REPUBLIC OF TÜRKİYE

YILDIZ TECHNICAL UNIVERSITY

GRADUATE SCHOOL OF SCIENCE AND ENGINEERING

SUSTAINABLE UTILIZATION OF CHROMIUM MINING WASTE IN SODIUM BOROSILICATE GLASS-CERAMIC COATING SYSTEMS

Kumru KARAMAN ÜNLÜTÜRK

MASTER OF SCIENCE THESIS

Department of Metallurgical and Materials Engineering

Material Program

Supervisor

Assoc. Prof. Dr. Buğra ÇİÇEK

August, 2024

REPUBLIC OF TÜRKİYE

YILDIZ TECHNICAL UNIVERSITY

GRADUATE SCHOOL OF SCIENCE AND ENGINEERING

SUSTAINABLE UTILIZATION OF CHROMIUM MINING WASTE IN SODIUM BOROSILICATE GLASS-CERAMIC COATING SYSTEMS

A thesis submitted by in partial Kumru KARAMAN ÜNLÜTÜRK fulfillment of the requirements for the degree of MASTER OF SCIENCE is approved by the committee on 07.08.2024 in Department of Metallurgical and Materials Engineering, Material Program.

Assoc. Prof. Dr. Buğra ÇİÇEK
Yıldız Technical University
Supervisor

Approved By the Examining Committee

Assoc. Prof. Dr. Buğra ÇİÇEK, Supervisor
Yildiz Technical University _____

Prof. Dr. Recep ARTIR, Member
Marmara University _____

Asst. Prof. Dr. Hakan YILMAZER, Member
Yildiz Technical University _____

I hereby declare that I have obtained the required legal permissions during data collection and exploitation procedures, that I have made the in-text citations and cited the references properly, that I haven't falsified and/or fabricated research data and results of the study and that I have abided by the principles of the scientific research and ethics during my Thesis Study under the title of Investigation, Sustainable Utilization of Chromium Mining Waste In Glass-Ceramic Coating Industry supervised by my supervisor, Assoc. Prof. Dr. Buğra ÇİÇEK. In the case of a discovery of false statement, I am to acknowledge any legal consequence.

Kumru KARAMAN ÜNLÜTÜRK

Signature

Dedicated to my family

and my best friends

ACKNOWLEDGEMENTS

I would like to express my sincere gratitude to the many individuals and institutions that contributed to the preparation of this thesis.

Firstly, I am deeply grateful to my thesis supervisor and esteemed professor, Assoc. Prof. Dr. Buğra Çiçek, for his guidance, valuable knowledge, and expertise throughout my research.

Additionally, I owe a debt of gratitude to Dr. Oğuz Karaahmet and MSc. Yasin Bozkurt Yılmaz, who have always been by my side throughout my educational journey. This study could not have been completed without their valuable contributions and patience.

I am also grateful to my family, who have supported me every step of the way, especially my spouse, Mete Ünlütürk, for his patience and belief in me. Moreover, I would like to thank my second family, my friends, who have motivated and encouraged me throughout this challenging process and my education journey. Special thanks to Emre Toy, MSc. Nurullah Çöpoğlu, Zeynep Hoşgör and Fahriye Altındal for their significant contributions to my study and for never hesitating to share their knowledge and efforts.

I would like to thank Akcoat Advanced Chemical Coating Materials and the technical staff there for assisting me with my experiments and patiently answering all my questions during my research.

With gratitude,

Kumru Karaman Ünlütürk

TABLE OF CONTENTS

LIST OF SYMBOLS x
LIST OF ABBREVIATIONS xii
LIST OF FIGURES xiv
LIST OF TABLES xvi
ABSTRACT xvii
ÖZET xix
1 INTRODUCTION 1
1.1 Literature Review 1
1.2 Objective of the Thesis....7
1.3 Hypothesis 7
2 GLASS CERAMIC 8
2.1 Definition and Classification of Pigments 8
2.2 Properties of Glass-Ceramics 10
2.3 Formation of Glass-Ceramic 12
2.3.1 Pressing 12
2.3.2 Casting 12
2.3.3 Spinning (Centrifugal Casting) 12
2.3.4 Float Process 12
2.3.5 Direct Forming or Reforming of Glass-Ceramics 13
2.4 Application of Glass-Ceramics....13
2.4.1 Technical Applications 15
2.4.2 Optical Applications 16
2.4.3 Electrical and Electronic Applications 16
2.4.4 Architectural Applications 17
2.4.5 Glass-Ceramics for Energy Applications....17
2.4.6 Coating and Solders....17
3 GLASS-CERAMIC COATINGS 18
3.1 Chemical Structure of Glass-Ceramic Coatings 18
3.1.1 Fluxes....21
3.1.2 Refractories 21
3.1.3 Opacifer....22
3.1.4 Color Agents 22

3.1.5 Adhesion Agents 22
3.2 Adhesion Mechanism Between Glass-Ceramic and Metallic Substrate 22
3.2.1 Diffusion Theory 22
3.2.2 Chemical Theory 23
3.2.3 Mechanical Theory 24
3.3 Properties of Glass-Ceramic Coatings 24
3.3.1 Thermal Properties 24
3.3.2 Physical and Mechanical Properties 29
3.3.3 Chemical Properties 32
4 ENAMEL COATED METAL SURFACES 34
4.1 Cast Iron 34
4.2 Decarburized Steel 35
4.3 Low Carbon Steel 35
4.4 Interstitial Free Steel 35
4.5 Stainless Steel 36
4.6 Coating Methods for Glass-Ceramic Coatings 36
4.6.1 Metallic Surface Preparation 36
4.7 Coating Methods 39
4.7.1 Spraying Technique 39
4.7.2 Dipping 39
4.7.3 Flow Coating 40
4.7.4 Electrostatic (Wet) Spraying 40
4.7.5 Electrostatic Powder Spraying 40
4.7.6 Electrophoretic Coating 40
4.7.7 Thermal Spray Coating 41
4.8 Coating Process 41
4.8.1 One Coat One Fire 41
4.8.2 Two Coat Two Fire 41
4.8.3 Two Coat One Fire 41
4.8.4 Three Coat Two Fire 42
4.8.5 Three Coat Three Firing 42
5 CHROMITE 44
5.1 Chromite Mines 45
5.2 Chromite Ore Processing 46
5.3 Chromium Effect on Environment and Human Health 47

6 EXPERIMENTAL STUDIES 49
6.1 Materials 50
6.2 COPR Characterization 50
6.2.1 Chemical Analysis 51
6.2.2 Phase Analysis 51
6.2.3 Thermal Analysis 51
6.2.4 Bonding-Structure Analysis 52
6.2.5 Surface Area Measurements 52
6.2.6 Microstructural Analysis 52
6.3 Precursor Glass Synthesis 52
6.4 Precursor Glasses Characterization 53
6.4.1 Chemical Analysis of Precursor Glasses 53
6.4.2 Crystalline Structure Analysis of Precursor Glasses 54
6.4.3 Thermal Behaviour Determination of Precursor Glasses 54
6.5 Milling and Coating Application 55
6.6 Glass-Ceramic Coating Characterization 55
6.6.1 Phase Determination of Glass Ceramic Coatings 55
6.6.2 Microstructural and Elemental Analysis 56
6.6.3 Impact Resistance Measurement 56
6.6.4 Acid Resistance Analysis 57
6.6.5 Coating Thickness 57
6.6.6 Color Measurement 57
6.6.7 Gloss Measurement 57
7 RESULTS AND DISCUSSION 59
7.1 COPR Characterization 59
7.2 Heat Treatment of COPR Samples 61
7.3 Heat Treated COPR Samples Characterization 62
7.4 PG Characterization 75
7.5 GCC Characterization 85
7.5.1 Phase Analysis 85
7.5.2 Microstructure Analysis 87
7.5.3 Color Measurement 96
7.5.4 Gloss Measurement 98
7.5.5 Acid Resistance Analysis 98
7.5.6 Coating Thickness 99

7.5.7 Impact Resistance Analysis 99
8 CONCLUSION **101**
REFERENCES **105**
PUBLICATIONS FROM THE THESIS **117**

LIST OF SYMBOLS

A	Ampere
°C	Celsius Degree
cm	Centimeter
cm^3	Centimeter Cube
cm^2	Centimeter Square
ΔE	Color Difference Measurement
q	Cooling Rate of Glass
q_c	Critical Cooling Rate
cc	Cubic Centimeter
dm^3	Cubic Decimeter
d	Density
E	Elasticity Modulus
eV	Electronvolt
l	Elongation
GPa	Gigapascal
T_g	Glass Transition Temperature
g	Gram
h	Hour
K	Kelvin
kg	Kilogram
kJ	Kilojoule
kV	Kilovolt
L	Length
L	Lightness – Darkness in Color Values
α	Linear Thermal Expansion Coefficient
T_L	Liquid Temperature
lt	Liter
m/m	Mass Percent Concentration
MPa	Megapascal
T_m	melting temperature
m	Meter
m^3	Meter Cube

m^2	Meter Square
μm	Micrometer
mK	milli Kelvin
mA	milliampere
mg	Milligram
mL	Milliliter
mm^2	Millimeter Square
mV	Millivolt
nm	Nanometer
N	Newton
T_N	Nose coordinates
Pa	Pascal
±	Plus – Minus
pH	Potential Hydrogen
a	Redness – Greenness in Color Values
sec	Second
S	Specific gravity of enamel
c	Specific Heat
σ	Tensile Strength
λ	Thermal Conductivity Coefficient
K	Thermal Shock
d	Thickness
V	Volt
β	Volume Thermal Expansion Coefficient
W	Watts
w	weight
p	weight of pycnometer
wt. %	Weight Percent
b	width

LIST OF ABBREVIATIONS

ADL	Activities of Daily Life
ANOVA	Analysis of Variance
BET	Brunauer-Emmett-Teller
C	Calcination
COE	Coefficient of Linear Thermal Expansion
COPR	Chromite Ore Processing Residue
Cr	Chromium
D	Dried
DSC	Differential Scanning Calorimetry
DTA	Differential Thermal Analysis
EDS	Energy-Dispersive X-Ray Spectroscopy
FT-IR	Fourier Transform Infrared Spectroscopy
GC	Glass Ceramic
GCC-STD-Co	Glass Ceramic Coating-Commercial Raw Material Derived-Cobalt Based Adhesion Agent
GCC-STD-Ni	Glass Ceramic Coating-Commercial Raw Material Derived-Nickel Based Adhesion Agent
GCC-WD-Co	Glass Ceramic Coating-Waste Derived- Cobalt Based Adhesion Agent
GCC-WD-Ni	Glass Ceramic Coating-Waste Derived-Nickel Based Adhesion Agent
GU	Gloss Units
HSM	Hot Stage Microscopy
HW21	Chromium-containing waste category on the China National Hazardous Waste List
LOI	Loss On Ignition
PG	Precursor Glass
PG-STD-Co	Precursor Glass-Commercial Raw Material Derived-Cobalt Based Adhesion Agent
PG-STD-Ni	Precursor Glass-Commercial Raw Material Derived-Nickel Based Adhesion Agent
PG-WD-Co	Precursor Glass- Waste Derived-Cobalt Based Adhesion Agent
PG-WD-Ni	Precursor Glass-Waste Derived-Nickel Based Adhesion Agent
PV	Pore Volume
RM	Red Mud
SCE	Specular Component Excluded

SCI	Specular Component Included
SEM	Scanning Electron Microscopy
SSA	Specific Surface Area
STD	Standard
TEM-EDX	Transmission Electron Microscopy Energy Dispersive X-ray
TG-DTA	Thermogravimetric – Differential Thermal Analysis
UV	Ultraviolet
WD	Waste Derived
XANES	X-ray absorption near edge structure
XRD	X-Ray Diffraction
XRF	X-Ray Fluorescence

LIST OF FIGURES

Figure 2.1 From glass to glass-ceramic. (a) nuclei formation, (b) crystal growth on nuclei, and (c) glass-ceramic microstructure 9

Figure 2.2 Time-temperature-transformation diagram for glass-ceramic formation 10

Figure 2.3 Mechanical properties chart of glass, glass- ceramics, and ceramics in the literature 11

Figure 3.1 Ellingham Diagram 23

Figure 3.2 Viscosity – Temperature curve for a theoretical glass 28

Figure 3.3 Rate – Viscosity and Temperature graph of the enamels during firing process 29

Figure 5.1 The spinel structure (A) as a ball and stick model and (B) as coordination polyhedra. In a) oxygen is red, the divalent atom (Mg is spinel, Fe in chromite) is yellow and the trivalent atom (Al in spinel, Cr in chromite) is shown as blue and at the center of the yellow tetrahedra. 44

Figure 5.2 Map of locations, geological types, and size (millions of tons of Cr) of global chromite resources and reserves. 46

Figure 5.3 Schematic diagram of Chromite ore processing 47

Figure 6.1 Experimental processes of the study 49

Figure 7.1 TG-DTA of COPR 61

Figure 7.2 XRD analysis of COPR samples 65

Figure 7.3 Ternary phase diagram of MgO-SiO_2-H_2O 66

Figure 7.4 COPR samples FTIR analysis result 69

Figure 7.5 COPR samples Raman analysis result 71

Figure 7.6 COPR samples hot stage microscopy analysis result 72

Figure 7.7 SEM analysis result of heat treated COPR samples 74

Figure 7.8 SEM-EDS analysis result of heat treated COPR samples. 75

Figure 7.9 XRD analysis results of precursor glasses 77

Figure 7.10 a) X-ray photoelectron spectroscopy (XPS) survey spectra b) high-resolution XPS spectra of Cr2p of D-200, C-1150 and GCC-WD sample 78

Figure 7.11 TG-DTA analysis results of precursor glasses 80

Figure 7.12 HSM analysis results of precursor glasses 82

Figure 7.13 Dilatometer analysis results of precursor glasses a) PGs containing nickel-derived adhesion agent, b) PGs containing cobalt derivative adhesion agent 84

Figure 7.14 XRD analysis results of glass ceramic coatings 87

Figure 7.15 SEM analysis of glass ceramic surfaces a) GCC-STD-Ni b) a) GCC-STD-Co c) WD-Ni d) WD-Co 88

Figure 7.16 SEM imaging of cross-section between glass-ceramic coating and steel substrate of GCC-STD-Ni 92

Figure 7.17 SEM imaging of cross-section between glass-ceramic coating and steel substrate of GCC-STD-Co 93

Figure 7.18 SEM imaging of cross-section between glass-ceramic coating and steel substrate of GCC-WD-Ni 94

Figure 7.19 SEM imaging of cross-section between glass-ceramic coating and steel substrate of GCC-WD-Co 95

Figure 7.20 Glass ceramic coatings low magnification optical microscope images 96

Figure 7.21 Impact test results of the glass ceramic coatings 100

LIST OF TABLES

Table 2.1 The main crystalline phases, properties and application areas of some glass-ceramic systems 13

Table 3.1 Raw materials of glass-ceramic coatings, minerals and the functions of the components 19

Table 3.2 The classification of oxides according to their functions in the glass structure 21

Table 3.3 Cubical thermal expansion coefficients of some enamels and some metals ... 25

Table 3.4 Bulk densities and coefficient of thermal expansions of some enamel types 27

Table 4.1 Limit composition of cast iron for enameling applications 34

Table 4.2 Chemical composition of a commercial IF steel 36

Table 4.3 Some cleaner components and their function in chemical surface cleaning before the enamelling application 38

Table 4.4 Coating process techniques for some industrial application areas 42

Table 5.1 Physical Properties of chromite 45

Table 6.1 Calcination condition explanation of samples 50

Table 6.2 Identificatioon of precrsor glasses 53

Table 7.1 Uncalcined waste chemical analysis results 59

Table 7.2 Sample identification derived from TG-DTA 62

Table 7.3 Heat treated samples chemical compositions 63

Table 7.4 COPR sample phases and their properties 67

Table 7.5 BET analysis result of samples 73

Table 7.6 Chemical compsitions of precursor glasses 76

Table 7.7 Cr2p peak positions and areas for D-200, C-1150 and PG-WD samples 82

Table 7.8 Characteristic thermal point results of precursor glasses from HSM analysis 89

Table 7.9 EDS point elemental distrubition of glass ceramic coatings 90

Table 7.10 Color measurement of glass ceramic coatings 97

Table 7.11 Gloss measurement of glass ceramic coatings 98

ABSTRACT

Sustainable Utilization of Chromium Mining Waste in Sodium Borosilicate Glass-Ceramic Coating Systems

Kumru Karaman ÜNLÜTÜRK

Department of Metallurgical and Materials Engineering

Master of Science Thesis

Supervisor: Assoc. Prof. Dr. Buğra ÇİÇEK

Increasing the reusability of waste in industrial processes offers both environmental and economic benefits. Chromite ore processing residues (COPR) released in our country are studied in order to examine the usability of mining wastes in the industry, the problems that may arise during their use, and whether they have the feature of being a substitute raw material. It investigates the potential use of COPR as an alternative raw material in sodium borosilicate glass-ceramic coatings and also aims to adapt to the structure potentially hazardous components such as Cr^{6+} that can be released into nature. Precursor glass production, one of the intermediate stages in glass ceramic coating production, was carried out at high temperatures. To examine the effect of this heating process on the COPR waste, TG-DTA analysis was performed and the waste was then calcined at critical temperature points. The study analyzes calcined samples considering the critical points of TG-DTA analysis of COPR; examines composition, phases, microstructures, chemical bonds and surface areas. According to the melting performance of precursor glasses melted and quenched at 1300°C for 1 hour was examined in terms of chemical composition changes, amorphous structures and thermal behavior compatibility between coating interfaces.

Adhesive substances (NiO and CoO) that facilitate adhesion to steel surfaces were investigated and their suitability for waste and coating properties was evaluated. In the study, where the glass structure was applied to steel surfaces by electrostatic coating and fired at 860°C, the crystal structures of glass-ceramic coatings were determined by microstructural evaluation. The successful use of COPR as a raw material is evidenced by the absence of phases in the structure of the waste in the precursor glass structure, which is a completely amorphous structure. Moreover, XPS analysis results show that Cr^{6+} in COPR is immobilized in the glass structure and turns into Cr^{3+}.

Keywords: Chromite, Cr^{6+} reduction, calcination, characterization, sustainable raw material.

ÖZET

Sodyum Borosilikat Cam-Seramik Kaplama Sistemlerinde Krom Madenciliği Atıklarının Sürdürülebilir Kullanımı

Kumru Karaman ÜNLÜTÜRK

Metalurji ve Malzeme Mühendisliği Anabilim Dalı

Yüksek Lisans Tezi

Danışman: Doç. Dr. Buğra ÇİÇEK

Atıkların endüstriyel süreçlerde yeniden kullanılabilirliğin artırılması hem çevresel hem de ekonomik faydalar sunmaktadır. Bu çalışma, endüstriyel atıklar arasında hacmen büyük bir sınıfı oluşturan madencilik atıklarının endüstride kullanılabilirliği, kullanımı esnasında açığa çıkabilecek problemler ve ikame hammadde özelliği taşıyıp taşımadığını incelemek için ülkemizde açığa çıkan kromit madeni işleme kalıntılarının (KMİK) ile bağdaştırılıp bu atık sınıfının cam seramik endüstrisinde kullanımına odaklanmaktadır. KMİK'in sodyum borosilikat cam-seramik kaplamalarda alternatif bir hammadde olarak potansiyel kullanımını araştırmakta ve ayrca doğaya salınabilecek Cr+6 gibi potansiyel olarak tehlikeli bileşenlerin yapıya uyarlanmasını amaçlamaktadır. Cam seramik kaplama üretiminde ara aşamalardan biri olan öncü cam üretimi yüksek sıcaklıklarda gerçekleştirilmiştir. Bu ısıtma işleminin KMİK atığı üzerindeki etkisini incelemek amacıyla TG-DTA analizi yapılmış ve ardından atık, kritik sıcaklık noktalarında kalsine edilmiştir. Çalışma, KMİK'in TG-DTA analizinin kritik noktalarını göz önünde bulundurarak kalsine numuneleri analiz etmekte; kompozisyon, fazlar, mikro yapılar, kimyasal bağlar ve yüzey alanlarını incelemektedir. 550°C'de tespit edilen reaksiyon noktası, XRF analizinde gözlenen yapıdan karbonun uzaklaştırılmasıyla açıklanabilirken, 819°C ve 1135°C'deki noktalar ise lizardit fazının oluşumu ve polimorfik dönüşümleri

ile açıklanabilir. XRD analizine göre, düşük sıcaklıklarda (200-400-500°C) kalsine edilen numunelerde ortak fazlar krizotil ve lizardit iken, kalsinasyon sıcaklığı arttıkça bu yapılar forsterit ve enstatit fazlarına dönüşmektedir. 1300°C'de 1 saat süreyle eritilen ve söndürülen öncü camların erime performansı, kimyasal bileşim değişiklikleri, amorf yapılar ve kaplama arayüzleri arasındaki termal davranış uyumluluğu açısından incelenmiştir. Çelik yüzeylere yapışmayı kolaylaştıran yapışma maddeleri (NiO ve CoO) araştırılarak atık ve kaplama özelliklerine uygunluğu değerlendirilmiştir. Cam yapının çelik yüzeylere elektrostatik kaplama ile uygulanıp 860°C'de pişirildiği çalışmada, cam-seramik kaplamaların mikroyapısal değerlendirilmesi yapılarak kristal yapıları belirlenmiştir. KMİK'in hammadde olarak başarılı kullanımı, tamamen amorf yapı olan birincil cam yapıdaki atığın yapısında fazların bulunmaması ile kanıtlanmaktadır. Cam-seramik kaplama yapısının ana fazlarının floro-tremolit, kuvars ve kristobalit olduğu da kanıtlanmıştır. Ayrıca, XPS analiz sonuçları, KMİK'deki Cr^{+6}'nın cam yapı içinde immobilize edildiğini ve Cr^{+3}'a dönüştüğünü göstermektedir.

Anahtar Kelimeler: Kromit, Cr^{6+} redüksiyon, kalsinasyon, karakterizasyon, sürdürülebilir hammadde.

1 INTRODUCTION

1.1 Literature Review

The increase in global population brings with it the problem of depletion of the world's natural resources. This reduction has prompted efforts to explore new resources, also has heightened the significance of sustainability and waste management concepts. Utilizing as a new source of waste becomes an appealing approach, capable of reducing or eliminating disposal costs and potential pollution issues, all the while enhancing resource conservation [1].

Waste generated from industrial activities, which can be reintroduced at any stage of the industrial process, is categorized as industrial waste. This particular type of waste holds potential resources for various sectors within the industry.

Smelting stands out as a sustainable alternative to recycling through calcination and deposition in landfills [2]. Among these sustainable approaches, the vitrification method plays a crucial role in stabilizing various inorganic wastes and metal elements. This is achieved by chemically bonding them to create a glassy structure through a thermal fusion process [3]. Vitrification processes encompass the melting of waste at high temperatures, followed by quenching using glass-forming agents and network modifiers, ultimately resulting in the formation of an amorphous structure [4].

Glass, glass-ceramic and ceramic structures with rich and complex input structures are suitable and easily adaptable options for industrial wastes in complex form.

In the literature, there are studies showing that steel production slag, plant ashes, cement waste, industrial livestock waste, fly and bottom ash, waste glass and ceramic products and mine waste can be used as a new alternative raw material [5], [6].

One of the most common industrial wastes is industrial waste generated during mining and ore processing [7], [8].

One of the frequently released industrial wastes is the process residue separated from the valuable chromium grade during the extraction of the chromite mineral, which is found in the world. Although the chemical structure of the waste varies depending on the mining region; it has a magnesium silicate structure containing magnesium (Mg) and silicon (Si)

oxides. Since the structure may contain chromium (VI) [Cr(VI)] which is harmful to be released into nature; It is important that it can be integrated into a structure sustainably. In recent years, environmental problems caused by chromium waste, especially Cr(VI) pollution, have attracted public attention worldwide. Chromite ore processing residue (COPR), a by-product of chromium extraction from chromite ores, is an important Cr-containing waste and has become the main source of Cr pollution in the environment. After decades of chromium extraction, the amount of COPR accumulated is significant, especially in some developing countries. For example, the total amount of COPR in China is estimated to be over 6 million tons and increasing by approximately 60,000 tons every year [1], [9], [10].

COPR is a toxic and hazardous waste slag generated during the production of chromium salt, which belongs to HW21 (chromium-containing waste category) on the China National Hazardous Waste List. COPR contains Cr (VI), which is a teratogen, carcinogen, and mutagen [8], [11]. Unreasonable storage or disposal will pollute soil, surface water, and groundwater, posing a significant danger to human life and health [8], [11]. It is therefore imperative that COPR is disposed of reasonably, efficiently and safely [12].

Although there are studies in the literature on the use of COPR in glass, glass-ceramic, glaze, pigment and cement products, the investigation of the successful adaptability of COPR to glass-ceramic coatings on metal surfaces, commercially called enamel, will be revealed for the first time within the scope of this thesis [10], [12]–[18]

Kilinçarslan et al.'s study aims to determine the advantages of using COPR foam concrete as a building material, reduce the production cost of foam concrete, produce alternative solutions for rehabilitation and eliminate environmental pollution. Chromite enrichment wastes obtained from Fethiye, Köyceğiz, Denizli and Burdur regions were used as aggregate in the production of foam concrete. In the study, compressive strength tests were carried out according to TS EN 1354 and thermal conductivity tests were carried out according to TS EN 12664. As a result, it has been reported that chromite waste (dunite) can be used in foam production. In this study, four different types of foam concrete samples were produced [17].

Fresh concrete was placed in an impermeable container and weighed, and its unit density was determined according to TS EN 12350-6 (2010) standard. The thermal conductivity coefficient is designed for thermal conductivity measurements of materials with a

coefficient of less than 10 W/mK. Thermal conductivity tests were carried out according to TS EN 12664 (2009) and TS EN 12667 (2003) standards.

When the compressive strength of foam concrete was evaluated, chromium waste as aggregate, which generally consists of dunite, did not cause any loss of strength in foam concrete. However, it has also been reported that dunite aggregate caused volume loss in foam concrete, which in turn caused the density of foam concrete to increase. As a result, it has been seen that chromite waste can be used in foam concrete production under certain conditions.

Liao et al. studied the detoxification and immobilization of chromite ore processing residue (COPR) in a spinel-based glass-ceramic matrix. In the search for a more chemically resistant matrix for COPR, it was found that the most critical crystalline phase for Cr immobilization was a spinel solid solution with the chemical composition $MgCr_{1.32}Fe_{0.19}Al_{0.49}O_4$ and the study was continued on this structure. The COPR-containing blend was melted at 1450°C for 3 hours and transferred to another crucible to obtain a glass-ceramic structure. Comparative analyzes were also carried out by casting standard glass ceramics that would exactly match the chemical composition of the structure. It was determined that the most critical crystalline phase for Cr immobilization was the spinel solid solution with the formula $MgCr_{1.32}Fe_{0.19}Al_{0.49}O_4$ determined by TEM-EDX. The final product is reported to consist of spinel, diopside, and amorphous contents, and their amounts are 3.5 wt.%, 5.2 wt.%, and 91.2 wt.%, respectively; here spinel and diopside are encapsulated by amorphous contents. It has also been proven that most of the chromium (about 77%) is contained in the spinel phase. With XANES, it was revealed that the transfer of all Cr(VI) to Cr(III) was almost complete. The study demonstrates that the spinel-based glass-ceramic product constitutes a safer means to immobilize Cr than simply encapsulating Cr in a glass matrix or crystalline phase. It has even been reported that it may be possible to use glass-ceramic products beneficially as construction materials [19].

Furthermore, in an other study; Li et al. focused on solving the problem of Chromium slag turning yellow and the accumulation of large amounts of Red Mud, and investigated the use of Red Mud and chromite ore process residue instead of clay in glass-ceramic production. Red Mud (RM), COPR and silicon dioxide were homogenized in ethanol and heat treated at 1200 °C for 2 hours. After sintering at 1200°C for 2 h, the concentration of Cr(VI) and total Cr in glass ceramics was determined that the detection limit of Cr(VI)

was 0.2 mgL^{-1} and total Cr was 0.004 mgL^{-1}. The examination of the physical and chemical processes in these glass-ceramic-forming solid wastes revealed that lowering the melting point of silicon dioxide can induce the transformation of some quartz into cristobalite and squamous quartz. As a result of the study, it has been proven that through industrial-scale production, the use of these composite materials can significantly improve environmental pollution in these landfills and reduce the irreversible damage caused to nature by traditional building materials mining [13].

Öztürk and Dal worked together on whether a new ceramic pigment material could be obtained from the wastes resulting from the processing of chrome ore for industrial glaze application. In order to investigate the color effect of pigments synthesized with different types of frits in industrial glazes, they calcined the waste powder at 900°C and 1000°C and added 5-20% calcined COPR waste to transparent, opaque and matte glaze compositions and fired at 1000°C and 1100°C. The parameters of the study were determined with the factorial experimental design method; 144 tiles were produced and their color values (L*, a*, b*) were measured. Brown and green tones have been reported to appear after firing, influenced by changes in the glaze composition. Researchers used ANOVA analysis to compare changes in results. They identified the main factors affecting L* values and stated that the most important ones are the amount of waste 38.5%, the type of frit 27.9% and the firing temperature 23.4%. For a* values, cooking temperature, frit type and waste amount were determined as the most effective factors. It has been reported that the total effect on a* values is 60.4% of the cooking temperature, 23.2% of the frit type and 5.4% of the waste amount. It was determined that the important factors affecting b* values are frit type, waste amount and firing temperature. The increasing amount of waste led to higher b* values. X-ray diffraction (XRD) analysis revealed the presence of Iron(II,III) oxide (Fe_3O_4) and Iron(III) oxide (Fe_2O_3) phases in both transparent and opaque glazed tiles. Due to the high Magnesium oxide (MgO), Calcium oxide (CaO) and Fe_2O_3 content of chromite processing wastes, the augite phase of glazed tiles increased and different colors (from brown tones to green tones) and surface textures were observed depending on the amount of waste and frit type. It has been reported from this study that it can be concluded that this waste powder can be used to economically produce pigments for different industrial ceramic glazes [15].

Glass-ceramic coatings coated on the substrate material (glass, aluminum, steel or cast iron) are produced by vitrification and controlled crystallization of inorganic oxide components. This type of coating is industrially called enamel [20].

There are several main steps to create this type of glass ceramic coating. Firstly; components such as silicon dioxide (SiO_2), magnesium oxide (MgO), aluminum oxide (Al_2O_3), calcium oxide (CaO) and fluorine (F) are mixed by taking into account the final product properties, these components are melted at 1200°C ±100 °C and then rapidly cooled (the vitrification procedure consisting of quenching to obtain this glassy structure). To proceed to the coating step, the glass precursor is ground and sieved to obtain powder, the application is carried out and the coating is obtained with the sinter-crystallization step [21].

Glass-ceramic coatings help prevent mechanical and thermal deterioration due to exposure of materials such as kitchen utensils, household appliances, and boilers [22].

The aim of the study is to characterize the physical, chemical, thermal, and morphological properties of chromite mine process waste, which is one of the mine wastes, and to investigate its use as raw material in inorganic coating production and to use it in a coating structure by integrating it with industrial raw materials. First, X-ray fluorescence (XRF) analysis was performed to determine the chemical composition of the wastes obtained from the Adana region. X-Ray Diffraction (XRD) analysis was used to examine phase and crystallinity. Following these analyses, Fourier-transform infrared spectroscopy (FT-IR), Raman Spectroscopy (RAMAN), Brunauer-Emmett-Teller (BET), Scanning electron microscopy - energy dispersive X-Ray Spectroscopy (SEM-EDS) analyzes were performed to determine the properties of the wastes such as bond structure, surface area and morphology. After all these features were determined, Thermogravimetry Differential Thermal Analysis (TG-DTA) analysis was performed to observe the thermal behavior of the waste. After thermal characterization, in-depth research continued, analysis critical temperatures were determined, and calcination was carried out at these temperatures. To observe the change of calcined samples compared to unprocessed waste, XRF, XRD, FTIR, RAMAN, BET and SEM-EDS analyzes were repeated and comparisons were made.

It aims to provide a new strategy for achieving sustainable glass-ceramic coating by integrating COPR wastes with commercial raw materials as a source of SiO_2 and MgO.

To examine whether COPR wastes could be successfully incorporated into glass-ceramic coatings and to examine the change of adhesion agents that strengthen the bond with the metal with this integration, 4 different precursor glasses were created and analyzed. Frits consisting entirely of commercially available raw materials and formulations containing partial amounts of COPR were designated commercial raw material derived (STD) and waste derived (WD), respectively. In addition, precursor glass-commercial raw material derived-nickel based adhesion agent (PG-STD-Ni), precursor glass-waste derived-nickel based adhesion agent (PG-WD-Ni) and precursor glass-commercial raw material derived-cobalt based adhesion agent (PG-STD-Co), precursor glass-waste derived-cobalt based adhesion agent (PG-WD-Co) precursor glasses were created to examine glass structures containing nickel and cobalt adhesion agents.

The chemical composition, phase transition and thermal behavior of the frits were analyzed using XRF, XRD, heating microscopy and TG-DTA. Typical noble borosilicate glass-ceramic coatings were formed after coating the frits on metal substrates by electrostatic spraying method and crystallizing them at 860 °C for 6 minutes. These coatings are named glass ceramic coating- commercial raw material derived- nickel based adhesion agent (GCC-STD-Ni), glass ceramic coating-waste derived-nickel based adhesion agent (GCC-WD-Ni) and glass ceramic coating- commercial raw material derived- cobalt based adhesion agent (GCC-STD-Co), glass ceramic coating-waste derived-cobalt based adhesion agent (GCC-WD-Co). XRD and SEM-EDS analyzers were used to characterize it in terms of micro and macrostructure, phase formation, and surface morphology. Additionally, the engineering properties of the coatings, such as adhesion behavior, chemical resistance and aesthetic properties, were examined according to standards.

1.2 Objective of the Thesis

The aim of the study is to characterize the physical, chemical, thermal, and morphological properties of chromite mine process waste, which is one of the mine wastes, and to investigate its use as raw material in glass ceramic coating production and to use it in a coating structure by integrating it with industrial raw materials.

1.3 Hypothesis

The hypothesis of this study is that chromite ore processing residue (COPR), which contains a large amount of magnesium oxide, silicon oxide and iron oxide in its structure and trace amounts of nickel oxide and chromium oxide, can be effectively used as an alternative raw material as a source of magnesium oxide and silicon oxide in the production of glass-ceramic coating. Specifically, the research suggests that:

- Environmental Mitigation: The potentially hazardous Cr^{+6} present in COPR will be immobilized within the glass-ceramic matrix and reduced to the less harmful Cr^{+3} form, thereby reducing its environmental impact.
- Economic and Industrial Viability: Utilizing COPR in glass-ceramic production will provide an economically viable waste management solution, while also producing high-performance coatings suitable for various industrial applications.

2
GLASS CERAMIC

2.1 Definition and Classification of Pigments

Famous glass scientist Dr. S.D. Stookey discovered and defined glass-ceramics in the 1950s. Glass-ceramics were defined by Dr. Stookey as "*Glass-Ceramics are made by first melting and forming special glasses containing nucleating agents and then causing controlled crystallization of the glass*" [23].

Dr Stookey, often regarded as the innovator in the realm of glass-ceramics, was a trailblazer in inducing and comprehending internal nucleation processes within glass. His initial research on dense opal glasses and the photosensitive precipitation of gold and silver within glass resulted in a remarkable sequence of innovations. These innovations encompassed Fotalite®, a photosensitive opal, chemically machined Fotoform®, and Fotoceram®, as well as Titanium dioxide TiO_2-nucleated Pyroceram™ products, which included missile nosecones and heat-resistant cookware. Stookey secured a fundamental patent for glass-ceramics, and despite facing legal challenges, the patent was ultimately contested and upheld in court [1].

With another definition Glass-ceramics are ceramic materials created by subjecting base glass to controlled nucleation and crystallization processes, resulting in the formation of a polycrystalline structure with a finely dispersed and uniform arrangement of crystals throughout the parent bulk glass structure [24], [25]

The process of crystallization is initiated by introducing nucleating agents into the glass matrix. These nucleating agents, primarily titanium dioxide (TiO_2), chromium (III) oxide (Cr_2O_3), zirconium dioxide (ZrO_2), and phosphorus pentoxide (P_2O_5) oxide groups, along with fluorides, serve as centers for nucleation within the matrix. During the controlled heat treatment, these nuclei undergo growth, forming crystals. Typically, complete crystallization does not occur, and the crystal structure retains an amorphous character. Crystallization yields one or more crystalline phases, and the resulting crystals exhibit diverse shapes, commonly appearing as rods, sheets, or spheres. Typically, these crystals are smaller than 1 μm, imparting exceptional properties such as enhanced toughness, impact resistance, and wear resistance to the glass-ceramic [2], [9], [26]. Formation of glass-ceramics is shown in Figure 2.1.

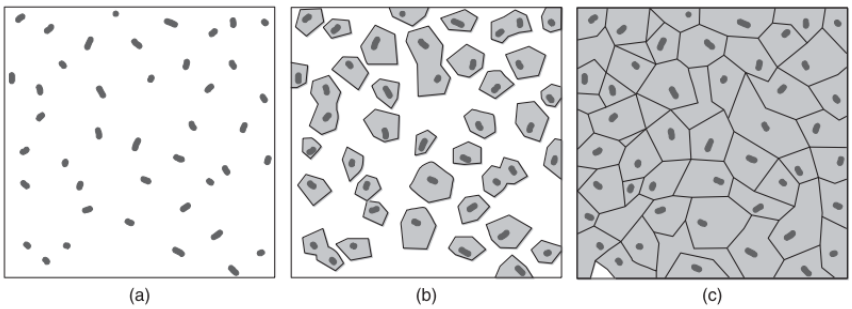


Figure 2.1 From glass to glass-ceramic. (a) nuclei formation, (b) crystal growth on nuclei, and (c) glass-ceramic microstructure [9]

An updated definition of glass-ceramics should embody the fundamental processing concept introduced by pioneers like Stookey. These pioneers envisioned the inherent advantages of the glass-ceramic route in comparison to traditional ceramic processing. The traditional glass-ceramic route involves three main steps: i) melting, homogenizing, and refining a batch to create an optically homogeneous glass with nucleating agents; ii) shaping a glass ware through hot-forming methods; and iii) inducing internal crystallization through controlled thermal treatments to produce a pore-free, nearly final shape product with the desired functionality.

In the first two steps (i and ii), the creation of a glass ware is crucial, and various routes, such as melt-quenching, sol-gel, or vapor deposition, may be employed, resulting in powders, thin films, or bulk glass products. Techniques like Differential Thermal Analysis (DTA) and Differential Scanning Calorimetry (DSC) signals or X-ray analysis can verify glass formation, and rapid cooling rates are essential for the melt-quenching route. Uhlmann's classic treatment correlates the onset of crystallization with a crystal fraction of one part per million ($X = 10^{-6}$), below the detection limit of X-ray diffraction.

In the third step (iii), converting a glass ware into a glass-ceramic involves a controlled temperature-time process. The time required for achieving the desired crystal fraction depends on the number of nucleation sites and the growth rate of crystals. Complex time-temperature protocols are often used, and the selection of the temperature profile significantly influences the time evolution of the crystal fraction. Various factors, including finite size effects, non-uniform nucleation, and chemical composition differences between crystals and the parent glass, can complicate the crystallization scenario [3], [4], [27].

It's crucial to note that in this processing step, the heat treatment temperatures and times must be carefully chosen to induce the desired crystallization while preventing deformation of the already shaped glass ware. The microstructure that evolves through the three-step processing of glass-ceramics is illustrated in Figure 2.2.

In the graphic;

q: indicates the cooling rate of the glass,

qc: gives the critical cooling rate, qc = (T_L- T_N) / δt

Tg: Glass transition temperature,

T_L: Liquidus temperature,

T_N and δt: The nose coordinates that can change according to nucleation mechanism.

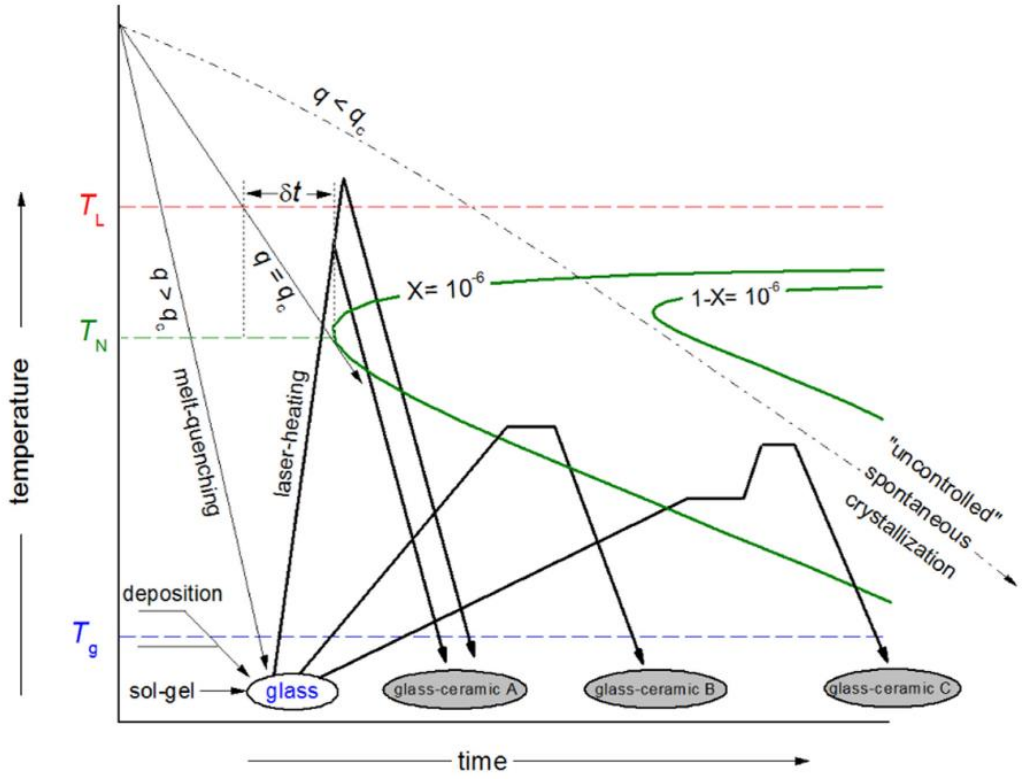


Figure 2.2 Time-temperature-transformation diagram for glass-ceramic formation

2.2 Properties of Glass-Ceramics

Typically, glass-ceramics exhibit a crystallinity, resulting in materials with diverse properties such as zero porosity, high strength, toughness, translucency or opacity, low or even negative thermal expansion, high-temperature stability, fluorescence,

machinability, ferromagnetism, restorability, high chemical durability, biocompatibility, bioactivity, ion conductivity, superconductivity, isolation capabilities, low dielectric constant and loss, and corrosion resistance [28].

Glass-ceramic materials, due to their thermal properties, undergo negligible shrinkage during production, making them highly suitable for widespread use in industrial and technological applications, particularly in kitchenware. Their glassy phase and nonporous structure enable the attainment of desired transparency and opacity values through meticulous control of crystals and microstructure. Additionally, glass-ceramic applications offer a versatile color spectrum, allowing the achievement of any desired color.

Chemically, when chemicals interact with glass-ceramics, their superior chemical properties are attributed to the crystal structure and glass composition. This imparts heightened chemical resistance to glass-ceramics, expanding their applicability.

In terms of mechanical properties, glass-ceramics exhibit remarkable strength characteristics. With developments in the field, flexural strengths can reach up to 500 MPa, and toughness values exceeding 3 MPa.m$^{1/2}$ have been achieved as shown in Figure 2.3. This mechanical resilience makes glass-ceramics suitable for applications requiring durability and resistance to mechanical stresses and impacts [9], [29]–[31].

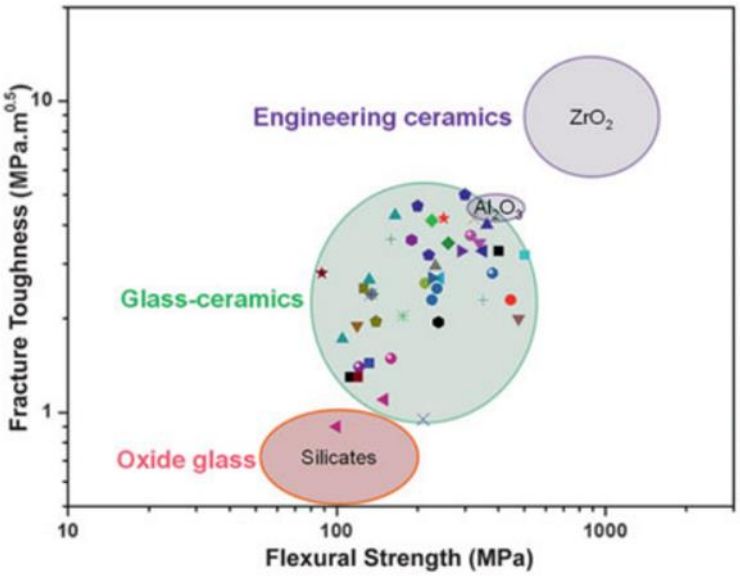


Figure 2.3 Mechanical properties chart of glass, glass- ceramics, and ceramics in the literature

2.3 Formation of Glass-Ceramic

Most commercially available glass-ceramics are initially shaped as glass and then undergo a heat treatment for internal nucleation and crystallization. These materials are engineered to be not only formed in the glassy state using efficient and swift glass-forming methods but also to undergo crystallization with minimal deformation, thereby maintaining the shape of the original glass article. The current glass-forming techniques employed with the parent glasses of glass-ceramics include pressing, casting, centrifugal casting or spinning, rolling, and the float process. Examples of glass-ceramics produced using these methods are detailed in the subsequent section [9].

2.3.1 Pressing

This method entails shaping glassware through pressure applied between a mold and a plunger. Typically, a horizontally rotating table features 8–16 mold positions on its periphery. Glass-ceramics produced through this technique include items like cookware (using a CorningWareTM block mold) and PyroceramTM tableware cups (using a split mold).

2.3.2 Casting

For this traditional technique, it is essential to have low glass viscosity and operate at temperatures exceeding the glass transition temperature. This method holds potential applications in the field of dentistry.

2.3.3 Spinning (Centrifugal Casting)

The distinctive feature of this method, setting it apart from standard casting, is the requirement for a rotating conical mold. In this process, the viscosity must fall within the range of 30 to 100 Pa s.

2.3.4 Float Process

The primary method of shaping in a molten tin bath is known as the float or Pilkington process, widely employed in contemporary flat glass production. In this process, molten glass is flattened and strengthened in the tin bath at lower temperatures as it comes from the furnace. The flat glass then proceeds along the same conveyor line, enters the annealing line to reduce tension, and continues its production process.

2.3.5 Direct Forming or Reforming of Glass-Ceramics

In certain instances, it is possible to reform a glass-ceramic in its crystalline state. The remaining glass may undergo softening, enabling deformation, or there might be adequate precipitation-creep to facilitate deformation even with a small amount of residual glass [9].

2.4 Application of Glass-Ceramics

Glass-ceramics, with their unique blend of glassy and crystalline properties, have become essential in various industries due to their superior strength, thermal stability, and durability. Engineered through controlled crystallization, these materials find applications in cookware, biomedical implants, aerospace components, and electronic substrates. Their versatility and customizable properties make glass-ceramics invaluable in advanced technologies [9], [32].

Table 2.1 The main crystalline phases, properties and application areas of some glass-ceramic systems [26]

Oxide System and Crystallization Agents	**Main Crystalline Phase**	**Property**	**Application Area**
$Li_2O.Al_2O_3.SiO_2$ (ZrO_2, TiO_2)	β-quartz β-spodumene β- eucryptite	Low thermal expansion High temperature resistance Transparency	Kitchenware Telescope Mirrors Oven Tops
$Li_2O.Al_2O_3.SiO_2$ (P_2O_5)	$Li_2O.Al_2O_3.SiO_2$	Dielectric properties Chemical resistance	Electronic Insulation Optical Coding Magnetic Recording Head Electric Sleeve

Table 2.1 The main crystalline phases, properties and application areas of some glass-ceramic systems (continued)

MgO. Al_2O_3.SiO_2 (P_2O_5, TiO_2)	Cordierite ($Mg_2Al_4Si_5O_{18}$)	Radar permeable Low expansion High strength	Missile Cap Radar Dome
PbO.ZnO. B_2O_3.SiO_2 (F)	Rankinite ($3CaO.SiO_2$)	Heat and vacuum insulation	Electrotechnology Microelectronic Circuits Capacitor
BaO.Al_2O_3.SiO_2 (TiO_2)	Celsian ($BaAl_2Si_2O_8$) Barium Titanate ($BaTiO_3$)	High strength Thermal shock resistance	Kitchenware Cookware
SiO_2.Al_2O_3.MgO. K_2O (F)	Phlogopite [$KMg_3AlSi_3O_{10}(F, OH)_2$]	Turning ability Dielectric properties	Electrotechnology Insulator Hermetic Seals
SiO_2.CaO.NaO_2 (P_2O_5)	Apatite [$Ca_5(PO_4)_3(F,Cl,OH)$]	Biocompatibiliy Resistance Chemical resistance	Dentistry Prostheses
SiO_2.Al_2O_3.MgO (TiO_2)	Mg-Al titanate [$MgxAl_{2(1-x)}Ti_{(1+x)}O$]	Hardness Resistance Abrasion resistant	Construction Material
SiO_2.Al_2O_3.CaO (ZnO)	Wollastonite ($CaSiO_3$)	Hardness Resistance Chemical resistant	Exterior Architectural Materials

2.4.1 Technical Applications

Radomes, as the inaugural glass-ceramic applications on the commercial scene, serve as vital protective enclosures for radar antennas. These structural, weather-resistant barriers play a pivotal role in minimizing the impact of electromagnetic signals transmitted or received by the antenna. The unique properties required for this application include a low dielectric loss and constant, a low coefficient of thermal expansion, high strength, and exceptional abrasion resistance. The careful selection and integration of glass-ceramic materials in radomes are driven by the need to strike a precise balance among these characteristics, ensuring optimal functionality and durability under diverse environmental conditions [33].

The utilization of photosensitive and etched patterned materials spans various fields such as electronics, chemistry, acoustics, optics, mechanics, and biology. These materials are intricately crafted in extremely sensitive miniature sizes to cater to the specific needs of these diverse disciplines. One commonly employed system for creating such glass ceramics is the SiO_2–Li_2O system. In this system, the parent glass is composed of Cerium Ce^{3+} and Silver Ag^{+} ions. Exposure to Ultraviolet UV light induces photoelectrons, triggering the oxidation of Ce^{3+} to Ce^{4+} and Ag^{+} to Ag^{0} within the compositions. Through controlled crystallization during heat treatment at 600 °C, crystal phases are precipitated, giving rise to the desired glass-ceramic structure. This tailored approach allows for the precise engineering of materials with unique properties, enabling their applications in a wide range of scientific and technological domains [34].

Glass ceramics (GCs) play a significant role in the realm of magnetic memory discs. Several common types of glass ceramics employed for this purpose include canasite, lithium disilicate, spinel–enstatite, and spinel. In this context, nanostructured fracture toughness and Young's modulus are critical material properties. For instance, in the case of materials like the solid solution of Gahnite type Zinc Aluminate ($ZnAl_2O_4$) or spinel type Magnesium Aluminate ($MgAl_2O_4$), or a solid solution of both types of crystals, the grain size must be smaller than 0.1 μm. Enstatite fracture toughness should exceed 1 $MPa \cdot m^{1/2}$, and the spinel–enstatite material should possess a high Young's modulus ranging from 100 to 165 GPa. These specific properties make spinel–enstatite a well-suited option for applications in magnetic memories, emphasizing the importance of tailored material characteristics in various technological applications [35].

2.4.2 Optical Applications

Various optical components, including Fiber Bragg Grating Athermalization, Laser-Induced Crystallization for Optical Gratings and Waveguides, Ferrule for Optical Connectors, Transparent Zinc Oxide (ZnO) Glass-Ceramics with Controlled Infrared Absorbance, and Microwave Susceptibility, have been successfully crafted using different crystal-based Glass Ceramics (GCs). These applications highlight the adaptability and precision of glass ceramics in the realm of optical technologies, showcasing their use in diverse optical components and functionalities [36].

Telescope mirror materials demand a near-zero coefficient of thermal expansion to cope with diverse temperature fluctuations. In this context, β-quartz solid-solution glass ceramics come into play. These materials are engineered to provide the necessary stability under changing temperatures, making them suitable for use in telescope mirrors. Additionally, integrated lens arrays have been crafted from lithium metasilicate/lithium disilicate glass ceramics, exhibiting a thickness of approximately 20 micrometers. This reflects the versatility of glass ceramics in meeting specific requirements for optical applications, where thermal stability and precision are crucial factors [37].

2.4.3 Electrical and Electronic Applications

Insulator materials, particularly those with a mica-type glass-ceramic composition, are designed to exhibit high dielectric constants. The creation of composite materials with elevated dielectric constants involves combining SiO_2-TiO_2-Nd_2O_5 and SiO_2-Al_2O_3-PbO glass-ceramic systems with sintered ceramics. In the manufacturing process, these inorganic components are mixed with a binder resin (such as butyl methacrylate), a solvent (toluene), and a plasticizer (dibutyl phthalate). The Doctor Blade Technique is then applied to a smooth flat surface, resulting in a material with a thickness ranging from 0.1 to 0.3 mm. The subsequent steps involve increasing the temperature to 400°C to burn out the organic components, followed by sintering at 900°C to achieve a mechanically strong and dense material. This process allows for the creation of circuit patterns on the surface after the removal of organics, contributing to the development of insulator materials with tailored dielectric properties for various applications [38].

2.4.4 Architectural Applications

Nippon Electric Glass develops the most important glass-ceramic for building applications under the NeopariésTM trademark [39].

The production of glass-ceramics involves the following steps: The foundation glass is created using granular glass particles. In a fully automated process, these granular glass particles are shaped into flat or curved panels within a tunnel furnace, reaching temperatures up to 1100°C. During the heat treatment, the granular glass undergoes sintering at 850°C. Temperatures exceeding 950°C lead to the crystallization of wollastonite. Glass-ceramics with properties such as weathering resistance, zero water absorption, lighter weight compared to natural stone building materials, increased hardness compared to natural stone, and more are produced through this process. These materials find applications in various areas, including the manufacturing of fire-resistant windows.

2.4.5 Glass-Ceramics for Energy Applications

Glass-ceramics play a pivotal role in enhancing the effectiveness of energy production and management across various applications. They are incorporated in at least three specific domains related to energy generation: (i) improving the efficiency of solar energy systems, (ii) contributing to battery components, and (iii) serving a vital role in solid oxide fuel cells [40].

2.4.6 Coating and Solders

Many commercial glass-ceramic coatings consist of ceramic glaze and enamel coatings. Both types of glass-ceramics are produced by crushing glassy components known as Frit, applying them onto a ceramic or metal substrate, and then sintering them. Due to the different expansion coefficients and surface properties of ceramics and metals, the oxides used as raw materials in glaze and enamel also vary. Consequently, the melting and sintering temperatures for these two glassy structures are also distinct. Ceramic glaze frits undergo vitrification at 1500°C and sintering at 1200°C, while enamel frits vitrify at 1300°C and sinter at 800°C.

3
GLASS-CERAMIC COATINGS

Glass-ceramic coatings, commonly known as enamel coatings, offer advanced technology for safe metal substrates and enhancing the durability of metal products [41]. The thin glassy layer serves as a protective barrier for the metallic substrate, shielding it from chemical corrosion in the surrounding corrosive environment. Enameling steels find widespread use in applications requiring chemical, corrosion, and weather resistance, as well as cleanability, mechanical and electrical properties, especially in cases where color or appearance holds significance [42]. Enamel is created by grinding frits, the essential components of enamels, into a fine powder and then applying it onto metallic substrates like steel, cast iron, copper, or aluminum. The subsequent step involves heating at temperatures ranging from 500 to 870°C. Various application methods are available, including electrostatic spraying, wet spraying, electrophoretic deposition, and more recently developed thermal spray methods. Enamel coatings exhibit outstanding engineering properties, including high-temperature endurance, chemical durability, and mechanical strength, along with aesthetic qualities. Consequently, enamel is a preferred choice for a wide range of products, including heating appliances, fireplaces, stoves, timepiece dials, culinary utensils, and hot water dispensers [43].

3.1 Chemical Structure of Glass-Ceramic Coatings

The essential components for enamel coatings are structures known as "frit." To create the frit structure, raw materials such as SiO_2 (silicon dioxide), Al_2O_3 (aluminum oxide), TiO_2 (titanium dioxide), ZrO_2 (zircon dioxide), P_2O_5 (phosphorus pentoxide), and F (fluorine) are melted at temperatures between 1200 and 1400°C. The inclusion of various oxides like sodium, potassium, and barium is contingent upon the specific location and desired features. Particle sizes of the raw materials play a crucial role before melting in terms of the melting regime and homogeneity. Rapid cooling is achieved by passing the melt, emerging from the furnace, through cooled steel rollers. The resultant amorphous structure, suitable for controlled crystallization, is termed "frit" [43].

Table 3.1 categorizes oxides based on their functionalities in the glass-ceramic structure. Within glass-ceramic systems, silica (SiO_2) demonstrates the ability to form glass at sufficiently high temperatures (above 1700°C) without the need for additional

components. In glass-ceramic formulations, SiO_2 is the most widely utilized component compared to others. Vitreous coatings, including glass-ceramic coatings, feature a silica tetrahedra network with other materials acting as modifiers. Low melting point components typically include one or two parts of SiO_2 per part of other components and melt at temperatures of 1050°C or lower. Conversely, compositions with higher melting points (1250°C or above) contain three to five parts of SiO_2. One notable drawback of SiO_2 as a coating ingredient is its exceptionally high melting point, exceeding 1700°C [44].

Table 3.1 Raw materials of glass-ceramic coatings, minerals and the functions of the components [45]–[48]

Component	Minerals	Functions
SiO_2	Quartz Feldspar	Refractory component, glass forming oxide, hardens the vitreous system, adds chemical resistance and increases viscosity.
B_2O_3	Borates	Flux that produces the vitreous matrix, reduces viscosity and increases surface hardness.
Na_2O K_2O Li_2O	Albite Feldspar Microcline Spodumene Petalite Lepidolite	Alkaline components that lower the temperature at which glass softens, reduce its elasticity and increase its brilliance.
Al_2O_3	Feldspar Corundum	Increases viscosity and chemical, mechanical and thermal resistance, reduces the expansion coefficient and favours an opaque finish.
ZrO_2	Zirconia	Improves resistance to acids, toughness, acts as an opacifier.

Table 3.1 Raw materials of glass-ceramic coatings, minerals and the functions of the components(continued)

ZnO	Zincite Blende Wurtzite	Excellent flux, lowers the expansion coefficient and improves brilliance and surface quality.
CoO	Cobaltite	A very strong adherence agent, it produces a structure with lots of small, well distributed bubbles.
NiO	Niccolite	A second adherence agent, it produces a structure with a small number of large bubbles.
CuO	Copper Oxide	When combined with primary bonds, it triggers the adherence reaction at lower temperatures.
MnO_2	Manganese Dioxide	Produces brown-colored frits, intensifies dark colors and acts as an oxidant and as a weak bonding agent.
Sb_2O_3	Antimonite	Produces a high degree of opacity and improves resistance to acids.
TiO_2	Rutile Anatase	Opacifiers, it increases whiteness, brilliance and resistance to acids and heat.
BaO CaO MgO	Baryte Witherite Calcite Dolomite Limestone Periclase	Alkaline-earthy components that integrate anti- acid glass-ceramics coating, increasing their resistance, their smelting facility and their viscosity.
P_2O_5	Apatite	Alters the opacity of the finish, improves color stability and reduces chemical resistance.
CaF_2	Fluorspar	Softens glass and influences the opacity

The function of the components in the chemical structure of glass-ceramic coatings divide the oxides utilized into five categories: fluxes, refractories, adhesion agents, opacifiers, and colorants which were given in Table 3.2.

Table 3.2 The classification of oxides according to their functions in the glass structure

Glass Former	**Glass Modifier** (R_2O)	**Glass Modifier** (RO)	**Glass Former** (RO_2, R_2O_3)	**Adhesion Promoter**
SiO_2	Li_2O	MgO	TiO_2	CaF_2
B_2O_3	Na_2O	CaO	ZrO_2	MnO_2
	K_2O	SrO	SnO_2	CoO
		BaO	Fe_2O_3	NiO
		ZnO	Al_2O_3	

3.1.1 Fluxes

Fluxes play a crucial role in enamel compositions by primarily aiming to reduce the melting temperature of silicon dioxide, the fundamental glass-making oxide. These oxides in the flux group also contribute to enhancing the consistency of the enamel. An enamel composition with optimal consistency not only strengthens the bond between enamel and metal but also positively influences surface quality. Additionally, these fundamental oxides in the flux group react with acidic refractories to form the glass structure. Key raw materials in this group include borax ($Na_2H_{20}B_4O_{17}$), soda ash (Na_2CO_3), soda nitrate ($NaNO_3$), fluorspar (CaF_2), cryolite (Na_3AlF_6), barium carbonate ($BaCO_3$), magnesium carbonate ($MgCO_3$), litharge (lead (II) oxide), red lead (lead (II, IV) oxide), and zinc oxide (ZnO) [45].

3.1.2 Refractories

Materials in this group play a vital role in forming the glass structure and supporting the acidic portion of the melt. Key materials in this category include quartz, feldspar, and

clay. Quartz serves as a glass former and is responsible for imparting essential mechanical and chemical properties to the final product [45].

3.1.3 Opacifer

The primary function of oxides in this group is to provide opacity to enamel coatings, as indicated in the title. Oxides in this category typically include antimony oxide (Sb_2O_3), sodium antimonate ($NaSbO_3$), titanium dioxide, zirconium silicate ($ZrSiO_4$), and zirconium dioxide (ZrO_2). A common characteristic of these oxides is their refractory properties. Additionally, auxiliary opacifiers like cryolite and fluorspar are utilized, contributing to increased fluidity of the melt [45].

3.1.4 Color Agents

Enamels are the coating type that is at the forefront with its aesthetic features as well as its superior technical features. For this reason, different colors and shades should be applicable in coatings. The most used oxides in this context are cobalt oxide (CoO), copper oxide (CuO), iron oxide and nickel oxide (NiO). These oxides can be used as colorants by themselves, and coloring can be done by adding pigment to the frits that are formed [45].

3.1.5 Adhesion Agents

Enamel coatings play a crucial role in establishing a strong bond with the metal surface to which they are applied. Oxides such as cobalt oxide, nickel oxide, and copper oxide are utilized in the melt for this purpose. Among them, CoO (cobalt oxide) is particularly significant as an adhesion agent, providing not only strong adhesion but also serving as a colorant, especially in the creation of a blue hue [45].

3.2 Adhesion Mechanism Between Glass-Ceramic and Metallic Substrate

3.2.1 Diffusion Theory

At the interfaces between the glass-ceramic coating and the metallic substrate, there is a phenomenon of iron diffusion from the metallic substrate to the glass-ceramic material, and simultaneously, silicon diffusion from the glass-ceramic to the substrate material

occurs. This diffusion process is believed to play a crucial role in contributing to the adhesion mechanism [49].

3.2.2 Chemical Theory

In this theory, during sintering, when the glass dissolves the existing oxide layer and comes into contact with the metal, a driving force is generated for the metal to oxidize and form the iron oxide (FeO) molecule [50].

Reactions occurring in the substrate material during the firing of glass-ceramic coating.

$$Fe_3O_4 \rightarrow Fe^{2+} + 2Fe^{3+} + 4O_2 \tag{3.1}$$

$$2Fe^{3+} + Fe \rightarrow 3Fe_2 \tag{3.2}$$

Fe reduces CoO (cobalt oxide) and NiO (nickel oxide) molecules in glass-ceramic coating composition to obtain metallic cobalt and nickel.

$$Fe + CoO \rightarrow FeO + Co \tag{3.3}$$

$$Fe + NiO \rightarrow FeO + Ni \tag{3.4}$$

As you move along the bottom of the Ellingham diagram, the oxygen affinity of the compound increases. At the heating point of glass-ceramic, iron exhibits a stronger oxygen affinity compared to nickel and cobalt, as illustrated in Figure 3.1. Consequently, cobalt and nickel are predominantly utilized to impart adhesive qualities [50], [51].

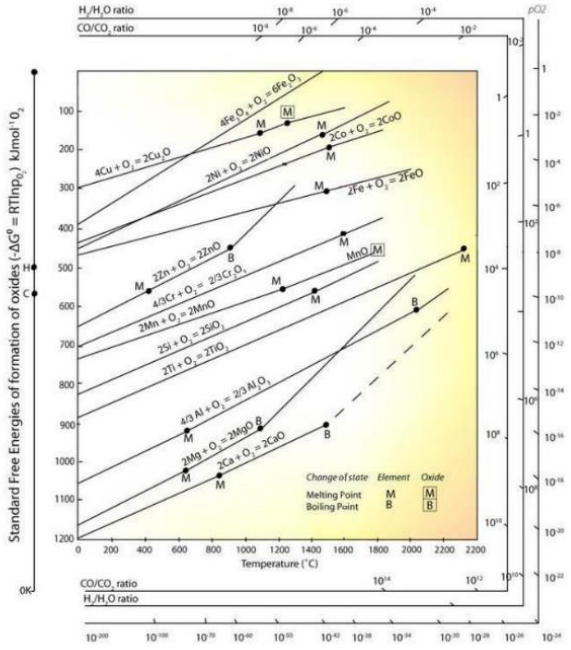


Figure 3.1 Ellingham Diagram [52]

3.2.3 Mechanical Theory

Mechanical theory centers around the contact area between the substrate and the coating [35]. In this approach, the surface of the metallic substrate undergoes chemical treatment using hydrochloric acid (HCl) and sulfuric acid (H_2SO_4), along with mechanical treatment. These treatments collectively enhance the contact between the glass-ceramic coating and the substrate [51].

3.3 Properties of Glass-Ceramic Coatings

3.3.1 Thermal Properties

3.3.1.1 Thermal Expansion

Thermal expansion refers to the increase in volume or length of materials with a rise in temperature. Essentially, it involves observing the changes in volume or length that occur in a substance with a one-unit temperature change. The thermal expansion coefficient is a parameter derived from the ratio of unit shape change to the temperature difference. Specifically, the linear thermal expansion coefficient (α) quantifies the change in the length of a material when the temperature increases by 1°C and is calculated using the following equation.

$$\alpha = \frac{1}{l} x \frac{\Delta l}{\Delta t} \tag{3.5}$$

where l is the length of the material, and Δl is the elongation obtained by means of heating through Δt°C

The change in volume of a material when the temperature increases by 1°C is described by the volume thermal expansion coefficient. In isotropic bodies like amorphous structures and glasses, the relationship between the volume thermal expansion coefficient (β) and the linear thermal expansion coefficient (α) is explained as follows: the volume expansion coefficient (β) is three times the linear expansion coefficient (α) in isotropic materials, expressed by the equation:

$$\beta = 3\alpha \tag{3.6}$$

The significance of the thermal expansion coefficient in enamels is tied to the bond between the enamel and metal. In enamel technology, it is imperative that the thermal expansion coefficients of the enamel and the substrate metal closely match. If the enamel coating has a lower thermal expansion coefficient than the metal, it will rapidly contract

during cooling after firing, as the enamel cools at a faster rate. A strong bond between enamel and metal, as indicated by enamel adhesion parameters, can resist enamel shrinkage on the metal surface. However, this resistance may lead to stress-induced cracks in the enamel structure if the tensile strength is exceeded. Conversely, if the metal's thermal expansion coefficient is less than that of the enamel, chipping defects may occur due to the enamel's higher compressive strength. Given that compressive strength is 15-20 times more critical than tensile strength, enamel coating applications typically prefer the expansion coefficient of the enamel to be less than that of the metals [43], [45] The volume thermal expansion coefficients of some metals and enamels are provided in Table 3.3.

Table 3.3 Cubical thermal expansion coefficients of some enamels and some metals [43]

Substrate Material	**Cubical Thermal Expansion Coefficient ($3\alpha x 10^{-7}$)**	**Temperature Range (°C)**
Iron	426	0 – 500
Low Carbon Steel	465	27 – 760
Cast Iron	378 – 390	20 – 500
Ground Coat for Steel	240 – 300	0 – 100
Cover Coat for Steel	280 – 360	0 – 100
Ground Coat for Cast Iron	250 – 300	0 – 100

3.3.1.2 Thermal Shock

The thermal shock resistance in enamel coatings indicates the behavior of the enamel in sudden temperature changes and is calculated mathematically according to the proposal of Winklemann and Schott:

$$K = \frac{P}{\alpha.E}\sqrt{\frac{\lambda}{c}}.d \tag{3.7}$$

where σ is tensile strength, α is the linear expansion coefficient, E is the elasticity modulus, λ is thermal conductivity coefficient, c is the specific heat and d is the density.

Thermal shock resistance is influenced not only by specific thermal properties but also by various other parameters, with internal strains playing a crucial role. The enamel's lower coefficient of thermal expansion compared to the metal induces compressive strains during rapid heating and tensile strains during rapid cooling. Enamels exhibit superior thermal shock resistance during rapid heating because compressive forces are weaker than tensile forces. The magnitude of the strains is also significant, with convex surfaces experiencing more tension than concave surfaces, resulting in lower thermal shock resistance for convex surfaces. Additionally, enamel thickness and substrate metal thickness play a role in thermal shock resistance [43].

As mentioned earlier, the thermal shock resistance of enamels is less effective during rapid cooling. Nevertheless, the cooling environment also plays a crucial role. Thermal shock resistance with cold air is generally less than thermal shock with cold water. Therefore, tests analyzing the thermal shock resistance of enamel coatings are often conducted using cold water [53].

3.3.1.3 Thermal Conductivity

The thermal conductivity of enamels holds significant importance in both industrial and scientific contexts. Efficient heat transmission through enamel is a crucial requirement for various applications, especially in kitchen equipment. It is a desirable property in military, construction, refrigerator, and oven applications, serving as a reflector or emitter. The enhancement of thermal conductivity in enamels can be achieved by incorporating oxides with high thermal conductivity, such as metal powders, into the composition.

Thermal conductivity is a magnitude of the thermal conductivity coefficient and is calculated as follows:

$$\lambda = p_1.\lambda_1 + p_2.\lambda_2 + p_3.\lambda_3 \quad (3.8)$$

Where λ is thermal conductivity, p represents percentage of oxide and λi represents thermal conductivity of that metal oxide.

The thermal conductivity of enamels varies between 0.84 and 1.26 watts/m.deg, depending on the composition. The presence of bubble structures in enamel significantly

influences thermal conductivity. An increase in the bubble structure leads to a decrease in thermal conductivity. This phenomenon can be attributed to the thermal conductivity of oxygen (O) being 28.5 and nitrogen (N) being 27.7 milliwatts/m.deg (at 50°C) [45]. This correlation is illustrated in Table 3.4. Additionally, low thermal conductivity has a negative impact on thermal expansion.

Table 3.4 Bulk densities and coefficient of thermal expansions of some enamel types [22]

Enamel Type	**Bulk Density (kg/dm^3)**	**Coefficient of Thermal Conductivity (watt/m.deg at40 °C)**
Ordinary	2.48	1.17
With some bubbles	2.45	1.09
With many small bubbles	2.36	1.05
Slightly foamed	2.28	0.8
Foamed	2.16	0.46

3.3.1.4 Fusibility and Fluidity

Fusibility and fluidity properties are crucial characteristics that come into play during the melting of enamel raw materials and the subsequent firing after application. While these properties are influenced by chemical composition, their calculation has generally remained experimental, with most attempts being valid only within certain composition ranges. Therefore, specific tests have become essential for each enamel composition, including the cone fusion test, fusion flow test, fusion block test, bead test, and interferometer test. The cone fusion test provides information about deformation intervals, the fusion flow test indicates the temperature-related hardness and softness of the frit, the fusion block test determines the fusion temperature of enamel compositions, the bead test evaluates frit's fusibility, fluidity, and surface tension properties, and the interferometer test measures the expansion coefficient [45].

3.3.1.5 Viscosity

Figure 3.2 illustrates that the enamel coatings' viscosity is a crucial parameter, as with all glassy materials, and is significantly influenced by temperature. Even a slight change in temperature can result in a substantial alteration in viscosity. The Tg temperature on the graph signifies the point at which the material becomes brittle, reaching a viscosity of 10^2 N.sec/m². Meanwhile, Ts indicates the melting temperature, corresponding to a viscosity value of 10 N.sec/m².

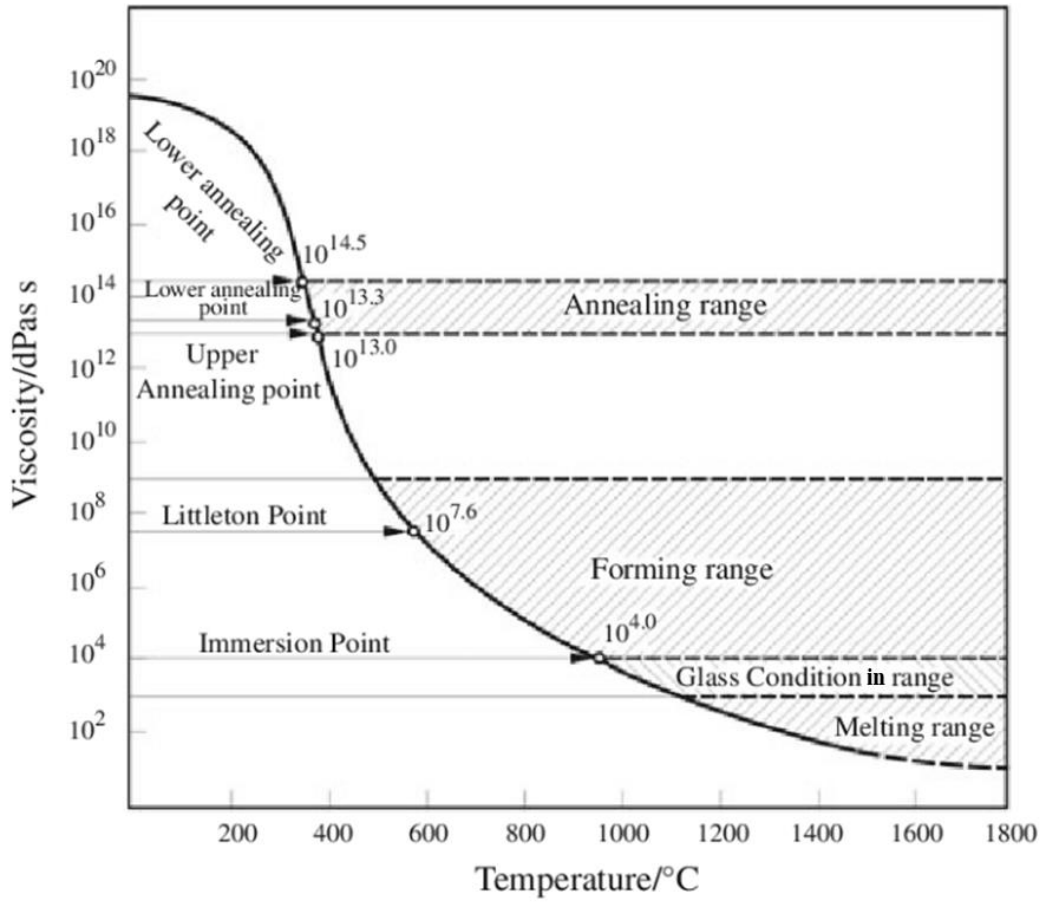


Figure 3.2 Viscosity – Temperature curve for a theoretical glass [30]

The values for Tg (glass transition temperature) and Tm (melting temperature) in enamels can typically be determined based on the chemical composition. Tg temperature is generally below 500°C, while Tm temperature is around 1400°C. Additionally, an increase in viscosity results in higher firing temperatures, reduced gas evolution, and improved surface flatness. On the contrary, low viscosity values may lead to enamel defects and uneven coating thickness. Throughout the firing process, enamel viscosities typically fall within the range of 10^2 to 10^3 N.sec/m² [45].

In wet applications of enamel coating process, the viscosity values of the prepared enamel slurry can be easily adjusted with materials such as boric acid, clay and sodium nitrite.

3.3.1.6 Crystallization

The ability to impart desired physical and chemical properties to enamels based significantly on the crystallization process, which involves nuclei, crystal growth, solubility, and supercooling. In enamel coatings, crystal formation occurs during the melt process, similar to glass and ceramic production processes. However, the frit structure formed during rapid cooling is entirely amorphous. Crystal formation is subsequently observed during the firing process, with the nucleus being the primary entity for crystal formation. The formation of the nucleus involves approximately 25 atoms or molecules coming together to create the initial aggregation, requiring energy and mobility [45].

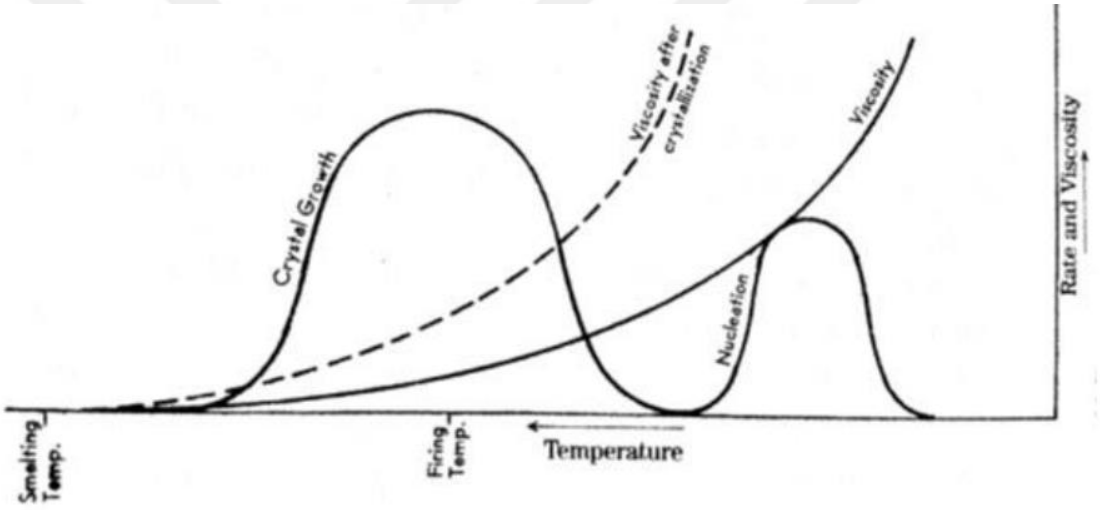


Figure 3.3 Rate – Viscosity and Temperature graph of the enamels during firing process [45]

The formation of nuclei is an endothermic reaction as the nuclei possess greater binding energy than the nuclei, whereas crystal formation is an exothermic reaction, involving the release of energy to attain a stable state [45]. Figure 3.3 illustrates the crystal formation of titanium, zircon, and fluoride enamels.

3.3.2 Physical and Mechanical Properties

3.3.2.1 Density

The density (specific gravity) property is commonly employed to monitor the fluidity of the sample in wet applications. Enamels are typically thinned based on the density measured using a pycnometer. The density of enamels is determined by the formula:

$$S = \frac{(w-p)}{[(w-p)-(w_2-w_1)]} \quad (3.9)$$

where S is the specific gravity of enamel, w is the weight of the tapered pycnometer and sample, w_1 is the weight of the tapered pycnometer filled with water, w_2 is the weight of the tapered pycnometer, sample, and water, and p is the weight of the tapered pycnometer [45]. This measurement is also known as powder density.

3.3.2.2 Specific Heat

The specific heat (Q) is the amount of heat required to increase the temperature of the material weighing 1 kg in constant pressure and constant volume by 1°C. The specific heat of enamels can be calculated with the following formula:

$$Q = p_1.s_1 + p_2.s_2 + p_3.s_3 \ldots \quad (3.10)$$

where Q is the specific heat of the enamel, p is the percentage of the oxide and s is the factor for the oxide [45].

3.3.2.3 Hardness

The hardness values of enamels exhibit minimal variation based on the chemical composition, and according to the Mohs scale, enamels generally fall within the hardness range of 5 to 6. Traditional hardness measurement methods like Rockwell, Brinell, and Knopp are not commonly employed for enamels due to their limited effectiveness in this context. The Mohs scale is often utilized to assess the scratch resistance of enamels [45].

3.3.2.4 Elasticity

Although the elasticity property is an important feature in materials, its use in enamel field is not common. It can be analyzed by mechanical and sonic methods. The mechanical method uses the following mathematical formula:

$$E = \frac{4PL^3}{bd^3\Delta} \quad (3.11)$$

where P is the load, L is the length of the material, b is the width, d is the thickness and Δ is the deflection [45].

3.3.2.5 Compressive Strength

The compressive strength of enamels is typically an overlooked property and serves as an auxiliary parameter that can influence other characteristics. For standard enamels, the

compressive strength falls within the range of 77 - 81 kg/mm^2 and can be calculated using the factor proposed by Winkelmann and Schott [45].

3.3.2.6 Tensile Strength

While the tensile strength of enamels is a significant property, its analysis proves challenging due to the brittle fracture nature of enameled materials, making them prone to breaking. Various methods have been proposed for its analysis, even though it is not a directly desired or analyzed property. Tensile strength has notable effects on the thermal properties, particularly the thermal expansion, of enamels [45].

3.3.2.7 Impact Resistance

Glass-ceramics exhibit remarkable impact resistance due to their unique microstructure, which combines both amorphous glass and crystalline phases. The controlled crystallization process during production enhances the toughness of these materials, thereby improving their ability to absorb and dissipate energy upon impact. This enhanced toughness is attributed to the presence of fine, uniformly distributed crystalline phases within the glass matrix, which act to hinder crack propagation. As a result, glass-ceramics are less susceptible to brittle failure compared to conventional glasses [9], [54].

3.3.2.8 Abrasion Resistance

The abrasion resistance property of enamels is a critical mechanical characteristic that significantly influences the material's durability. Enamels are consistently subjected to various types of abrasion, depending on their location. For instance, enamel coatings in kitchenware are frequently exposed to abrasion from metallic utensils such as spoons, scoops, knives, and wires. This constant exposure can lead to the deterioration of essential surface properties in enamels.

As scratches on the surface increase, the initial impact is the loss of color and gloss, resulting in enamels losing their aesthetic properties. With continued abrasion, it can extend to the metal-enamel interface. Complete deformation of the enamel due to abrasion, even in a small area, exposes the metal and the external environment to interaction, initiating metal corrosion. Ongoing corrosion may eventually lead to the complete removal of the coating.

Moreover, in kitchen applications, direct contact of food with metal due to abrasion on food contact surfaces can introduce elements from the metal into the human body through

food, potentially causing illness. Therefore, the abrasion resistance property in enamels is crucial. This property is dependent on factors such as the chemical composition of the enamel, its glass-ceramic structure, surface roughness, and the presence of bubble structures. Tests like Taber-branded abrasives and falling abrasive tests can be employed to evaluate the abrasion resistance property [45].

3.3.3 Chemical Properties

3.3.3.1 Acid Resistance

Enamels, particularly in kitchenware applications, are frequently exposed to acid attacks. One of the crucial oxides influencing acid resistance is SiO_2, given its role in maintaining the structure's continuity {[SiO_4]} in the enamel. The [SiO_4] tetrahedra surround {[AlO_4] - R+} and {[BO_4] - R+]} to resist the corrosive impact of acids. Therefore, an increase in SiO_2 content in the enamel recipe enhances acid resistance. Conversely, an increase in the R2O group in the structure disrupts the continuity of [SiO_4] tetrahedra due to the Si-R-O structure formed by ions like Li^+, Na^+, and K^+, resulting in decreased acid resistance [45], [55].

3.3.3.2 Alkali Resistance

Enamels can be exposed to alkaline attacks depending on their area of use. However, alkaline attacks typically occur more slowly compared to acid attacks. Consequently, tests for the alkali resistance of enamel tend to last longer. Moreover, when comparing acid and alkaline solutions, the impact of corrosive materials leading to ion exchange leaching in the enamel structure is generally lower. Testing is typically conducted using solutions such as sodium pyrophosphate, sodium hydroxide, and sodium bicarbonate.

The ion exchange leach of enamel is made with hydrogen ions in the solution, which reacts with the enamel matrix and causes the ionization of the alkaline ions in the enamel. This reaction is pH related and usually takes place at pH < 9 [45].

The reaction between hydrogen ions and a silica network with two non-bridging oxygen produces alkaline ions in the solution. This means that hydrogen will be easily replaced by any of the alkali metal ions bound by non-bridged oxygen and will form an aqueous surface layer.

The dissolution of the silicate structure typically occurs at a pH greater than 8 initially, and this dissolution tends to increase as the pH rises. At these pH levels, the hydroxyl

groups (OH) react with the hydrated layer or glass matrix. Subsequent reactions of hydroxyl groups with the initial product result in the formation of Si(OH) molecules that enter the alkaline solution. The second product, SiO^-, reacts with water in the $SiO^- + H_2O \rightarrow Si\text{-}OH + OH^-$ reaction. Consequently, the enamel undergoes erosion due to repeated reactions with hydroxyl groups [45].

3.3.3.3 Water Resistance

Enamels exhibit resistance to water at room temperature and remain structurally unaffected. Moreover, exposure to hot water typically does not significantly impact the enamel structure. However, prolonged and continuous exposure to high temperature and pressure at the point of use can initiate losses in the enamel structure [45]. According to tests conducted in accordance with the DIN EN ISO 4753-3 standard, enamel coatings should not exceed 8 mg/m^2 after tests conducted over 21 + 21 days (total 42 days) [2].Water resistance holds significance in applications such as thermosiphon systems, valves, and boilers.

4
ENAMEL COATED METAL SURFACES

Enamel coatings can be applied to various metal surfaces, including aluminum, gold, copper, cast iron, low carbon steel, decarburized steel, interstitial-free steel, titanium-stabilized steel, cold-rolled steel, and hot-rolled steel. However, variations exist in firing temperatures, melting temperatures, and chemical composition during the enameling process for these metal substrates. Consequently, the types of steel most commonly utilized in the industry for enameling are specifically highlighted.

4.1 Cast Iron

Cast iron serves as a prevalent substrate for enameling due to the adherence facilitated by the adhesive nature of the oxide layer and mechanical interlocking between cast iron and enamel. In the enameling industry, grey cast iron is predominantly favored, boasting various compositions. The limit chemical composition of cast irons for enameling is detailed in Table 4.1.

Table 4.1 Limit composition of cast iron for enameling applications [45]

Element	Percentage (%)
Total C	3.25 – 3.60
Graphitic C	2.80 – 3.20
Si	2.25 – 3.00
Mn	0.45 – 0.65
P	0.60 – 0.95
S	0.05– 0.10

Cast iron enamels exhibit distinctions from steel enamels, primarily in the adhesion mechanism. The adhesion between cast iron and enamel is predominantly mechanical,

attributed to the penetration of enamel into the pores of the rough surface of cast iron. In contrast, the adhesion mechanism between steel and enamel is mostly chemical [20].

Additionally, the components of cast iron, such as phosphorus (P) and silicon (Si), indirectly enhance adhesion by positively influencing the cast iron solidification process. This effect is attributed to either the carbon equivalent (Eq. 4.1) or the favorable chemical interaction of phosphorus and silicon with the enamel structure [20].

$$C_{eq} = C_{total} + \frac{Si+P}{3} \tag{4.1}$$

4.2 Decarburized Steel

Decarburized steels are the most suitable steels for enamelling process and can be used even for direct cover coat applications. Boiling defects, carbon gases formations and fish scale defects that occur after enamelling and during firing do not occur in this type of steel [45].

4.3 Low Carbon Steel

These steels are characterized by low carbon content (ranging from 0.002 to 0.004%) and are aluminum-killed steels that contain 0.15 - 0.30 wt.% Mn, with a maximum of 0.015 wt.% P, 0.015 wt.% S, and 0.015 wt.% Si. Additionally, up to 0.006 wt.% boron can be incorporated to address the fish scale defect observed during enamel coating and to regulate grain size. Typically, these steels exhibit a yield strength between 172 - 221 MPa, a tensile strength of 303 - 338 MPa, and an elongation ranging from 38 - 46%. An essential consideration is the absence of defects on the steel surface, ensuring it is suitable for acid washing [45].

4.4 Interstitial Free Steel

These steels are known for having all carbon and nitrogen in the structure bonded with alloying elements. Typically, titanium, niobium, or a combination of titanium and niobium are utilized as alloy elements for this purpose. They generally exhibit a yield strength ranging from 138 – 165 MPa, a tensile strength of 290 – 317 MPa, and an elongation between 41 – 45% [45]. It is crucial to note that the titanium ratio can negatively impact the adhesion of enamel to the steel. Therefore, the enamel composition

must be carefully prepared, taking this factor into account. An example of interstitial free steel composition was given in Table 4.2.

Table 4.2 Chemical composition of a commercial IF steel [56]

Generic Name	Max. Content (%)								
	C	Si	Mn	P	S	Al	Ti	Nb	Cu
IF180	0.01	0.3	0.7	0.06	0.025	≥ 0.01	0.12	0.09	0.2

4.5 Stainless Steel

Stainless steels, characterized by an average chromium (Cr) content of 18 wt.% and nickel (Ni) content of 8 wt.%, are widely utilized due to their excellent corrosion resistance properties, leading to a broad range of applications in kitchen utensils. The 400 series stainless steels, with their ferritic structure, facilitate the application of low-temperature enamels. However, the 200 series (Cr-Ni-Mn) and 300 series (Cr-Ni) stainless steels, being austenitic, pose challenges in the enameling process due to their high thermal expansion coefficient. Specialized enamel studies are required to overcome these challenges. Studies have shown that mechanical activation of the surface can enhance adhesion, and successful enamel coating has been achieved on 316L stainless steels to prevent oxidation at high temperatures [56], [57].

4.6 Coating Methods for Glass-Ceramic Coatings

4.6.1 Metallic Surface Preparation

4.6.1.1 Mechanical Cleaning

Mechanical cleaning typically involves abrasive action on the surface, where impurities are dislodged by impacting particles, creating a rougher metal surface. The increased surface roughness enhances the specific surface area available for reactions between the enamel and the metal surface, providing more opportunities for adhesion. Key parameters in sandblasting, a commonly used technique for mechanical cleaning, include particle size, particle size difference, and applied pressure [45].

4.6.1.2 Chemical Cleaning

Chemical cleaning involves several interdependent steps, with the initial step being degreasing. This process is undertaken to eliminate oil, rust-preventing oil, and various types of rust. Several critical parameters in the degreasing process include:

- Type of degreasing agent
- Degreasing temperature (must be between 60°C – 90°C)
- Concentration of the agent (must be between 45 – 50 g/L)
- pH of the baths
- Treatment time (approximately 15 min)
- Mechanical action (spraying pressure)

After this process, the subsequent steps involve hot water rinsing, cold water rinsing, and final rinsing with demineralized water before moving on to the pickling step [58]. Pickling with acid aims to remove rust and scale from the metal surface by inducing a reaction between the acid and the rust. This reaction results in the formation of hydrated ferric oxide ($Fe_2O_3.2H_2O$), anhydrous ferric oxide (Fe_2O_3), and magnetic iron oxide (Fe_3O_4) as products. Additionally, the acid solution facilitates the release of hydrogen gases that remain dissolved in the metal. Sulfuric acid (H_2SO_4) is one of the acids commonly used for this purpose, and the metal surface is slowly cleaned in a process involving a 6% H_2SO_4 solution at 66°C. However, ions such as H^+, SO^{4-}, and SO_4^{-2}, produced by the low ionization of H_2SO_4, react more rapidly with the surface. Temperature is a crucial factor influencing reaction mobility and rate. As the acid solution diminishes with repeated processes, it is necessary to change the solution after a certain pickling period. While hydrochloric acid (HCl) can be used for pickling, its application is infrequent due to the need for heating and high concentration. Phosphoric acid (H_3PO_4) is known for its superior effect on enamel quality in this context, but its use is limited by its cost and is typically employed in one-coat-one-fire white enamel applications[45]. Various cleaner components can be used for cleaning, and these are listed in Table 4.3.

Table 4.3 Some cleaner components and their function in chemical surface cleaning before the enamelling application [43]

Component	**Function**
Silicates • Sodium metasilicate (Na_2SiO_3) • Sodium orthosilicate (Na_4SiO_4)	Softening the water by precipitation Good dispenser and saponifier Inhibition of Al and Zn dissolution High alkalinity property
Phosphates • Trisodium phosphate (TSP-Na_3PO_4) • Sodium tripolyphosphate (STPP-$Na_5P_3O_{10}$) • Tetrasodium pyrophosphate (TSPP –$Na_4P_2O_7$) • Disodium phosphate (DSP-Na_2HPO_4)	Softening the water Improving rinsing
Carbonates • Sodium carbonate (Na_2CO_3)	Good buffering Good alkalinity property
Hydroxides • Potassium hydroxide (KOH) • Sodium hydroxide (NaOH)	Source of alkalinity
Nitrites • Sodium nitrite ($NaNO_2$)	Prevents the oxidation due to drying process
Chelants • Ethylenediaminetetraacetic acid($C_{10}H_{16}N_2O_8$)	Softening the water Prevention of metal ion deposition

After the cleaning process, metal surfaces undergo a rinsing procedure. The chemicals or their by-products utilized during cleaning may leave a thin layer on the metal surface or reside in the surface pores. Rinsing is essential after each washing step and is carried out through hot water rinsing followed by cold water rinsing. Subsequently, the metals are immersed in a neutralization bath where an alkaline solution (such as soda ash, borax, or trisodium phosphate mixed with water) is used to completely eliminate the last traces of acid. Maintaining a solution temperature of 60 - 70°C is recommended. In the final step, the metals proceed to the drying phase, where they are rapidly dried to eliminate dust and scale, leaving them ready for subsequent processes [45].

4.7 Coating Methods

4.7.1 Spraying Technique

This method involves manual or fully automatic coating systems equipped with a spray gun and a booth. The process revolves around propelling enamel slurry particles through a narrow opening (nozzle) to the opposite side (metal plate) using air pressure. It is crucial to ensure that the slurry particles are neither too fast nor too slow, and that there are no air gaps present. Typically, air pressure falls within the range of 4.1 atm to 6.8 atm [45].

An ideal spray gun has the following properties.

- Nozzle hole: 1.8 - 2.4 mm
- Spray Pressure: 2.8 - 3.5 atm.
- Enamel Flow: 36 - 48 L/h
- Air Consumption: 30 - 35 m^3/h
- Optimum distance to enamel parts: 30 - 50 cm

4.7.2 Dipping

This technique operates on the immersion principle, involving the submersion, removal, and filtering of the work piece in a tank filled with enamel slurry. While material loss is minimal, challenges may arise when coating large or shaped parts. Additionally, the slurry in the tank tends to settle over time, accumulating water. To address this, a mechanical mixer is employed to agitate the bottom of the tank, ensuring a uniform slurry for application [45].

4.7.3 Flow Coating

In the continuous flow enamel slurry process, the parts being coated are typically smaller and less shaped. This method is commonly employed for applying the ground coat in 2C1F (two coats, one fire) applications. It is the preferred choice for cover coat applications that require a ground coat, as water on the surface can lead to water trace defects in the ground coats [45].

4.7.4 Electrostatic (Wet) Spraying

While the electrostatic application of enameled slurry particles is technically feasible by transferring charged particles to a metal sample with an opposite electric charge, it is not commonly preferred for manual application due to the high electric current involved. This method is typically avoided in manual processes. However, it can be utilized in automated systems where the coating can be applied homogeneously and without defects [45].

4.7.5 Electrostatic Powder Spraying

Enamel powder obtained from the mill or frit composition is negatively charged by passing near a high-potential electrode. This sets up an electric field between the high-potential spray gun and the work piece, leading to local ionization of the air in the environment. As a result, oxygen ions in the surroundings become negatively charged, and enamel powder also acquires a negative charge in the air. Guided by the electric field, enamel powder and air move toward the work piece. During this process, four different forces influence enamel powders: electrical force, mechanical force, air resistance, and gravity. The operation is conducted at 100 kV voltages and very low amperes. Typically, the enamel coating at the end of the process is uniform. Smaller powder particles are more easily charged with electric charge, enhancing the adhesion of the enamel to the surface. Additionally, dust particles that do not adhere to the part or disperse in the air can be recycled in this method [45].

4.7.6 Electrophoretic Coating

In this method, the metal plate to be coated serves as the positive electrode. Both positive and negative electrodes are present in the enamel slurry bath. When the metal substrate is exposed to a potential of 50 V and 50-300 A/m^2 in the enamel slurry, it attracts the charged frit particles collected in the coating layer. The most crucial parameters influencing coating quality include the density of enamel, particle size, and the amount of power

applied. The enamel density should be approximately 1.5 g/cm^3. While coating thickness increases with higher applied voltages, surface defects may occur due to gas evolution at very high voltages [45].

4.7.7 Thermal Spray Coating

In this coating method, powder frits or enamel powder are injected into the plasma jet, melted, and applied to a material to be coated. The melted frit is sent to the surface at a speed of approximately 100-200 m/sec through the spray gun. The distance between the surface and the gun is typically between 100 and 150 mm. Frits exit the gun at a temperature close to 1500°C, and when they adhere to the surface, their temperature rapidly decreases to 270°C due to sudden direct cooling. The temperature then drops to 90°C and finally to 40°C. This method requires careful execution, but when it is performed properly, it can yield the best results compared to other coating methods [59].

4.8 Coating Process

4.8.1 One Coat One Fire

This method, abbreviated as 1C1F, is utilized for ground coat applications, indicating that the enamel is applied to the surface once and fired once. It is the most basic method, and both wet and electrostatic powder methods can be employed in this process [45].

4.8.2 Two Coat Two Fire

It is abbreviated as 2C2F, representing the applications of cover coats. This method involves applying the first coat, the ground coat, firing it, and then applying and firing the second coat, the cover coat. The application methods, either wet or powder, can vary. For instance, after applying the ground coat as a powder, the cover coat application can be done using the wet method, and vice versa [45].

4.8.3 Two Coat One Fire

It is referred to as 2C1F, indicating that the ground coat is not fired after application, but the cover coat is applied, and then both layers are fired together. This method is significant because it reduces energy consumption, making it suitable for industrial applications [45].

Typically, after applying the ground coat with the wet application method in a thickness of 40 - 80 μm, it is not fired but only dried, resulting in a form known as a biscuit.

Although the biscuit form may appear hard, it lacks resistance to impacts. The cover coat for the biscuit form is usually applied using the powder method, and the coating is fired at the firing temperature. It is crucial that the ground coat must not be visible from the cover coat or cause black dot defects.

4.8.4 Three Coat Two Fire

The 3C2F system is generally based on the principle of bringing the ground or intermediate layer (first cover coat) into a biscuit form and then firing it. This process is optimized compared to the 2C1F system. However, it is crucial that the thermal expansion coefficients of the layers applied are very close to each other; otherwise, cracking may occur in the coating [45].

4.8.5 Three Coat Three Firing

The 3C3F system mentions the firing method after each application. The important point here is that the thermal expansion coefficients of the enamel compositions coated are very close to each other and do not allow crystal growth within their body during reheating much. Otherwise, the material may lose its glassiness. In addition, internal stresses and the release of hydrogen and other gases from the metal surface have a negative effect on the coating quality [60]. Some of the industrially applied methods are given in the Table 4.4.

Table 4.4 Coating process techniques for some industrial application areas [33]

Processes	Boiler	Cookware	Kitchenware	Sanitaryware
1 coat / 1 fire dry	Yes	Yes	No	No
1 coat / 1 fire wet	Yes	Yes	Yes	No
2 coat / 1 fire dry/dry	No	Yes	No	Yes
2 coat / 1 fire wet/dry	Yes	Yes	No	Yes
2 coat / 1 fire wet/wet	No	Yes	No	Yes

Table 4.4 Coating process techniques for some industrial application areas (continued)

Processes	Boiler	Cookware	Kitchenware	Sanitaryware
2 coat / 2 fire dry/dry	Yes	Yes	No	Yes
2 coat / 2 fire dry/wet	Yes	Yes	No	Yes
2 coat / 2 fire wet/wet	Yes	Yes	Yes	Yes
3 coat / 2 fire wet/wet/wet or dry/wet/wet or dry/wet/dry or wet/wet/dry	No	No	No	Yes

5
CHROMITE

Chromium, one of the natural components of the earth's crust; It is one of the basic elements of metallurgy, chemistry, and refractory industries [34]. While some chromium-based minerals such as crocoite ($PbCrO_4$), vauquelinite ($Pb_2Cu[CrO_4][PO_4]$), uvarovite ($Ca_3Cr_2[SiO_4]_3$), and merumite ($4(Cr,Al)_2O_3 \cdot 3H_2O$) are well known, chromite ($FeCr_2O_4$) is the only one that is a commercially recoverable source of Cr [61].

Chromite is an oxide mineral belonging to the spinel group, a complex mineral containing magnesium, iron, aluminum, and Cr in varying proportions depending on the deposit. It can be represented as $FeCr_2O_4$ or $(Fe^{2+}, Mg)[Cr, Al, Fe^{3+}]2O_4$ [62]. The structure of chromite is formed by a nearly cubic close-packed array of oxygen atoms, with the aluminum atoms in octahedral coordination and the iron atoms in tetrahedral coordination It is shown in Figure 5.1 [63].

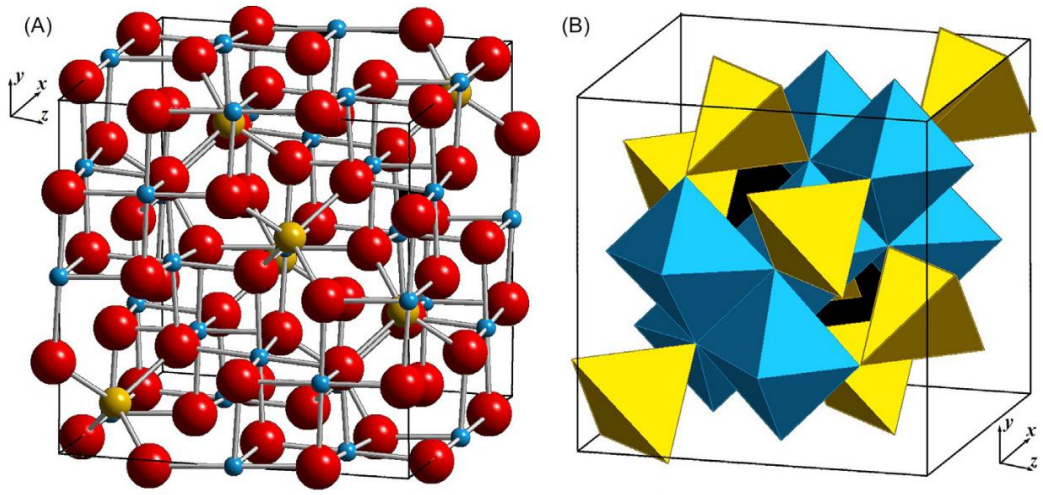


Figure 5.1 The spinel structure (A) as a ball and stick model and (B) as coordination polyhedra. In a) oxygen is red, the divalent atom (Mg is spinel, Fe in chromite) is yellow and the trivalent atom (Al in spinel, Cr in chromite) is shown as blue and at the center of the yellow tetrahedra

Chromite, the most important chromium mineral, is an oxide mineral consisting of chromium, iron, and oxygen ($FeCr_2O_4$). Magnesium often replaces iron in chromite. It has a metallic to submetallic luster and high specific gravity, appearing dark gray to black in color. Chromite can be challenging to identify, requiring consideration of color,

specific gravity, luster, and a characteristic brown streak when identified by hand sample. A significant clue in identifying chromite is its association with metamorphic rocks such as ultrabasic igneous rocks and serpentinite. The physical properties of chromite are stated in the Table 5.1

Table 5.1 Physical Properties of chromite [34][64]

Chemical Classification	**Oxide**
Formula	(Fe, Mg) Cr_2O_4
Colour	Dark gray to black rarely brown black
Gloss	Metallic to submetallic
Transparency	Opaque
Mohs Hardness	5.5-6
Crystal System	Isometric, octahedron, massive
Specific Gravity	4.0-5.1 g/cm^3

5.1 Chromite Mines

Commercial chromite deposits that are large enough for mining are generally found in stratiform deposits and podiform deposits. Other sources of chromite include laterites, which are weathering products of peridotite. Laterites are more widely recognized as sources of nickel and cobalt, historically serving as a minor source of chromite. Figure 5.2 presents a map showing the locations, geological types, and the size of global chromite resources and reserves [65].

The majority of the World's chromite resources occur as stratiform deposits in layered intrusions found in countries such as South Africa, Canada, Finland, and Madagascar. South Africa holds approximately three-quarters of the world's viable chromite reserves. Historic sources of chromite from podiform deposits are significant in Kazakhstan, Turkiye, and Albania. Zimbabwe stands out as the only country to exploit both stratiform and podiform deposits, as indicated in Figure 5.2 [66].

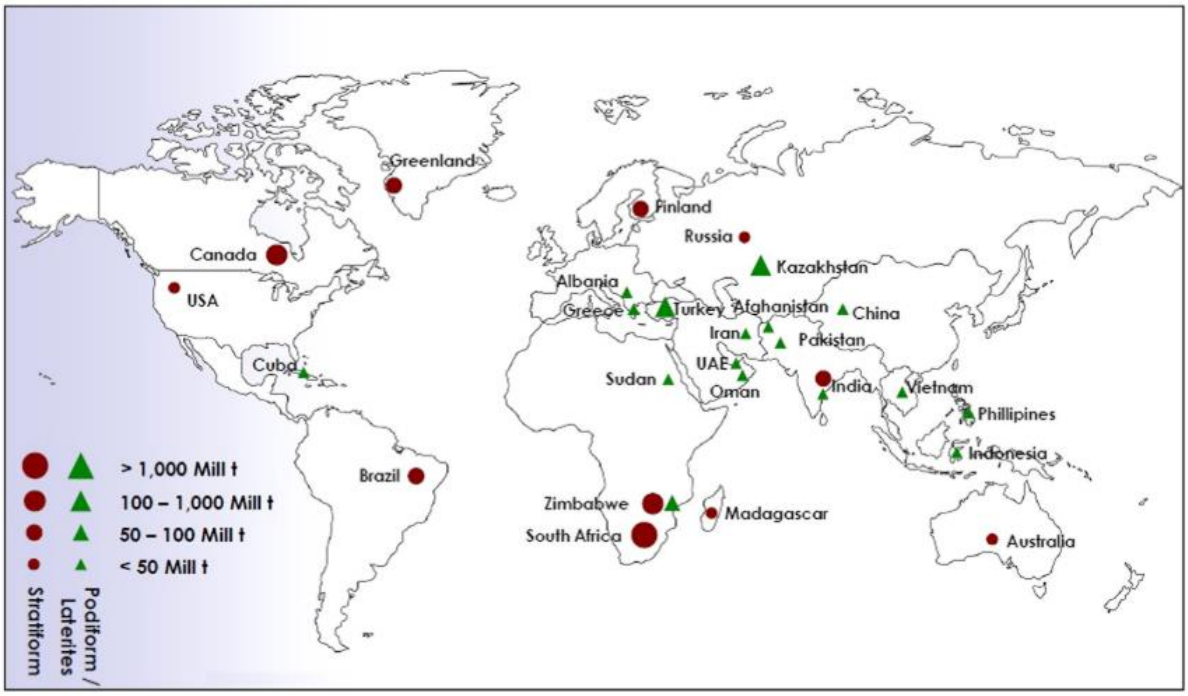


Figure 5.2 Map of locations, geological types, and size (millions of tons of Cr) of global chromite resources and reserves [67]

5.2 Chromite Ore Processing

A schematic diagram of Chromite ore processing is presented in the process flow diagram with chemical reactions involved (Fig. 5.3). Chromite ore, represented as $FeO \cdot Cr_2O_3$ in rock form, typically contains about 50–61% Cr_2O_3, 11–19% FeO, along with other minerals such as 9–16% MgO, 10–16% Al_2O_3, and 1–16% Fe_2O_3. This ore composition is generally available in association with other minerals. The process flow diagram provides an illustration of the steps involved in the processing of chromite ore, showing the chemical reactions in the extraction process.

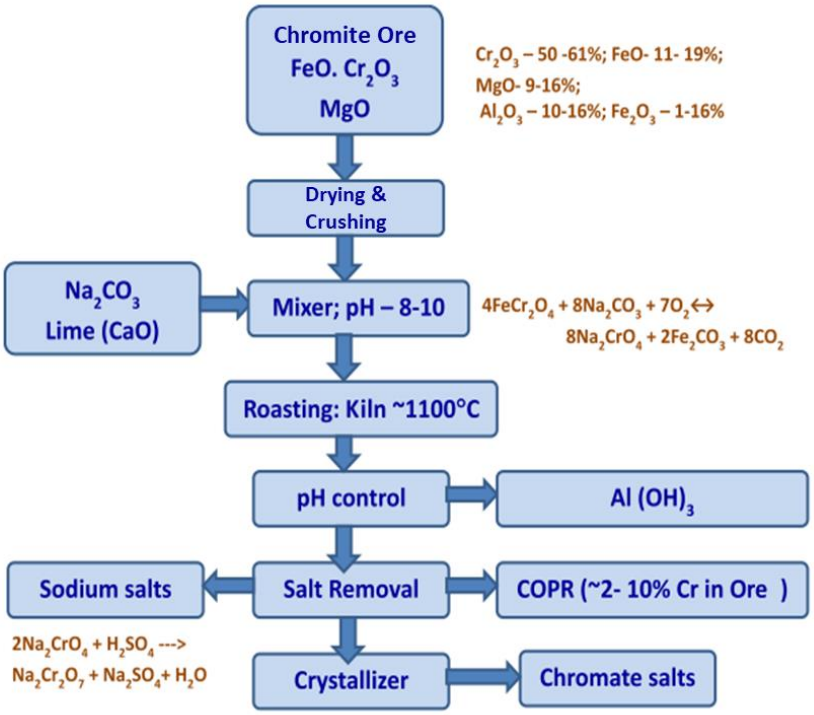


Figure 5.3 Schematic diagram of Chromite ore processing [68]

5.3 Chromium Effect on Environment and Human Health

Chromium is a metal long recognized for its toxic, mutagenic, and carcinogenic properties. It exerts toxic effects on microorganisms, plants, animals, and humans. In the environment, chromium exists in two stable forms: Cr(VI) and Cr(III). While Cr(III) is less toxic and insoluble, Cr(VI) is highly toxic and highly soluble. Natural sources of chromium in aquatic systems include the weathering of rock formations, atmospheric deposition, and runoff from surface soils. Rocks naturally contain high concentrations of chromium. Both trivalent and hexavalent chromium are significant within the Eh-pH range of natural water systems. Hexavalent chromium (Cr(VI)) is particularly toxic to plants and animals, functioning as a strong oxidizing agent, a corrosive substance, and a potential carcinogen. Despite its widespread use in various industrial applications, chromium presents a serious environmental threat. Industries such as mining, chrome plating, leather tanning, and dye manufacturing produce wastewater and solid waste with high chromium concentrations, which are major health hazards due to their contribution to environmental pollution. The leaching of industrial waste during landfill operations allows toxic chromium to migrate from soil to water bodies, thereby posing an environmental threat. The ferrochrome industry is among the largest contributors to

chromium contamination in aquatic environments. South Africa, possessing the world's largest chromium reserves, generates significant waste from its ferrochrome industry, including slag, dust, and processed water, all of which contain high concentrations of chromium and contribute to environmental pollution [69], [70]. Cr(VI) has a known carcinogenic effect on humans, Cr(III) is relatively less toxic [71]. Cr(VI) is known to have 100 times more toxicity than trivalent chromium in both acute and chronic exposures due to its high solubility and mobility in water as well as its easy reduction. Chronic human exposure to high levels of hexavalent chromium through inhalation or oral exposure can produce effects on the kidney, gastrointestinal and immune systems, and possibly the blood [72].

6
EXPERIMENTAL STUDIES

In this study, the potential use of mining waste as an alternative raw material in the composition of sodium borosilicate glass-ceramic system glass-ceramic coatings was explored. Furthermore, the study also investigated the adhesion of agents (such as NiO and CoO) facilitating the bonding of the glass-ceramic system to steel surfaces.

The experimental procedure begins with, a detailed characterization of the chromite ore processing residue (COPR), which constitutes the mining waste; secondly, precursor glasses are synthesized using a formulation with new complex compounds of the waste raw material and industrial compounds; and finally, the application of this glass as a coating on a steel substrate to produce a glass-ceramic coating. Comprehensive characterizations were performed on all COPR samples, precursor glasses (PG) and coatings (GCC). Figure 6.1 illustrates all the experimental processes of the study.

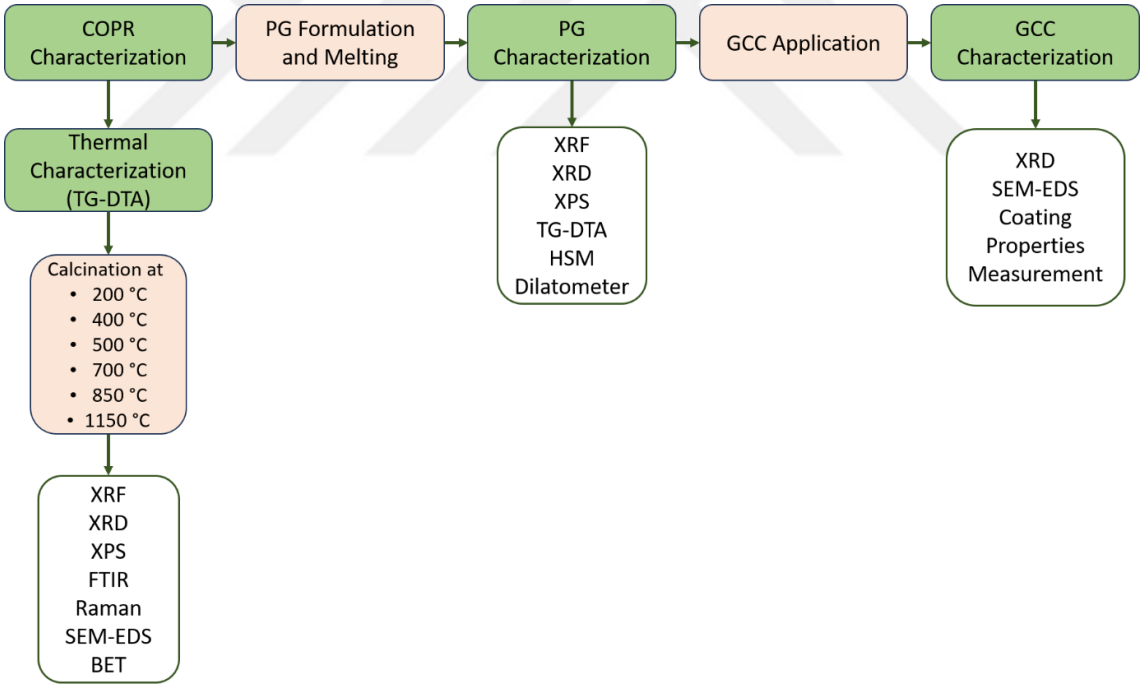


Figure 6.1 Experimental processes of the study

6.1 Materials

The Chromite Ore Processing Residue (COPR) waste was obtained from Adana, Türkiye. Akcoat Advanced Coating Chemicals & Co. supplied all essential raw materials, as well as access to the experimental equipment and characterization instruments.

6.2 COPR Characterization

The raw wastes were heat treated at 200°C, 400°C, 500°C, 600°C, 700°C, 850°C and 1150°C for observing the effect of heat during melting process. The calcination temperatures were decided from the critical points of thermal analysis which were used as operation values.

All samples were analyzed to determine different perspectives such as the composition, phases, microstructures, chemical bonds, and surface areas. The designation of the waste specimens is clarified in Table 6.1.

Table 6.1 Calcination condition explanation of samples

Sample Name	Calcination Temperature (°C)	Duration (min)
D-200	200	60
C-400	400	
C-500	500	
C-700	700	
C-850	850	
C-1150	1150	

D refers to Dried

****C refers to Calcination***

6.2.1 Chemical Analysis

X-ray fluorescence (XRF) (Bruker S8 Tiger WDXRF) analysis was performed for two main purposes; to examine the chemical composition of the supplied waste and to observe the differences between samples after calcination mainly in carbon and components. X-ray Photoelectron Spectroscopy (XPS) (Thermo Scientific K-Alpha) analysis was carried out to detect the potentially harmful Cr^{6+} component of the waste and to examine the effects of calcination on $Cr^{6+.}$

All samples were ground in a tungsten carbide ring mill (Rocklabs BenchTop Ring Mill Pulveriser; WC-Co ring) at 300 rpm for 30 seconds. After that sample powders were pressed into pellets in an automatic press Herzog HTP40 Automatic Pellet Press) for XRF and XPS analysis.

6.2.2 Phase Analysis

X-ray Diffraction (XRD) analysis was used to examine the phases it contains, and its phase transformations calcined COPR samples. The device is Bruker D8 Advance Diffractometer, and the analysis parameters are CuKα radiation, acceleration voltage 40 kV, current 25 mA and 2θ values of 10–80°.

6.2.3 Thermal Analysis

This analysis had a significant role of the characterization of COPR. Thermogravimetry-Differential Thermal Analysis (TG-DTA) analyzes were used to determine the thermal behavior of the wastes (Netzsch STA 449F1A-0207-M). Expected outputs of TG analysis; it is to determine the moisture content of the waste, to determine the amount of mass loss that will be caused by the removal of organic and volatile raw materials from the structure. Likewise, what is expected from the DTA analysis is, to give information about whether the reactions such as phase transformation, decomposition and crystallization are exothermic or endothermic reactions. Critical temperature points for the waste were determined by using the temperature changes during the reactions. Analysis were occurred at a heating rate 10°C/min to 1200°C and under a dry air. The samples were analyzed under a dry air atmosphere placed in alumina crucibles at a heating rate of 10°C/min to 1200°C. Hot stage microscopy analysis was conducted to investigate the glassing properties under heat.

6.2.4 Bonding-Structure Analysis

Spectroscopic characterization methodology was preferred to identify bonding structures, changes in bonds with the effect of temperature. In addition, the two different analysis preferences aim is to; clearly reveal the nature of the waste and calcination performance with correlated information. Fourier-transform infrared spectroscopy (FT-IR) analysis (Perkin-Elmer Spectrum Two FT-IR Spectrometer, ATR method) has occurred between 400 cm^{-1} and 4000 cm^{-1} wavelength range. Raman spectra is calculated by Kaiser Optical System Raman RXN1 with its own MR probe. Measurement parameters are 250 mV, 10 seconds, 785 nm laser wavelength and 150 - 1750 cm^{-1} spectral range.

6.2.5 Surface Area Measurements

The surface area of the supplied waste and the effect of calcination on the surface area were determined by Brunauer-Emmett-Teller (BET) analysis (NOVA Touch LX1 Quantachrome Instruments NOV Atouch) methods. BET analysis has an exclusive environment for analysis. The machine working principle is based on the adsorption of a gas. Degassing procedure was applied on the sample at 110°C for 10 hours with N_2 gas.

6.2.6 Microstructural Analysis

The morphology and elemental distribution of waste and calcined samples were examined by Scanning Electron Microscope-Energy Dispersive Spectroscopy (SEM-EDS) analysis (JEOL JSM-6060 LV equipped with IXRF EDS). Samples were characterized with SE mode. All samples were coated with Au-Pt (Quorum SC7620 - Mini Sputter Moater/ Glow Discharge System) for examine accurately.

6.3 Precursor Glass Synthesis

Mixture formulations were prepared considering the end product coating properties and the physical and chemical properties of the COPR waste. To investigate the behavior of the waste in the mixture and its affects on the final product, standard and waste-derived precursor glass structures were prepared using both waste-derived and 100% industrially sourced raw materials (such as magnesium oxide (MgO), quartz (SiO_2), iron oxide (Fe_2O_3), and others. All batches were mixed and melted for 60 min at 1300°C. The molten products were quenched by pouring them into water for the formation of precursor glasses, also commonly known as frit. The resulting granular frit compositions dried at

100°C for 24 h for be ready the milling step. Considering the proportional change of agents that provide adhesion with the metal during the synthesis of precursor glass structures, two standard and two different waste-derived precursor glass structures were synthesized. These structures featured varying NiO and CoO ratios. The standard precursor glass, predominantly featuring the NiO adhesion agent, was designated as PG-STD-Ni, while its waste-derived counterpart was labeled as PG-WD-Ni. Similarly, the CoO adhesion agent-dominant standard precursor glass was denoted as PG-STD-Co, and the waste-derived version was identified as PG-WD-Co. These identifications give in Table 6.2.

Table 6.2 Identification of precursor glasses

Sample Name	Explanation
PG-STD-Ni	Industrial raw material and NiO adhesion agent
PG-WD-Ni	Approximately 3.5 wt.% COPR and NiO adhesion agent
PG- STD -Co	Industrial raw material and CoO adhesion agent
PG-WD-Co	Approximately 3.5 wt.% COPR and CoO adhesion agent

PG refers to Precursor Glass

****STD refers to Standard***

*****WD refers to Waste Derived***

6.4 Precursor Glasses Characterization

Precursor glasses were examined the melting performance, chemical composition change, amorphous structure and harmony of thermal behavior between the coating substrate.

6.4.1 Chemical Analysis of Precursor Glasses

X-ray fluorescence (XRF) (Bruker S8 Tiger WDXRF) analysis was performed to evaluate the melting performance precursor glasses. Precursor glasses also were ground at 300 rpm for 30 seconds in a ring mill (Rocklabs BenchTop Ring Mill Pulveriser; WC-Co ring). Milled particles were sieved with a 35 micron sieve. After that sample powders were pressed into pellets in an automatic press Herzog HTP40 Automatic Pellet Press) for XRF

analysis. Additionally, lithium oxide (Li_2O) content of the frits were analyzed using Atomic Absorption Spectrometry (PG Instrument PG-990 AAS, UK).

XPS analysis was performed on grounded precursor glass (PG) structures to evaluate the success of the vitrification process in eliminating Cr element toxicity and to examine the effect of different adhesion agent content on the conversion of the Cr^{6+} component. Grounded powders were prepared in the same way for XPS and XRF analyses. Analysis parameters are AlKα radiation, pass energy mode, acceleration voltage 30 eV and 0-1350 eV range.

6.4.2 Crystalline Structure Analysis of Precursor Glasses

X-ray Diffraction (XRD) analysis was performed to determine the chemical composition and melting performance of the precursor glass powders. After the melting process the PGs were analyzed the effect of changing the raw material on phase transformations occurring during melting and cooling. The device is Bruker D8 Advance Diffractometer, and the analysis parameters are CuKα radiation, acceleration voltage 40 kV, current 25 mA and 2θ values of 10–80°.

6.4.3 Thermal Behaviour Determination of Precursor Glasses

In order to determine the behavior of the samples against heat; they were analyzed with a hot stage microscope (Misura3.32 ODTH HSM 1600-80, Italy). Compliance with DIN 51730 standards led to the analysis of $T_{Sintering}$, $T_{Softening}$, T_{Sphere}, $T_{Half\ Sphere}$, and $T_{Melting}$ temperatures, ranging up to 1250°C, with a heating rate of 10°C/min, accounting for geometric shape alterations.

The coefficient of thermal expansion (COE) was determined between 20 and 540°C, employing a dilatometric apparatus (DIL 402 PC Netzsch, Germany) equipped with a Pt-Pt/Rh thermocouple, fused silica push rod, and sample holder. A 5×5×5×25 mm piece was cut from the sample after pelletization for dilatometer analysis.

Thermal properties of glasses and the impact of COPR on frits' thermal characteristics were explored using Simultaneous Thermo Gravimetry-Differential Thermal Analysis (TG-DTA Netzsch STA 449F1A-0207-M, Germany). Thermogravimetry (TG) was observed weight changes, while differential thermal analysis (DTA) examined enthalpy changes associated with exothermic-endothermic reactions like glass-transition and crystallization temperatures. Simultaneous TG-DTA analyses involved 30 mg of frit

powder in an alumina crucible, heated to 1200°C at a consistent rate of 10°C/min in a nitrogen (N_2) atmosphere.

6.5 Milling and Coating Application

After the frits were produced, a grinding process was employed to obtain powder from frit granules. This process utilized a alumina-zirconia ball mill and alumina-zirconia balls. Three different-sized balls (Ø 5-25 mm) were employed, maintaining a ratio of 1:3 between the amount of ground material and the total ball weight. This procedure aimed to ensure homogeneous milling and achieve the desired particle size distribution. Following grinding, the mixture was sieved through 80 mesh (197 μm) sieves to attain a grain size suitable for electrostatic powder application (<200 μm). Electrostatic properties were imparted to the enamel coating frit powders by adding silicone oil (C_2H_6OSi) at a rate of 0.5 cc per 100 g of powder [44], [73].

Low carbon steel plates were utilized as the metal substrate in the study, adhering to the specifications outlined in the EN10209:2013 standard. Plates measuring 37 cm x 12 cm x 0.5 cm underwent surface cleaning before the coating process. Within the mechanical cleaning scope, samples were initially subjected to sandblasting, followed by cleaning with an industrial degreaser. After cleaning, the surface underwent hot water rinsing, cold water rinsing, neutralization, and drying steps. The coating process was executed through the manual electrostatic spraying method. Given the laboratory scale of the study, multiple furnaces were utilized in the firing process. Initially, the samples were dried in an oven at 100°C to evaporate internal water without distorting the structure. Subsequently, they were placed in the furnace at 550°C for 5 minutes, followed by firing at 830°C for 6 minutes. After removal from the furnace, the samples were allowed to cool to room temperature.

6.6 Glass-Ceramic Coating Characterization

The characterization studies were completed with the GCCs' microstructural evaluation, phase determination and coating properties.

6.6.1 Phase Determination of Glass Ceramic Coatings

X-ray Diffraction (XRD) analysis was evaluated GCCs phases. PGs powders were pelletized (30 mm diameter and 5 mm thickness) and were fired at 830°C for 6 minutes.

The fired pellets were ground in a ring mill and sieved through a 325 mesh (45 μm) sieve and GCCs were cut in a water jet for XRD analysis. The ground powders were sieved through a 325 mesh (45 μm) sieve and the GCCs (2 cm x 2cm) placed in the XRD holder. The device is Bruker D8 Advance Diffractometer, and the analysis parameters are CuKα radiation, acceleration voltage 40 kV, current 25 mA and 2θ values of 10 - 80°.

6.6.2 Microstructural and Elemental Analysis

Scanning Electron Microscope-Energy Dispersive Spectroscopy (SEM-EDS) analysis (JEOL JSM-6060 LV equipped with IXRF EDS) was used for microstructural analysis of the samples. After all coating processes, SEM-EDS analysis was performed on the coating surfaces to examine the surface morphology and determine the elemental distribution. Several metallographic procedures were applied to examine the coating-metal interface in SEM-EDS analysis; I) 10x10 mm parts were cut from the coated plates and cold moulded with epoxy, II) the cross-sectional surfaces were subjected to grinding (120-400-600-1200 μm) and polishing (5-3-1-0.25 μm), respectively, in a fully automatic polishing device (Struers Tegramin-25). After these pretreatment processes, the polished cross-sections were coated with Au-Pt (Quorum SC7620—Mini Sputter Moater/ Glow Discharge System). The coated samples were examined by SEM-EDS (JEOL JSM-6060 LV equipped with IXRF EDS) analysis. After the preparation of glass-ceramic-coating samples, SEM (Jeol JSM-6060LV, Japan) analysis was performed to cross-section between the coatings and the steel substrate in the SEI mode and microstructure of the glass ceramic coatings were examined. The adhesion mechanism between glass-ceramic and steel substrate was investigated.

6.6.3 Impact Resistance Measurement

The impact resistance (adhesion ability) of glass ceramic coatings, enamels, is assessed in accordance with the BS EN ISO 10209:2013 standard.

As specified in the standard, the impact test involves subjecting the enamel surface to an energy of 15 kJ by dropping a 1,5 kg cylinder apparatus with a 22 mm diameter from a height of 75 cm onto the metal surface coated with enamel. The standard outlines the analysis of the impact on the enamel surface.

Following the impact, the resulting marks on the coatings are evaluated based on a scale ranging from 1 (indicating optimum adhesion) to 5 (indicating failed adhesion).

6.6.4 Acid Resistance Analysis

The acid resistance of glass ceramic coatings, enamels, is assessed in accordance with the ISO 28706-2 standard. For the acid resistance test, a solution is prepared with 10 g citric acid monohydrate and 100 mL distilled water 4 mL of the solution from the prepared solution is applied on the enamel surface and kept for 15 minutes on the enamel. The acid tested area is covered with a cap to prevent evaporation of the solution. When the time is completed, tthe designated region undergoes a thorough washing process, and acid resistance is determined according to the remaining trace. Following the trace, the resulting marks on the coatings are evaluated based on a scale ranging from AA (indicating optimum acid resistance) to D (indicating failed against from acids).

6.6.5 Coating Thickness

The thickness of glass ceramic coatings, namely enamels, is evaluated in compliance with the ISO 2178:2016 standard. To examine the uniform distribution of coating thickness, measurements are conducted using the DeFelsko Positest DFT Combo model coating thickness gauge. Measurements are acquired from three distinct areas, and the resulting average is recorded as the coating thickness.

6.6.6 Color Measurement

Color analysis is performed by measurement according to ISO 7724 guidelines. Measurements were taken using a spectrophotometer (Spectrophotometer CM-700d, Konica Minolta) in accordance with SCE D65 methods. Color values were calculated in terms of L*, a* and b*. The measured L value corresponds to whiteness and blackness, the measured a value corresponds to chromatic color from red to green and the measured b value corresponds to chromatic color from yellow to blue. The E calculation was used for color change comparison immediately after the measurement was taken. The delta E calculation is given in equation 6.1.

$$\Delta E^* = \sqrt{(L_2^* - L_1^*)^2 + (a_2^* - a_1^*)^2 + (b_2^* - b_1^*)^2} \quad (6.1)$$

6.6.7 Gloss Measurement

The assessment of gloss was conducted at five distinct locations using a TQC Sheen Polygloss gloss meter at a 60° angle. The results represent the average of these

measurements. A score of 0 signifies the highest level of opacity, while a score of 90 indicates the maximum glossiness of the coatings.

7
RESULTS AND DISCUSSION

7.1 COPR Characterization

XRF analysis was conducted to chemical contents the waste appropriate for use in glass-ceramic structures and to determine its heavy metal content. The XRF analysis revealed that the waste contains major components suitable for glass-ceramic structures. The predominant components in the supplied waste are MgO and SiO_2, while minor components include Fe_2O_3, C, and Cr_2O_3. Additionally, trace components such as CaO, NiO, and MnO were also identified. Components present in amounts less than 0.1 wt% were not included in the XRF results. These components, i.e. SO_3, Cl, CuO, Na_2O, are assumed to be impurities. In addition to the oxide components, the amount of carbon in the waste was also measured and is listed in table 7.1. Although the chemical composition of the COPR waste exhibits similarities to examples found in the literature, it also demonstrates differences[73]. These differences can be attributed to variations in the composition of mine wastes influenced by factors such as the geographical region, mining extraction methods, and enrichment processes [74]. The chemical composition results of the waste are presented in Table 7.1.

Table 7.1 Uncalcined waste chemical analysis results

Oxide	**wt.%**
MgO	36.33
SiO_2	32,85
Fe_2O_3	6,11
C	5,62
Cr_2O_3	2,28
Al_2O_3	0,5
CaO	0,33
NiO	0,34

Table 7.1 Uncalcined waste chemical analysis results (continued)

MnO	0,08
LOI*	15,56

Loss On Ignition was calculated by TG-DTA Analysis

Figure 7.1 demonstrates the thermal behaviors from TG and DTA perspectives**.** The first sudden mass loss started immediately with heating and continued up to approximately 200°C resulting in 2.52 wt.% mass loss. This reaction is thought to be an endothermic reaction in which the physically bound water is removed. When the heating operation was continued, the mass loss continued at different rates without stopping. There was a 3.27% reduction in the mass of the waste in the heating range of 200-450°C. The existence of various mass loss rates at different temperatures can be explained by the fact that the waste contains a wide variety of impurities that can become volatile. Most of the mass losses between 450 and 650°C can be explained by the removal of CO_2 from the structure. Moreover, the first dehydroxylation reactions start in this temperature range and reach the maximum level, which is one of the main causes of mass loss [75], [76]. The combustion reaction of C in the structure in the amorphous state took place and it became volatile and moved away from the structure. The presence of the exothermic reaction peak around 550°C can be explained by the burning of C obtained from the XRF results. (The reason for the endothermic reaction, which takes place at around 660°C without any change in mass, is the partially conversion of Lizardite 1T phase to Forsterite phase observed in XRD). Another endothermic reaction following this phase transformation is a decomposition reaction that takes place around 819°C. It is the thermal decomposition reaction of the structure containing the Lizardite 1T phase in the waste. There is also a decrease in the waste mass due to the thermal decomposition reaction at 819°C and the mass loss value equal to 3.04 wt.%. As a result of TG analysis, the total mass loss value was 15.56 wt.%. The reason for the exothermic reactions that take place after the mass loss has stopped might be also crystallization and polymorphic transformations at around 1100°C (protoenstatite and clinoenstatite). The phase transformation and thermal decomposition information in the literature support the analysis [77].

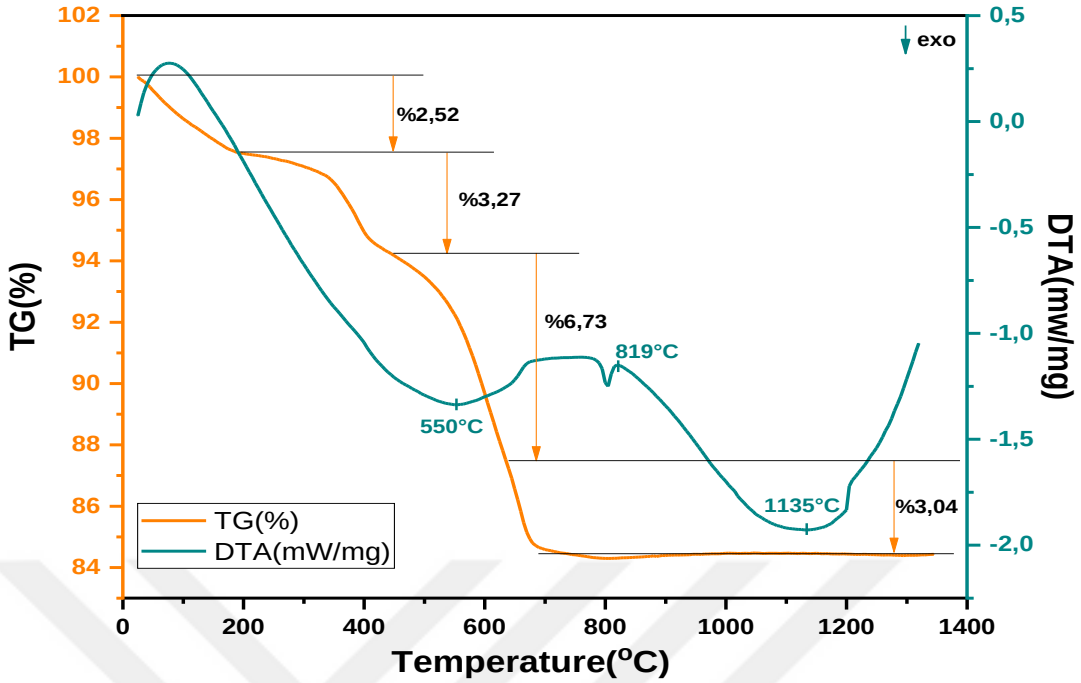


Figure 7.1 TG-DTA of COPR

7.2 Heat Treatment of COPR Samples

Heat treatment was applied to the waste to observe the results of heat effects. In order to increase the surface area and facilitate the contact of the heat, all the raw materials were laid on an alumina refractory and calcined for 1 hours. The samples were allowed to cool in the furnace once the process was completed. Calcination temperatures were determined by considering the critical temperature and mass loss points identified in TG-DTA analysis.

The drying process at 200°C was occurred based on the completion of the first mass loss observed at 198°C. Subsequently, calcination was conducted at 400°C to investigate alterations during the second phase of mass loss.

Temperatures of 500°C and 700°C were selected to observe changes in the structure corresponding to the exothermic reactions peaking at 550°C on the DTA curve. To explore modifications following endothermic reactions, samples calcined at 850°C and 1150°C were prepared.

Calcination parameters of heat-treated wastes, critical points in thermal analysis and sample codes are shown in Table 7.2 in detail.

Table 7.2 Sample identification derived from TG-DTA

Sample Code	Critical Points at TG-DTA	Calcination Temperature(°C)
D-200	First mass loss completed ≈198 at °C	200
C-400	Second mass loss between 200°C and 400°C	400
C-500	Before exothermic peak (550°C)	500
C-700	After exothermic peak (550°C)	700
C-850	After first endothermic peak (819°C)	850
C-1150	After second endothermic peak (1135°C)	1150

7.3 Heat Treated COPR Samples Characterization

The XRF result of sample D-200 is similar to the XRF result of the raw waste. It can be considered as dried and the moisture in its structure has been removed for measurement. Differences observed compared to the raw sample may stem from percentage composition changes inherent to it being a waste sample and the fact that it underwent drying at a higher temperature. Approximately 82% of the D-200 sample consists of major components.

Sample C-400 exhibits a major component percentage approximately 1 wt.% higher than that of sample D-200. The proportions of C, Cr_2O_3 and Al_2O_3 were in a decreasing trend, while Fe_2O_3 tended to increase.

Sample C-500 demonstrated results similar to sample C-400, with deviations of only about 0.2%. The percentage of C continues to decrease linearly. Upon analyzing the C-700 sample, a sudden decrease in the C percentage was observed, representing an approximate 2% change. This reduction can be attributed to CO_2 formation at 550°C, as explained in the TG-DTA analysis of the waste. The percentage fluctuation of components other than C followed a similar pattern, with the major components in the structure increasing to about 84%. In the remaining calcination samples, the percentage

of major components consistently remained above 83.5%, while the percentage of C decreased and the percentage of Fe_2O_3 increased.

Upon analyzing sample C-1150, it became evident that it had the most dominant percentage of MgO and SiO_2, with the percentage of C decreasing by about 4% compared to the dried sample D-200. Minor deviations of 0.1 - 0.2% were observed in other components. This variance in chemical composition may be attributed to the different calcination temperatures. Even if a sufficient decomposition temperature was reached for C, it might not have been able to completely evacuate the structure due to its form and insufficient calcination time. Heat treated samples chemical compositions are given in Table 7.3.

Table 7.3 Heat treated samples chemical compositions

Components/Sample Codes	**D-200**	**C-400**	**C-500**	**C-700**	**C-800**	**C-850**	**C-1150**
MgO	42.72	43.16	43.43	44.49	44.62	45.39	45.62
SiO_2	39.3	39.87	39.55	39.9	39.53	38.43	38.26
Fe_2O_3	7.24	7.7	7.85	8.1	8.43	8.88	9.43
C	6.46	5.6	5.1	3.2	3.01	2.92	2.49
Cr_2O_3	2.78	2.43	2.65	2.8	2.67	2.73	2.55
Al_2O_3	0.6	0.44	0.52	0.5	0.54	0.58	0.49
CaO	0.4	0.4	0.4	0.51	0.57	0.54	0.5
NiO	0.4	0.3	0.4	0.4	0.49	0.43	0.5
MnO	0.1	0.1	0.1	0.1	0.14	0.1	0.18

Values are given in weight percentage (wt.%)

XRD diffractograms are given in Figure 7.2. When the D-200 sample is examined; due to heat treatment at 200°C for 1 hour, it is usual that there is no physically bonded -OH group. D-200 sample contains amorphous and crystalline phases together. The major phases of the D-200 sample is the Chrysotile-2Mc1 (PDF#00-062-0393) and Lizardite1-T (PDF # 00-050-1625) phases. Chrysotile and Lizardite are the main minerals of the serpentine group and have similar chemical composition ($Mg_3Si_2(OH)_4$)[58], [78]–[80].

In addition, D200 sample has 2 minor phases, Brucite ($Mg(OH)_2$) and Hillebrandite ($Ca_2(SiO_3)(OH)_2$).

Figure 7.2 shows also XRD analysis results of the heat treated samples at different temperatures**.** Due to the crystal-bound water contained in the Chrysotile-2Mc1 an Lizardite 1-T phases, the peaks in the D-200 sample are more pronounced than those heat-treated at 400 and 500 degrees. The C-400 and C-500 phases have similar phases to the D-200 sample. Brucite phase is disappeared when the temperature is increased by an endothermic reaction.

Furthermore, C-500 has forsterite (Mg_2SiO_4) and Magnesiochromite ($Mg_{0.58}Cr_{1.52}Fe_{0.42}Al_{0.48}O_4$) phase formations.

In the literature, it has been determined that the formation of the lizardite phase towards anhydrous phase structures, that is, the formation of the forsterite phase, begins above 500°C [75].

Differently, the C-850 sample and other samples differ in terms of the phases they contain. According to the information confirmed from the TG-DTA analysis and the literature, the C-850 sample has forsterite phase instead of Lizardite1-T phase due to the phase transformation occurring around 819°C. The forsterite phase dominates the C-850 sample. As the minor phase, the magnesichromite (#PDF 04-007-9722) phase is observed.

Finally, sample C-1150 has both forsterite and Magnesiochromite phases similar to sample C-850 and a new phase, Enstatite ($MgSiO_3$) that is different. The formation of the enstatite phase occurs through a polymorphic transformation of the forsterite phase around 1100°C. Literature and TG-DTA analysis results of the waste support this phase formation [81].

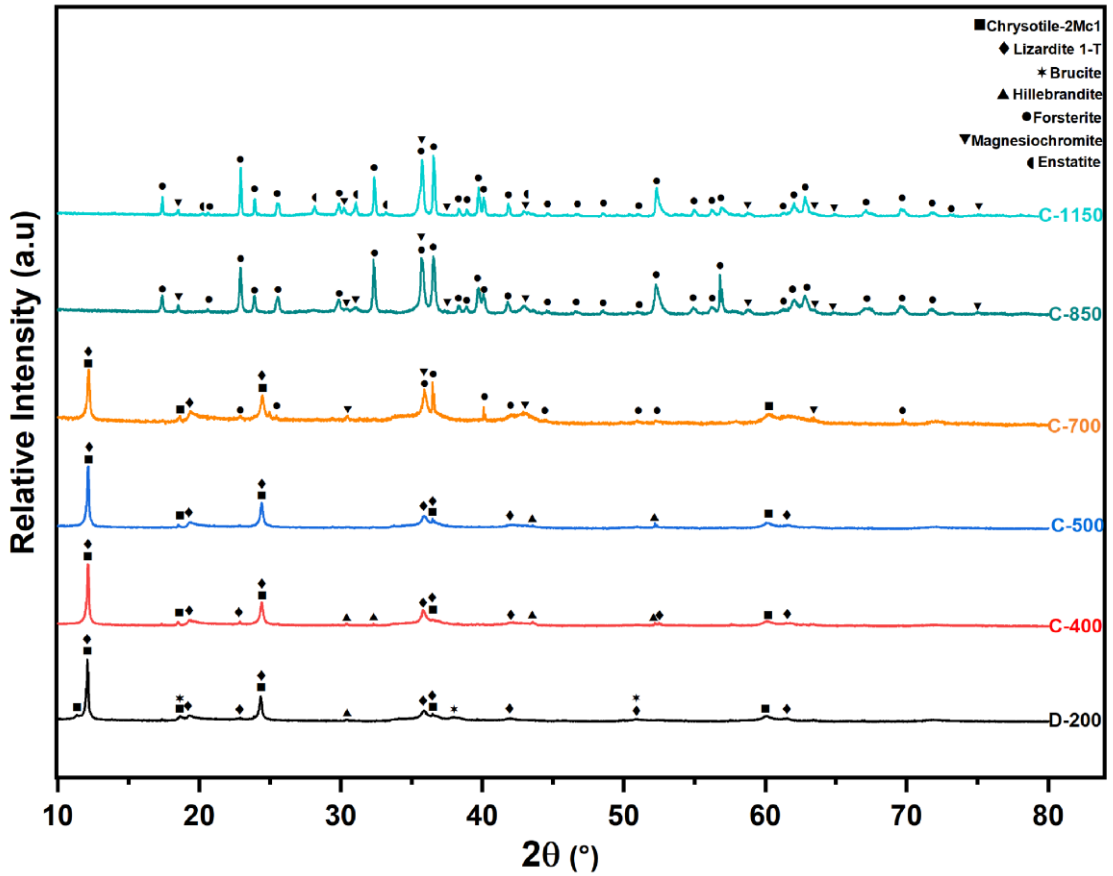


Figure 7.2 XRD analysis of COPR samples

When XRD analysis and TG-DTA analysis are evaluated together; it continues the dehydroxylation process of the phases of the waste with the effect of temperature and completes its transformation into the enstatite phase that does not contain OH groups and, it can be said that some structures in the amorphous phase crystallize by turning into a new magnesiochromite phase.

The ternary phase diagram of the phases in the serpentine group is also given in detail in Figure 7.3 [58]. In addition, the properties of the phases detected according to the XRD analysis results are also available in Table 7.4.

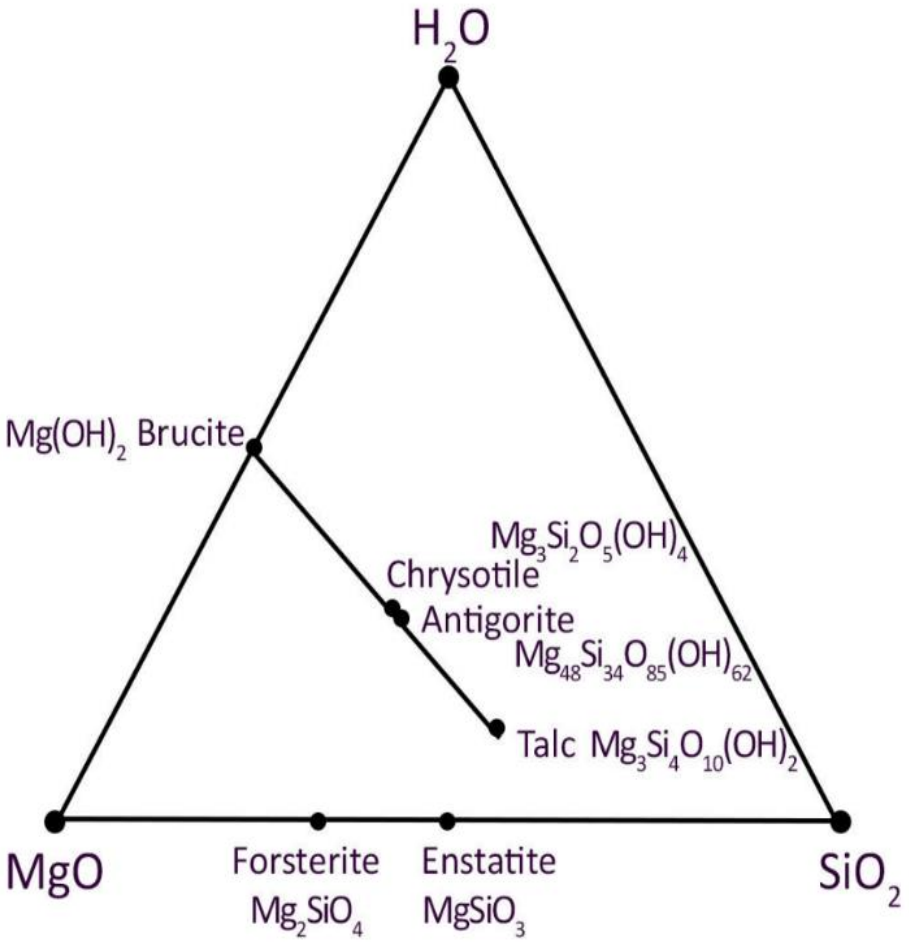


Figure 7.3 Ternary phase diagram of $MgO\text{-}SiO_2\text{-}H_2O$

The three oxides MgO, SiO_2 and H_2O make up 80–90 wt% of hydrated ultramafic rocks. Hydrous minerals stable in the $MgO\text{-}SiO_2\text{-}H_2O$ (MSH) system include the serpentine minerals (antigorite, lizardite, and chrysotile) and talc. Chemical formations have unique pressure and temperature ranges in which they are stable. Yet, These dehydration reactions release H_2O and depend strongly on temperature rather than Pressure. With increasing temperature, the low-T serpentine polymorphs lizardite and chrysotile breakdown to form antigorite serpentine at ~300°C. Antigorite dehydrates at~600°C–700°C and talc is stable to ~800°C on its own bulk composition [58], [82]–[84]

Table 7.4 COPR sample phases and their properties

Phases	Reference Number	Chemical Formula	Crystal System and Space Group	Molecular Weight (g/mol)	Atomic%
Chrysotile-2Mc1	PDF# 00-062-0393	Mg3Si2(OH)4	Hexagonal P31m(157)	277.11	H→22.22 Mg→16.6 O→50.0 Si→11.11
Lizardite 1T	PDF# 00-027-1276	Mg3Si2(OH)4	Monoclinic C2/m(12)	277.11	H→22.22 Mg→16.67 O→50.0 Si→11.11
Brucite	PDF# 00-044-1482	Mg(OH)2	Hexagonal P-3m1(164)	58.32	H→3.46 Mg→41.68 O→54.8

Table 7.4 COPR sample phases and their properties (continue)

Hillebrandite	PDF# 00-042-0538	$Ca_2(SiO_3)(OH)_2$	Orthorhombic Cc**(63E)	190.25	Ca→20.0 H→20.0 O→50.0 Si→10.0
Forsterite	PDF# 04-008-8545	Mg_2SiO_4	Orthorhombic Pbnm(62)	140.69	Mg→34.5 O→45.49 Si→19.96
Magnesio-chromite	PDF# 04-007-9722	$Mg_{0.58}Cr_{1.52}Fe_{0.42}Al_{0.48}O_4$	Cubic Fd-3m(227)	Cubic Fd-3m(227)	Al→6.69 Cr→40.84 Fe→12.12 Mg→7.28 O→33.07
Enstatite	PDF# 00-019-0768	$MgSiO_3$	Orthorhombic Pbca(61)	100.39	Mg→24.2 O→47.81 Si→27.98

To identify bonding types and stretching difference in the treated COPR, FTIR analysis were also shown in Figure 7.4 The existence of bands in the 3686 cm^{-1} in the structure for all samples apart from C-700, C-850 and C-1150 indicates that there are O–H bonds formed by water molecules and OH groups. This demonstrates that the structure of C-700, C-850 and C-1150 is free of moisture and crystal bonded water[85]. Peaks of between 900-1000 cm^{-1} represents the asymmetrical stretching vibration of Si-O-T (T = Si, Al), which indicates that Si-O and Al-O bonds are presence [12], [85]. Many studies have reported that spectral ranges of approximately 600 cm^{-1} and 650 cm^{-1} may be due to the presence of Mg. The peak at 612 cm^{-1} represents Mg-O bond when evaluated together with the results of literature and XRF analysis [86]–[88]. Bands at around 542 cm^{-1} and 426 cm^{-1} in all samples are attributed to Si-O and Al-O bonds, respectively. The structural vibrations and stretching are given in figure 7.4 [85], [89], [90].

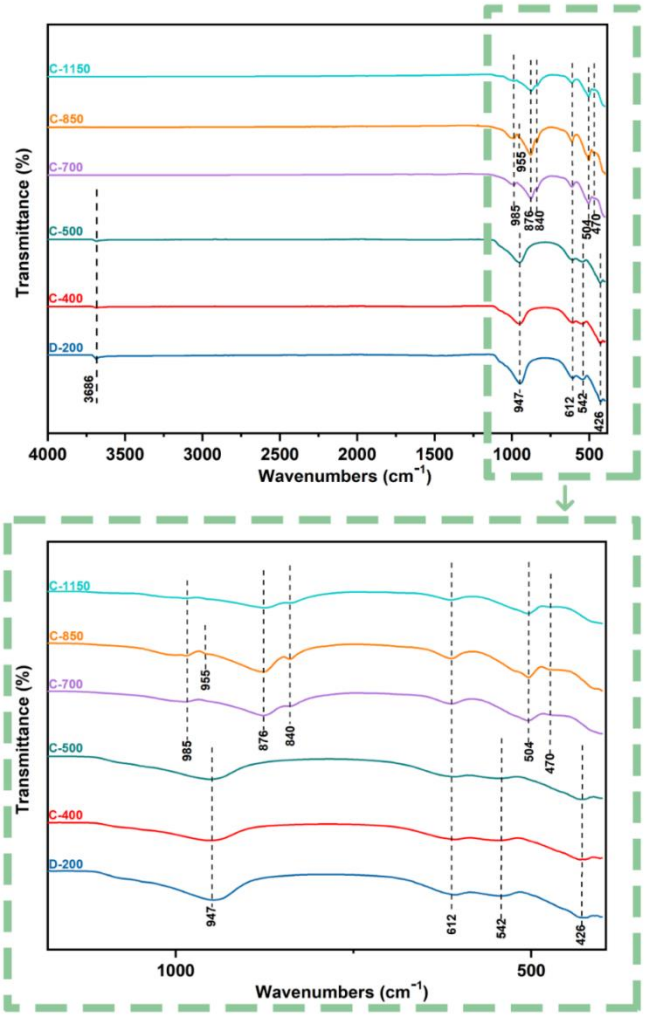


Figure 7.4 COPR samples FTIR analysis result

Raman and Fourier Transform Infrared (FTIR) spectroscopy are two complementary techniques used extensively for molecular characterization. While they have similarities, they operate on different principles and exhibit distinct strengths and limitations, making each suitable for specific applications.FTIR spectroscopy is particularly sensitive to polar functional groups like O-H, N-H, and C=O bonds. On the other hand, Raman spectroscopy is more sensitive to non-polar bonds such as C=C and C≡C, especially in carbon-based materials like graphene and carbon nanotubes. It also excels in detecting symmetrical vibrations.Combining both techniques enables a more comprehensive analysis of molecular vibrations in a sample. This combined approach was utilized to thoroughly analyze waste materials and monitor changes induced by temperature variations [91]–[93]. Figure 7.5 shows the Raman spectrum obtained samples from COPR. The Raman signal was acquired for approximately 10 s in three acquisition cycles by setting the laser output power at the sample surface to 250 mW. The low frequency range of the Raman spectrum obtained in the D-200 sample is characterized by three bands. These three bands are located at 231 cm^{-1}, 340 cm^{-1}, and 377 cm^{-1} and represent the vibrations of O-H-O groups, bending of SiO_4, and symmetric Mg-OH vibration, respectively [94], [95]. The other characteristic peak at 450 cm^{-1} belongs to T-O-T (T=Si or Al) vibrations [60], [96]. The minor vibration at 520 cm^{-1} indicates the presence of Si-Si [97]–[99].

There are also three bands in D-200 with peaks at 620 cm^{-1}, 690 cm^{-1} and 1090 cm^{-1}. These bands represent OH–Mg–OH, Si-O-Si (690 cm^{-1}) and Si-O-Ca (1090 cm^{-1}) bonds. Four main peaks (about 230 cm^{-1}, 390 cm^{-1}, 690 cm^{-1}, and 1100 cm^{-1}) also characterize the spectrum of lizardite. The presence of these peaks coincides with our XRD analysis results and confirms the existence of the Lizardite 1-T phase [94], [96].

C-400 sample has vibration points just like D-200. Only the intensities of these peaks decreased. The frequency of all Raman OH vibration modes decreases linearly with temperature. Unlike the D-200 sample, new peaks started to become evident at 840cm^{-1} and 860cm^{-1}. These vibrations can be attributed to Si-O stretching. C-500 contains both the same and different vibrations. New peaks are seen more intensely at 840 cm^{-1} and 860cm^{-1}. This can be explained by the fact that, as in the D-200 and C-400 samples, it contains the Lizardite 1-T phase in its structure, but also the Forsterite phase. Unlike the D-200 and C-400 samples, it contains 820 cm^{-1} and 860 cm^{-1} vibrations. These vibrations can be attributed to Si-O stretching. The reason for this new Si-O stretching may be the

formation of forsterite phase. Additionally, the observation of tetrahedral SiO_4 in the forsterite phase can be explained by the fact that Mg atoms are in the center. The C-850 sample, on the other hand, has a Si-O stress caused by the presence of the forsterite phase at 820 cm^{-1} and 860 cm^{-1}. XRD results of the samples and literature samples confirm the Raman analysis [76], [95].

Another peak occurring in the C-500 sample is located at 911 cm^{-1}. This peak is associated with the presence of $(Si_3O_9)^{-6}$ ion in the structure in the literature [75].

Three new characteristic peaks were observed in the C-700, C-850 and C-1150 samples, except for regions similar to other samples. These peaks; it is located at 295 cm^{-1}, 325 cm^{-1} and 911 cm^{-1}. While 295 cm^{-1} and 325 cm^{-1} represent SiO_4 bending, the peak located at 911 cm^{-1} is attributed to the presence of $(SiO_7)^{-6}$ ion. When the peak at 690 cm^{-1} is interpreted together with the XRD analysis, lizardite has disappeared from the environment, but the peak due to the ferrian chromite structure continues to exist and these two peaks overlap [75], [94], [96].

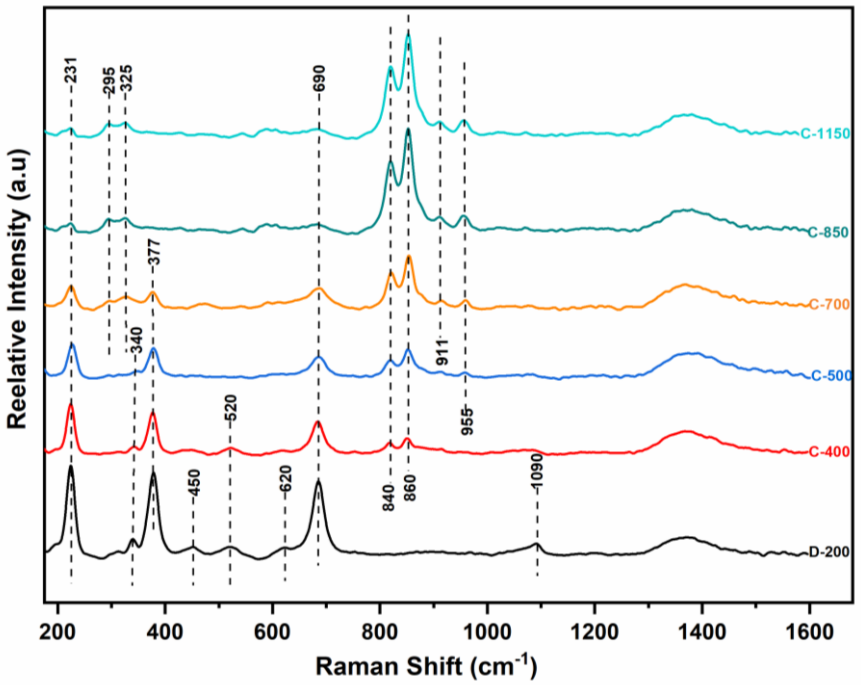


Figure 7.5 COPR samples Raman analysis result

To analyze the thermal behavior of the prepared sample, geometric changes, such as the height and width at various temperatures, were assessed according to the DIN 51730 standard. Heating microscope analysis provided five typical temperatures. The greatest shrinkage, when rounded edges appear, and the initial shrinkage with a 5% change in size are referred to as sintering ($T_{Sintering}$) and softening ($T_{Softening}$), respectively, as illustrated

in Figure 7.6. The sample's corners become perfectly round, and the spherical point where the first hint of melting emerges is known as the sphere temperature (T_{Sphere}). The half-sphere temperature ($T_{Half\ Sphere}$) is found at the semi-spherical position where the sample height is equal to half the base width. The melting temperature ($T_{Melting}$) is defined as the flow point at which the sample melts and shrinks to a third of its original height in the hemispheric condition [100], [101].

Figures 7.6 demonstrate the characteristic temperatures, $T_{Sintering}$, of each COPR. The sintering temperatures of the COPR $T_{Sintering}$ were determined as 895°C respectively.

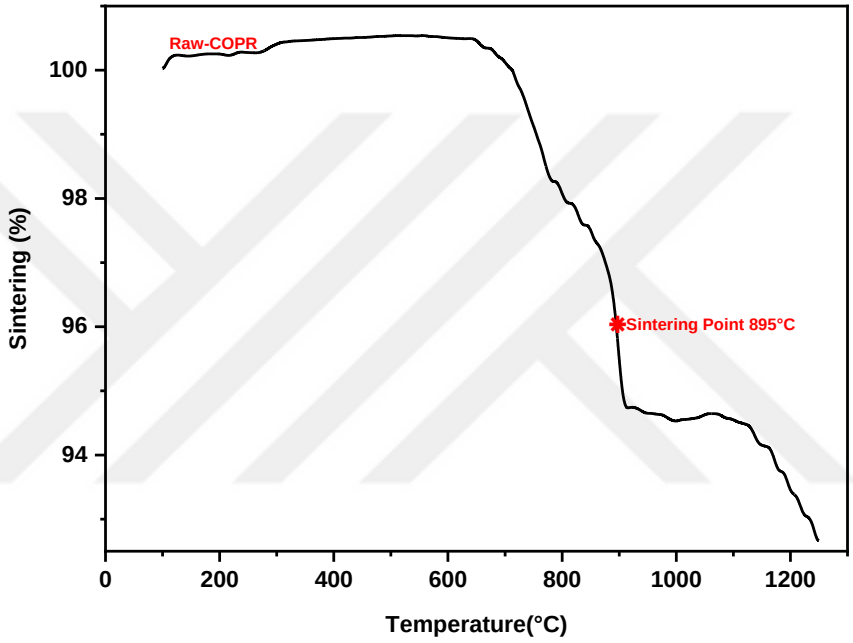


Figure 7.6 COPR samples hot stage microscopy analysis result

Specific surface area (SSA) and pore volumes (PV) are given in Table 7.5. When calcination temperatures, specific surface area and pore volume are evaluated together; as the temperature increases, there is a linear increase in SSA and PV for D-200, C-400, C-500, C-700 and C-850 samples. The reason for this can be explained by the loss of moisture and carbon in the structure over time. Elemental analysis results also confirm this information. Differently, there was a sharp decrease in SSA and PV values in the C-1150 sample. The reason for this can be explained by the transformation of the structure into a more dense form. Heat microscope analysis of waste; this explains the sudden decline. The waste showed sintering properties by losing 5% of its structural volume around 895°C (higher than the calcination temperature of the C-850 sample) [102].

Table 7.5 BET analysis result of samples

Sample Code	Specific Surface Area (m^2/g)	Pore Volume (cc/g)
D-200	3.44	0.004
C-400	10.76	0.012
C-500	11.99	0.013
C-700	27.81	0.041
C-850	28.76	0.051
C-1150	0.623	0.003

SEM images of heat treated COPR samples are shown in Figure 7.7. Images were captured with BSE mode; obtained at 250 times magnification. Analysis results show particle size samples subjected to heat treatment. As the heat treatment temperature increased (from D-200 to C-1150), no major change was observed in the particle, and it preserved its structure. However, as the temperature increased, cracks and fissures appeared in the structure as shown yellow arrows. The reason for this can be explained by the carbon burning in the structure becoming volatilized with rising temperature and leaving the structure by escaping from some areas. The departure from this structure observed by SEM analysis can also be clearly observed according to the elemental analysis results.

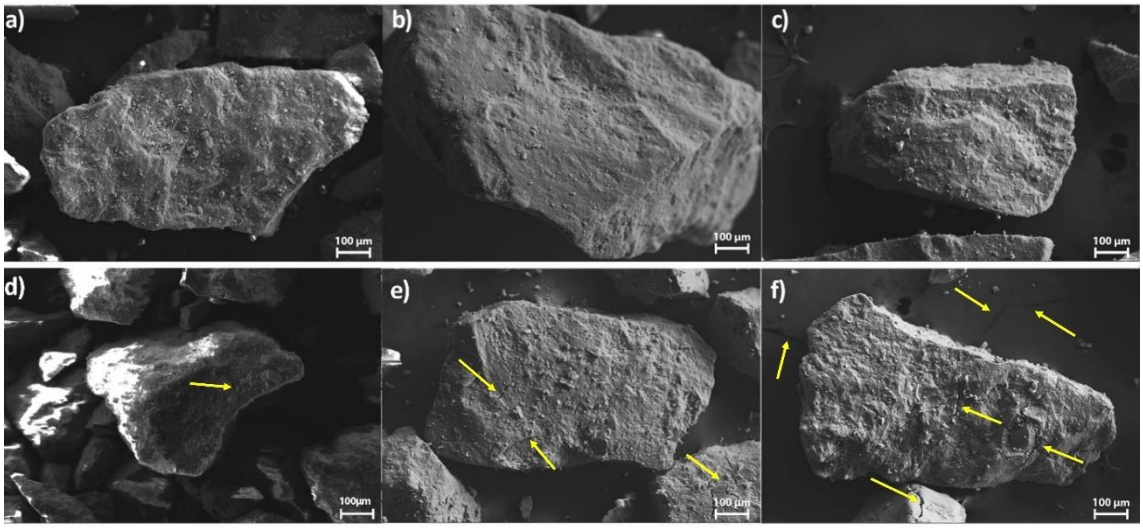


Figure 7.7 SEM analysis result of heat treated COPR samples

Additionally, Figure 7.8 includes samples; EDS analysis results are included. The SEM images of the sample obtained with closer magnifications in the left column of the figure were elementally mapped using EDS; The mapping of the relevant SEM image is included in the right column. Carbon removal from the structure, which is also clearly observed at smaller magnification scales; It was clearly observed in EDS mapping, and with the removal of carbon, the concentrations of magnesium and silicon, which are the major components, in the structure increased. The amount of carbon in the structure; it decreased from 8.50 wt.% to 1.69 wt.%. With this decrease, magnesium and silicon concentrations increased from 24.69 wt.% and 16.11 wt.% to 33.55 wt.%, 24.04 wt.%. The reason for the numerical differences in these results, which are similar to elemental analysis in terms of decrease and increase behavior, can be explained by the fact that measurements were taken from a local area within the sample with the EDS mapping method.

Mg and Si concentration increase are not only due carbon losses by burning but also evaporation reactions of physical and chemically bonded water molecules and OH groups during calcination and sintering % heat treatment of COPR.

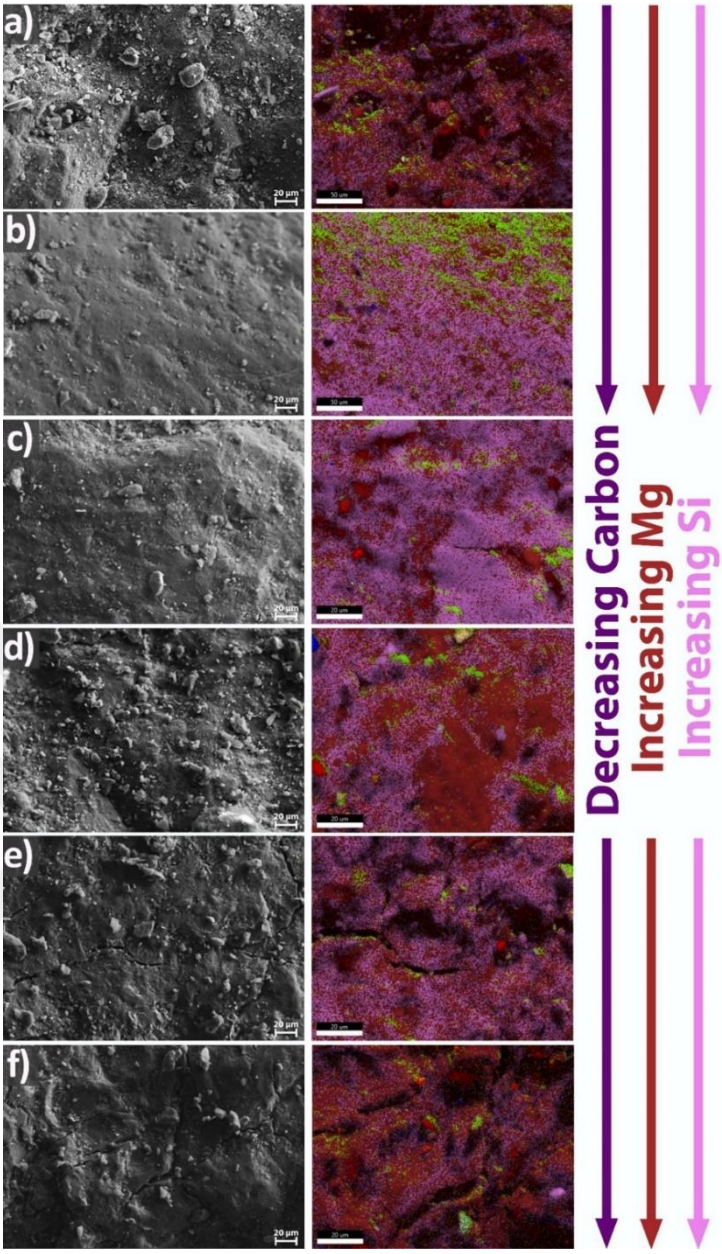


Figure 7.8 SEM-EDS analysis result of heat treated COPR samples

7.4 PG Characterization

The COPR sample, whose behavior in the blend was previously investigated, was added untreated and the WD-batches started to be heated. The chemical compositions of PG-STD-Ni, PG-WD-Ni, PG-STD-Co, and PG-WD-Co frits are provided in Table 7.6. XRF and AAS analyses were employed to determine the chemical contents. A typical sodium borosilicate glass system was synthesized, and functionalizing oxides were incorporated into the composition, taking into account the coating's final properties.

Table 7.6 Chemical compositions of precursor glasses

		PG-STD-Ni	PG-WD-Ni	PG-STD-Co	PG-WD-Co
	SiO_2	53.92	54.03	53,26	53.93
	MgO	3.55	3.57	3.57	3.56
R_2O	Na_2O K_2O Li_2O	11.11	11.01	11.0	10.94
RO	CaO BaO NiO CoO MnO	12.35	12.1	11.9	12.39
R_2O_3	B_2O_3 Fe_2O_3 Al_2O_3 Sb_2O_3 Cr_2O_3	14.94	15.23	15.76	14.74
RO_2	TiO_2 ZrO_2	2.71	2.59	2.54	2.66
R	F	1.42	1.47	1.97	1.78

PG-WD glass systems, produced using approximately 3.5 wt.% COPR, exhibit similar chemical compositions to PG-STD glass systems produced entirely from commercial raw materials. The deviation rate between the compositions is within the range of ±0-0.2%. This sensitivity in the deviation rate reveals the similarity of the chemical compositions of waste-derived glass systems combined with industrial raw materials and COPR and

standard glass systems produced entirely using industrial raw materials. This indicated that COPR could be a suitable raw material source for SiO_2 and MgO for a sustainable production approach in glass ceramic coating. COPR has become an alternative raw material to industrial raw materials.

The XRD patterns of the precursor glass structures, obtained by melting and quenching the batches mixture, are presented in the Figure 7.9. The diffractograms are generated range from 2θ:10° to 2θ:80°. XRD results of all precursor glass structures are similar; 2θ:15° to 35° has a broad peak. This peak indicates the amorphous structure typical of silicate glass. No characteristic peaks were identified in the patterns, affirming that all glass precursors possess an amorphous structure and that the melting/quenching processes were successful[103], [104]. XRD analysis results of precursor glasses are given in Figure 7.9.

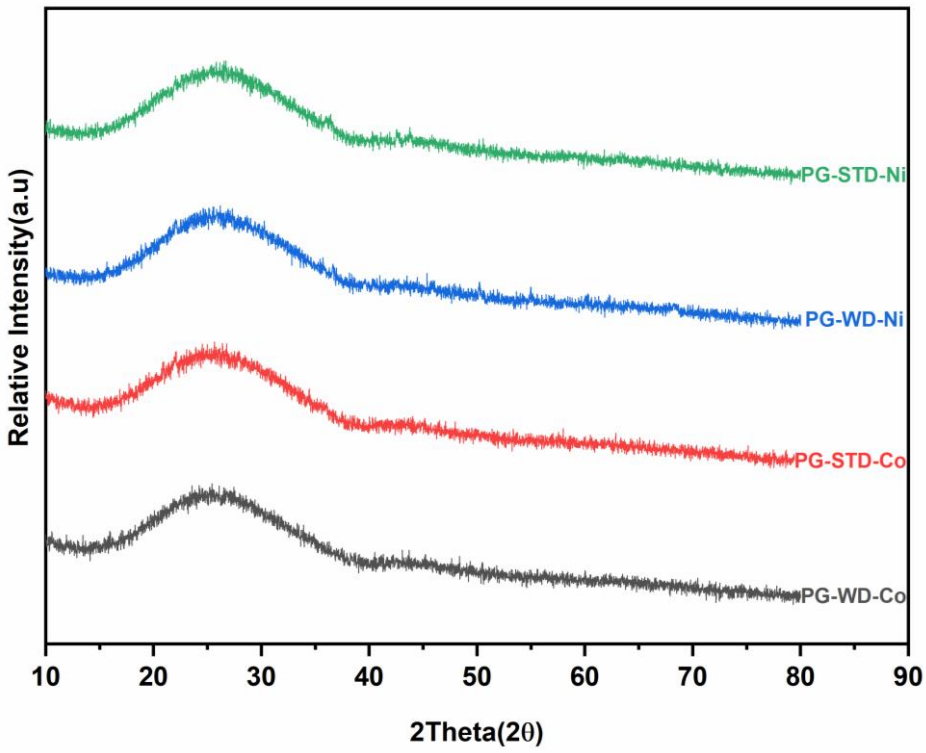


Figure 7.9 XRD analysis results of precursor glasses

X-ray Photoelectron Spectroscopy (XPS) analysis was conducted to determine the valence states of the components within the structures. The D-200 and C-1150 samples were selected to investigate the initial state of the waste and the effects of calcination on chromium valence. Upon examining the element distributions of the samples, it is evident that the XPS analysis results are consistent with the XRF and XRD analyses.

The base line data for chromium (Cr) obtained through deconvolution indicate that the D-200 sample contains Cr^{6+} at 579.1 eV. With an increase in temperature, some of the Cr^{6+} transitions to Cr^{3+} at 576.4 eV. The element distribution data for the D-200 and C-1150 samples are presented in Figure 7.10, and the valence states and binding energies of the Cr element are summarized in Table 7.7.

Upon examining PG-WD samples, it was observed that the PG-WD-Ni sample displayed partial success to the C-1150 sample, with both Cr+6 and Cr+3 valences present. Initially, all Cr in the waste was in the Cr^{+6} state prior to vitrification. For the PG-WD-Co sample, all Cr^{+6} was completely reduced to the Cr^{+3} form. Magnesium (Mg) plays a crucial role in facilitating this reduction, as it tends to form $MgCr_2O_4$ at high temperatures, thus reducing Cr^{+6} to Cr^{+3} [10], [105]–[108]. The variance in Cr^{+6} between PG-WD-Ni and PG-WD-Co samples is due to the higher oxygen affinity and reducing capabilities of CoO compared to NiO, as depicted in the Ellingham diagram [52]. The element distribution data for D-200, C-1150, and PG-WD samples are provided in Figure 7.10 and the valence and binding energies of Cr are detailed in Table 7.7.

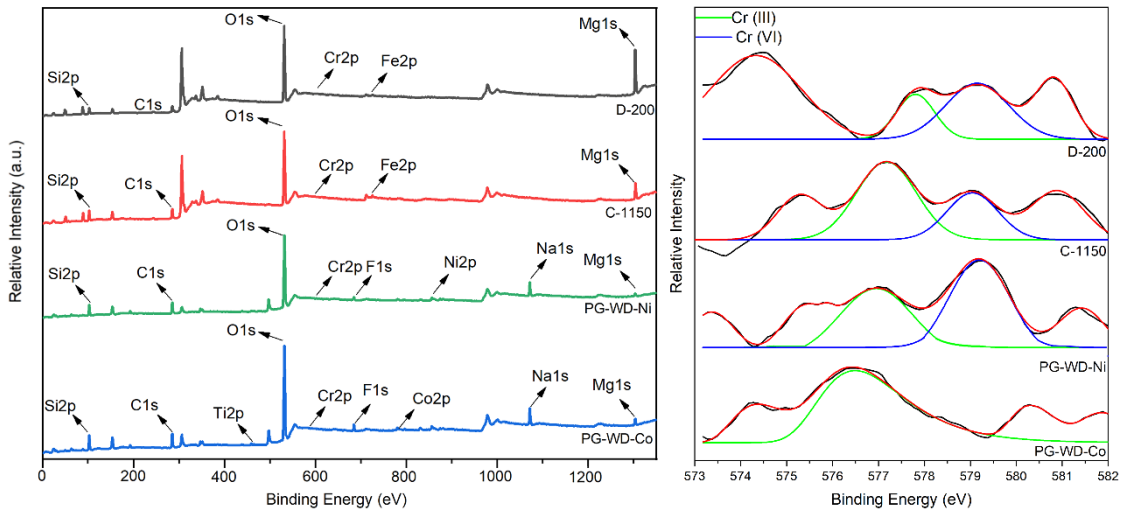


Figure 7.10 . a) X-ray photoelectron spectroscopy (XPS) survey spectra b) high-resolution XPS spectra of Cr2p of D-200, C-1150 and GCC-WD sample

Table 7.7 Cr2p peak positions and areas for D-200, C-1150 and PG-WD samples

Samples	Parameters	Cr^{3+}	Cr^{6+}
D-200	Peak position (eV)	576.4	579,1
	%Peak area	-	100
C-1150	Peak position (eV)	576,4	579,1
	%Peak area	66,4	33,6
PG-WD-Ni	Peak position (eV)	576,4	579,1
	%Peak area	45,5	54,5
PG-WD-Co	Peak position (eV)	576,4	579,1
	%Peak area	100	-

TG-DTA analysis of PGs is given in Figure 7.11. The figure can be dived two main parts for clear explanation. First main part is mass loss with analyzed TG analysis. All PGs have similar characteristic patterns. A total mass loss 0.66 wt.%, 0.69 wt.%, 0.82 wt.% and 0.91 wt.% for PG-STD-Ni, PG-WD-Ni, PG-STD-Co and PG-WD-Co respectively. This loss is expected in sodium boro-silicate glasses, which is defined as thirsty glass, and is caused by the moisture absorbed by the glass from the atmosphere[109], [110].Furthermore, thirsty glasses, PGs, contains fluorine. With the temperature, some of the fluorine in the glass structure has moved away from the gaseous structure.

The other main issue is the interpretation of DTA analysis. For this interpretation it is necessary to divide the curves into areas of endothermic and exothermic behavior. When we look at endothermic areas; the presence of TG can be mentioned for the formation of the first endothermic peak. When nickel-derived and cobalt-derived glasses are compared among themselves; the glass transition temperatures are quite close to each other: 515°C, 518°C, 513°C and 511°C for PG-STD-Ni, PG-WD-Ni, PG-STD-Co and PG-WD-Co, respectively. When these temperatures were measured by dilatometry analysis, different results were obtained. The reason for this can be explained as the measurement sensitivity

of the two devices and their sample preparation methods. The dilatometry sample is prepared by previously subjecting it to heat treatment.

When both analyzes are compared, it is seen that the raw material change does not affect the glass transition temperature.

A broad exothermic peak in the range of 600-700°C was observed for all four PGs. The formation of this large exothermic structure can be attributed to calcium silicate crystallization [111].

From the broad exothermic peak, the endothermic peak located later, around 721-730°C, can be attributed to nucleation for the formation of a new phase [112].

The exothermic peak observed around 820°C is it is the transformation of amorphous silica structure into cristobalite [113].

The endothermic peak observed at 860-870°C, when compared to the literature, is the tridymite transformation of the quartz in the structure before the cristobalite transformation [81]. All glass structures; have similar characteristic points and reaction tendencies. The temperature differences that exist between them can be explained by chemical composition differences.

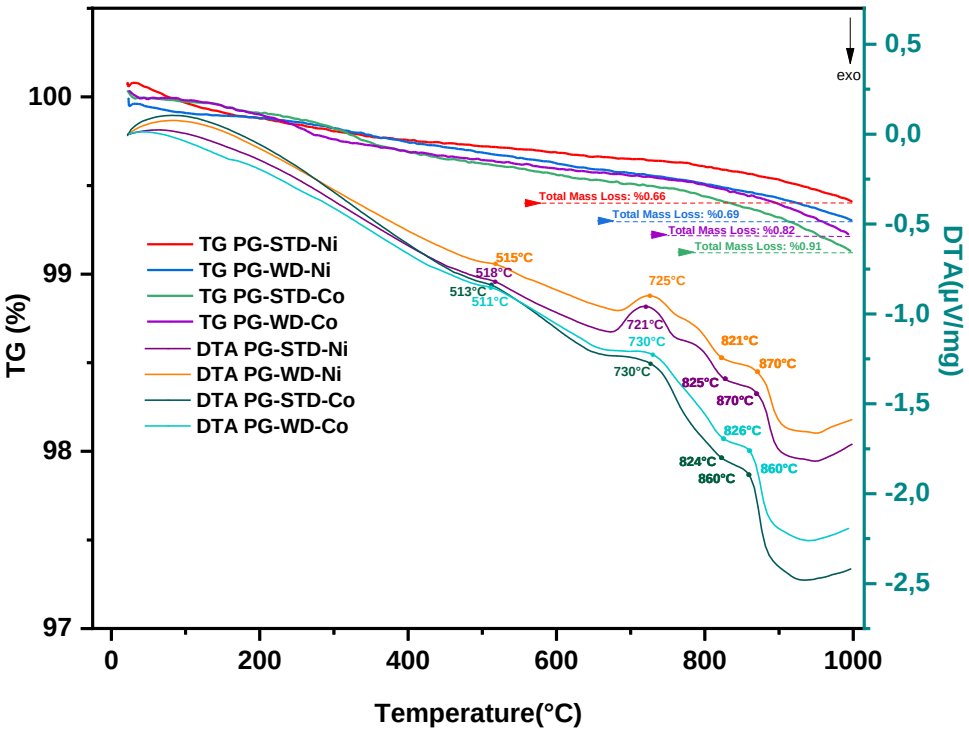


Figure 7.11 TG-DTA analysis results of precursor glasses

Sintering point decrease due to temperature of precursor glasses; the temperature points are explained in Table 7.8. The sintering temperatures of the precursor glasses $T_{Sintering}$ were determined as 747°C, 750°C, 731°C and 729°C, respectively. There is negligible difference between PG-STD and PG-WD samples. (2-3°C) The sintering temperature of PG-WD-Ni is the highest value; it can be explained by the fact that the highest refractory component amount is present in PG [114].

Due to the low viscosity of the glass structure, which causes the surface of the samples to get wet, softening temperatures in this study were determined by observing the rounded edges of the samples. Softening values were observed as 867°C, 861°C, 847°C and 859°C, respectively. These differences in softening values are around 10% °C. This change, $T_{Sintering}$ and $T_{Softening}$ temperatures, is of great importance in determining the bubble size of the coating after the devitrification process.

Additionally, upon reaching the T_{Sphere}, the effect of flux oxides on the heating behavior of the precursor glass chemical composition was observed more clearly. Fluxes play a key role in reaching the melting point from this temperature [75]. T_{Sphere} is displayed at points where the shapes turn into spherical forms and the height is equal to the diameter. T_{Sphere} values were determined as 906°C, 902°C, 865°C and 878°C respectively. Nickel-derived glasses showed very similar results (°4C). Hydrostatic pressure, associated with the density of the liquid phase, tries to flatten the shape, while surface tension tries to minimize the surface, making it spherical. If the height of the sample is equal to half the width of the base, the sample reaches the $T_{Half\ Sphere}$.

$T_{Half\ Sphere}$ values were recorded as 927°C, 926°C, 875°C and 888°C, respectively. Finally, when the height of the sample reaches one-third of the base, it becomes clear that melting has begun. 939°C, 938°C, 886°C and 902°C were used as the melting values of the samples.

Nickel-derived glass structures successively revealed $T_{Half\ Sphere}$ and $T_{Melting}$ values with a difference of 1°C. In cobalt-derived glass structures, $T_{Half\ Sphere}$ and $T_{Melting}$ values were determined with similar temperature differences (12-15°C). This can be explained by the fact that the detection sensitivity may vary due to the optical measurement of the device.

Table 7.8 Characteristic thermal point results of precursor glasses from HSM analysis

	 Sintering Point	 Softening Point	 Sphere Point	 Half Sphere Point	 Melting Point
PG-STD-Ni	747°C	867°C	906°C	927°C	939°C
PG-WD-Ni	750°C	861°C	902°C	926°C	938°C
PG-STD-Co	731°C	847°C	865°C	875°C	886°C
PG-WD-Co	729°C	859°C	878°C	888°C	902°C

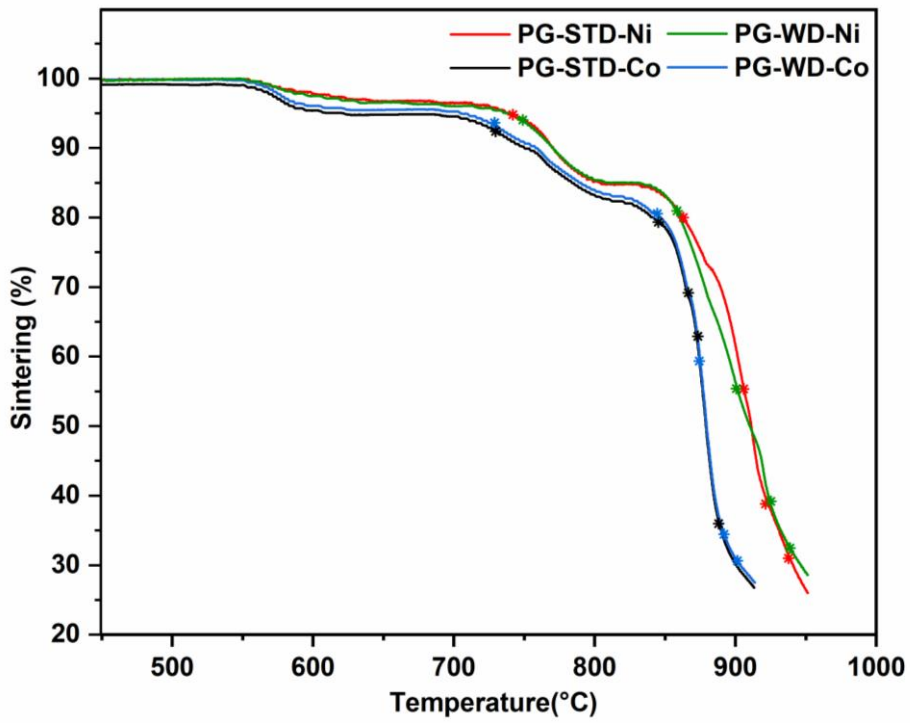


Figure 7.12 HSM analysis results of precursor glasses

When the temperature rises above the softening point ($T_{Softening}$), the viscosity continues to decrease, and the glass-ceramic system behaves like a high-density liquid clearly seen at Figure 7.12. It is assumed that the decreasing viscosity of the coating system accelerates the metal substrate, increasing its wettability. Due to the formation of dendritic structures on the metal substrate, its surface area has increased and due to the decrease in viscosity, it can be wetted more easily during the application of the adhesion mechanism. As a result, the glass-ceramic coating and the metal substrate interact chemically more quickly

and intensively during the adhesion mechanism. This leads to better surface properties and adhesion properties between the metal substrate and the glass-ceramic coating [21], [110] Therefore, ensuring excellent adhesion between the substrate and glass-ceramic coatings; The heat treatment temperature was chosen as 860°C in order to examine the coating performance of glass structures at similar temperatures.

Certain changes occur when a material is heated. One of these changes can be termed thermal expansion, observed through the elongation or volumetric increase in the body. Thermal expansion is crucial data for material interoperability and is numerically defined as the coefficient of linear thermal expansion (COE), representing the percentage increase in the length of a material sample as the temperature rises by one degree. The coefficient of linear thermal expansion (COE) "α" is calculated using the equation provided below.

$$\alpha = (1/1)\, x\, (\Delta l/\Delta t) \tag{7.1}$$

Additionally, beyond linear, two-dimensional thermal expansion, three-dimensional volumetric thermal expansion is used to describe the change in object volume when heated up to 1°C and is expressed as "β." For isotropic amorphous structures, where properties do not vary depending on direction, the volumetric COE can be adequately described by the following equation [45].

$$\beta = 3\alpha \tag{7.2}$$

The thermal expansion behavior of the precursor glass, or frit, is one of the factors that determine how well a glass-ceramic coating adheres to a steel substrate. One of the most critical elements in producing a glass-ceramic coating without errors is ensuring that the coefficients of thermal expansion (COEs) of the steel substrate and frits are very close to each other [115], [116]

Tension-causing fissures in the structure become apparent when the tensile strength of the glass-ceramic coating is exceeded. On the other hand, if the metal substrate's coefficient of expansion (COE) is significantly lower than that of the glass-ceramic, only chipping flaws emerge due to the stronger compressive strength of the glass-ceramic coating. Since it is widely recognized that compressive strength is more detrimental than tensile strength, the COE of glass-ceramic coatings is always kept lower than that of metal substrates [45], [115].

To determine thermal expansion coefficients; PG-STD-Ni, PG-WD-Ni and PG-STD-Co, PG-WD-Co were heated up to 550°C, starting from room temperature. α values were measured at 2 different points: 30°- 300°C and 30°- 400°C.

In Figure 7.13, these values are given for PGs containing nickel-derived adhesion agent in figure a, and for PGs containing cobalt derivative adhesion agent in figure b.

It is 9.97x10^{-6}/K, 9.88x10^{-6}/K for PG-STD-Ni and PG-WD-Ni at 300°C, respectively; it was observed that at 400°C it was 10.40x10^{-6}/K and 10.15x10^{-6}/K, respectively. For PG-STD-Co and PG-WD-Co, it is 9.93x10^{-6}/K, 9.73.10^{-6}/K, respectively, at 300°C; it was observed that at 400°C it was 10.30x10^{-6}/K and 10.21x10^{-6}/K, respectively

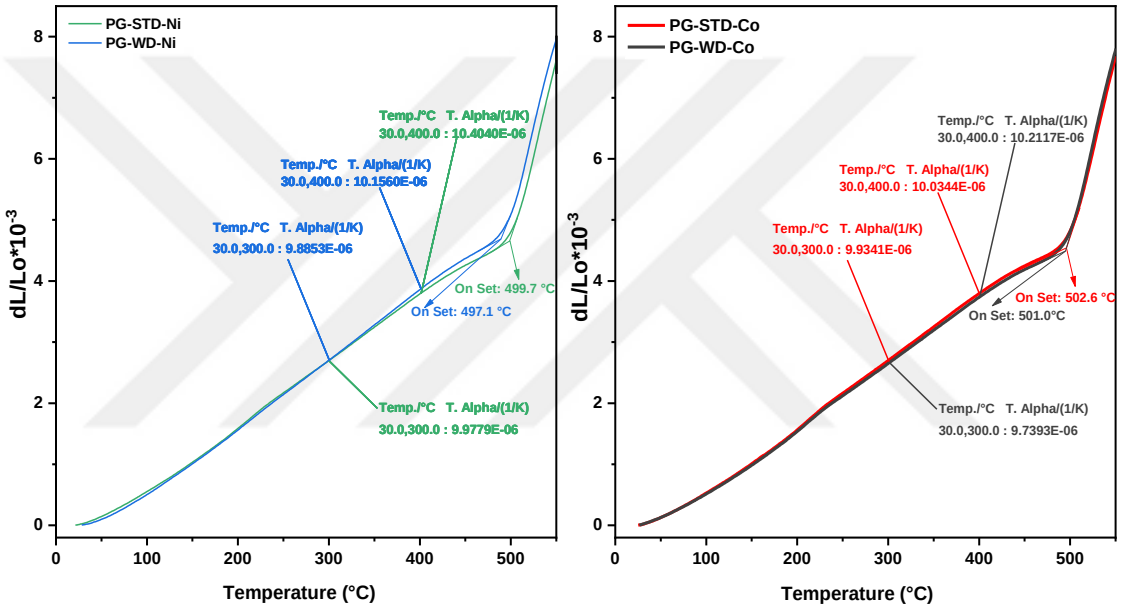


Figure 7.13 Dilatometer analysis results of precursor glasses a) PGs containing nickel-derived adhesion agent, b) PGs containing cobalt derivative adhesion agent

These changes in the expansion coefficient results may vary depending on the presence of R_2O components in the chemical composition, sample preparation method and device sensitivity. The situation PG-STD-Ni > PG-WD-Ni and PG-STD-Co > PG-WD-Co in the coefficient of thermal expansion can be explained by non-bridging oxygen ions.

The thermal expansion coefficient of glass is influenced by the asymmetry of the amplitude of thermal vibrations within the glass structure. When the glass network contains numerous strong bonds, the amplitudes of thermal vibrations are small, resulting in a decrease in the thermal expansion coefficient as the rigidity of the glass network increases. Modifying cations contribute to a reduction in the rigidity of the glass network

by introducing non-bridging oxygen ions, consequently increasing the thermal expansion coefficient of the glass. The alteration in the thermal expansion coefficient caused by various additives is often directly proportional to the quantity of the additive [117].

The cubic thermal expansion coefficient of glass-ceramic coating samples was calculated using eq. 7.2 result of calculations; For cubic thermal expansion coefficients, the order can be made: PG-STD-Ni > PG-STD-Co > PG-WD-Ni > PG-WD-Co. Numerically, this ranking is; 299($1/10^{-7}$°C) > 298($1/10^{-7}$°C) > 296($1/10^{-7}$°C) > 292($1/10^{-7}$°C). The cubic expansion coefficients of glass structures are lower than the cubic expansion coefficient of low carbon steel (465.$1/10^{-7}$°C) and the presence of adhesion agents that can cause chemical bonding with steel; it reveals that the steel base can be covered with these glass structures [45], [115]

In this analysis, both the glass transition temperature and expansion coefficients were measured. It is well-documented in the literature that for supercooled liquids, the glass transition temperature expressed in absolute degrees is approximately two-thirds of the melting point (T_M), represented as $T_G / T_M = 2/3$ [118]. As seen in the Figure 7.13, the T_G temperature of PG-STD-Ni, PG-WD-Ni and PG-STD-Co, PG-WD-Co samples are 499.7°C, 497.1°C and 502.6°C, 501°C, respectively. In this analysis, which confirmed that the characteristic temperatures of the samples seen in the TG-DTA analysis were similar, it was seen that the Tg changed by only 1.5°C and was negligible; it has been determined that PG-STD glass structures have higher Tg values.

7.5 GCC Characterization

7.5.1 Phase Analysis

Figure 7.14 shows the X-Ray Diffraction spectra of glass ceramics. According to the results observed from the diffractograms, amorphous and crystalline phases coexist. During crystallization, instead of the entire amorphous phase crystallizing; The resulting crystal was dispersed embedded in the amorphous phase. The broad band around 2θ:15°-40° in the XRD patterns revealed that GCC-STD-Ni, GCC-WD-Ni, GCC-STD-Co and GCC-WD-Co had amorphous network. Five different crystalline phases were detected in a typical sodium borosilicate glass system. These phases; fluoro-tremolite with $Ca_2Mg_5(Si_4O_{11})_2F_2$ formulation (PDF#00-009-0330), quartz with SiO_2 formulation (PDF#00-022-1161) and cristobalite (PDF#82-0512), $Ca_2Fe_2O_5$ (PDF#01-086). Calcium

iron oxide with the formulation and sodium calcium silicate crystals with the formulation $Na_4CaSi_3O_9$. For all four glass-ceramic structures; even though the peak intensities changed, there was no difference between the crystals formed. With these glass-ceramic structures synthesized from different adhesion agents; it can be said that there is no direct relationship with adhesion agents-crystal formation. As a major component, it can be viewed from three crystals. Fluoro-tremolite, quartz and cristobalite. Along with these crystals, minor calcium silicate and calcium iron oxide structures were observed.

Although the crystalline phases had the same peaks, there were differences in peak intensities between nickel-derived GCCs and cobalt-derived GCCs, which may be attributed to the lower initial nucleation temperature of nickel-derived GCCs compared to TG-DTA analysis.

The peaks belonging to the fluoro-tremolite phase from nickel-derived GCCs were more intense than those from cobalt-derived GCCs. The fluoride concentration of the frits may be responsible for the differences in crystalline peak intensities.

In general, almost all crystal intensities of industrial raw material-derived glass-ceramic structures gave higher results than waste-derived glass-ceramic structures. This can be attributed to the complex structure of COPR. Peaks that could not be found in the reference library were detected around 39°, 43° and 65°. The reason for this may be that the cards for the obtained structures are not included in the library or that the complex crystal structures formed more than once overlap each other.

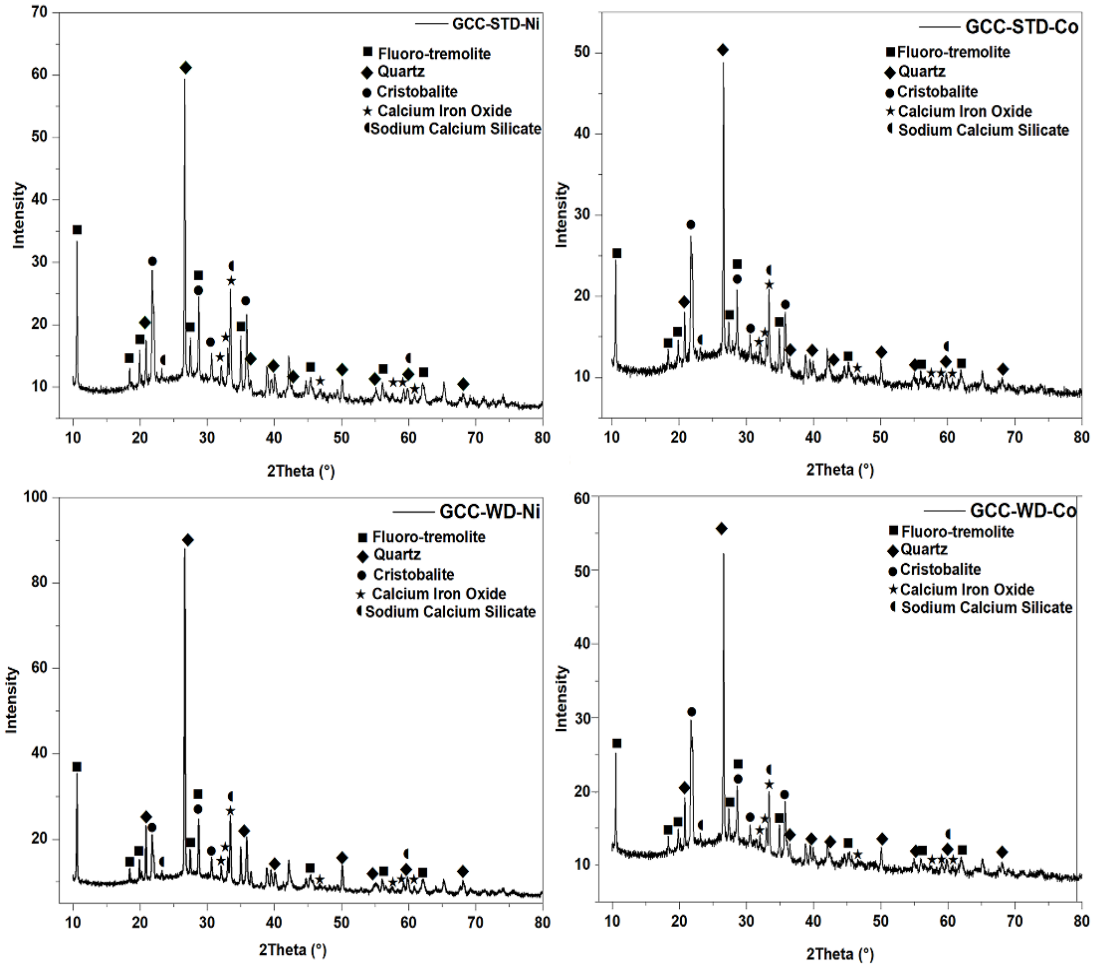


Figure 7.14 XRD analysis results of glass ceramic coatings

7.5.2 Microstructure Analysis

Figure 7.15, 7.16, 7.17, 7.18 and 7.19 are the analysis results of the coating surface and its interface to obtain information about the microstructure of the coatings and to examine the effect of COPR use on the microstructure. When the figure 7.15 SEM analysis was examined, it was proven that all four coatings contained similar structures. Results were obtained using BSE format. The coatings consist of spherical and needle-shaped crystal and glass matrix.

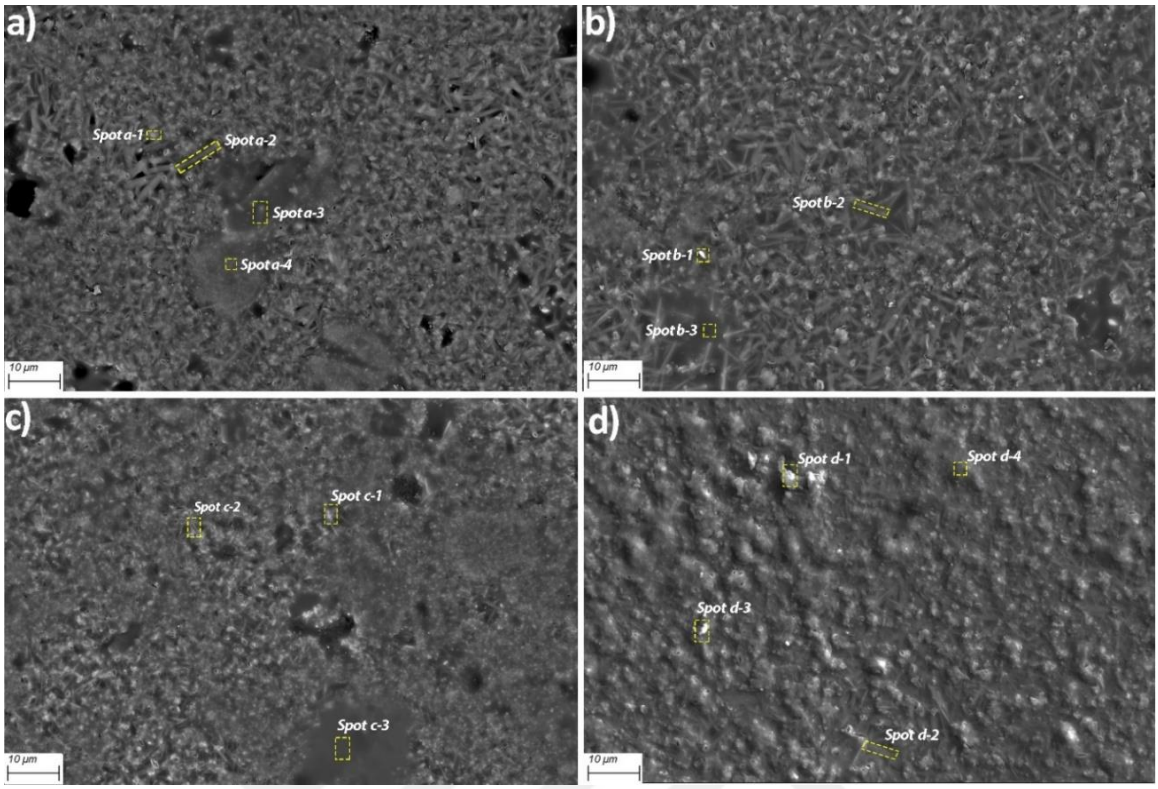


Figure 7.15 SEM analysis of glass ceramic surfaces a) GCC-STD-Ni b) a) GCC-STD-Co c) WD-Ni d) WD-Co

The regions in needle and spherical form are similar to the literature images of tremolite, calcium silicate and quartz phases obtained as a result of XRD analysis. Spot a-2, Spot b-2, Spot c-2 and Spot d-2, unlike the general structure, contain high amounts of Mg and Si. This result can be attributed to the formation of fluoro-tremolite crystals seen in the XRD analysis [119]. Some of the spherical spot areas contain high amounts of Si, unlike the general structure; it can be attributed to the presence of Quartz and cristobalite phases detected as a result of XRD analysis [120].In addition, in some of these structures, there are areas with very high Ca and Na content, which can be attributed to the presence of Sodium Calcium Silicate structures [121].

Table 7.9 EDS point elemental distribution of glass ceramic coatings

Element (% wt.)	GCC-STD-Ni				GCC-WD-Ni		
	Spot a-1	**Spot a-2**	**Spot a-3**	**Spot a-4**	**Spot c-1**	**Spot c-2**	**Spot c-3**
Si	36.85	29,60	51,27	35,44	34,27	29,73	29,82
O	29,42	36,40	41,66	45,48	33,01	39,59	48,17
Mg	1,62	4,16	0,74	1,56	1,34	3,43	1,53
Ca	11,09	6,39	0,19	3,96	13,43	6,87	5,17
Na	4,61	6,05	1,66	7,18	5,19	6,64	8,54
F	0,21	1,19	0,21	0,44	0,00	0,80	0,48
Ti	3,51	2,18	0,03	1,07	2,94	1,90	1,34
Zr	3,15	3,09	2,09	1,64	0,00	0,00	0,00
Fe	1,42	0,74	0,21	0,52	2,68	1,01	0,92
Cr	0,25	0,19	0,08	0,05	0,00	0,07	0,05
Al	1,22	0,65	1,01	0,97	2,14	0,82	2,10
Ni	6,03	9,10	0,64	1,40	4,47	8,90	1,61
K	0,38	0,17	0,07	0,16	0,52	0,12	0,15
Mn	0,24	0,08	0,12	0,13	0,00	0,11	0,11

Table 7.9 EDS point elemental distribution of glass ceramic coatings (continued)

Element (% wt.)	GCC-STD-Co			GCC-WD-Co			
	Spot b-1	**Spot b-2**	**Spot b-3**	**Spot d-1**	**Spot d-2**	**Spot d-3**	**Spot d-4**
Si	32,22	32,41	29,78	33,10	32,41	35,03	26,46
O	43,01	40,36	43,58	41,50	40,36	43,48	49,04
Mg	1,61	3,32	3,76	1,73	3,32	1,81	3,73
Ca	5,10	7,33	6,33	5,11	7,33	5,58	5,25
Na	7,81	6,98	7,82	8,01	6,98	6,61	8,10
F	0,12	0,32	0,69	0,20	0,32	0,45	0,98
Ti	1,47	2,33	1,83	1,62	2,33	1,65	1,52
Zr	1,93	2,28	1,87	1,69	2,28	1,22	1,20
Fe	0,75	0,79	1,10	0,84	0,79	0,63	0,61
Cr	0,09	0,16	0,19	0,14	0,16	0,09	0,12
Al	3,34	0,90	0,88	3,20	0,90	0,92	0,79
Co	2,22	2,55	1,87	2,40	2,55	2,26	2,00
K	0,22	0,13	0,13	0,22	0,13	0,12	0,08
Mn	0,09	0,13	0,18	0,25	0,13	0,13	0,12

It is observed that the crystals in the microstructures of COPR-derived coatings are more embedded in the glass structure. The reason for this is that the amount of crystals belonging to the GCC-STD-Ni coating is qualitatively higher. The reason for this may be that the first nucleation mobility, which was also revealed in TG-DTA analysis, started

earlier than other coatings. EDS point elemental distributions of glass ceramic coatings are given in detail in Tables 7.9.

When the Figure from 7.16 to 7.20 are examined, bubbles; the dendritic structure and the approximate sizes of the needle crystals, which prove that chemical bonding has occurred, are clearly visible. Coating thickness, crystal sizes and average bubble diameters are also calculated and given on the figure. Coating thicknesses are similar (180 μm) and homogeneous.

Dendritic structures were formed at the metal-enamel interface in all coatings. Thus, a metallic bond is formed between the coating and the metal. Bubble formation is observed in both coatings. During controlled crystallization, the carbon in the metal substrate oxidizes and becomes a gas and collects in the glass ceramic coating layer. Components that become volatile with increasing temperature (e.g. fluorine) also try to leave the structure. They cannot overcome surface tension and accumulate in areas close to the surface. Since the temperature is higher than the melting temperature, it is assumed that the bubbles coalesce without exceeding the surface tension. It was observed that the number of bubbles in the coating samples is high and has a heterogeneous distribution. Nickel and cobalt play a key role successfully as a adhesion agents with the metal surface, and dentrite formations are clearly visible in the Figure from 7.16 to 7.20 for all glass-ceramic coatings SEM images of cross-section between glass-ceramic coating and steel substrate.

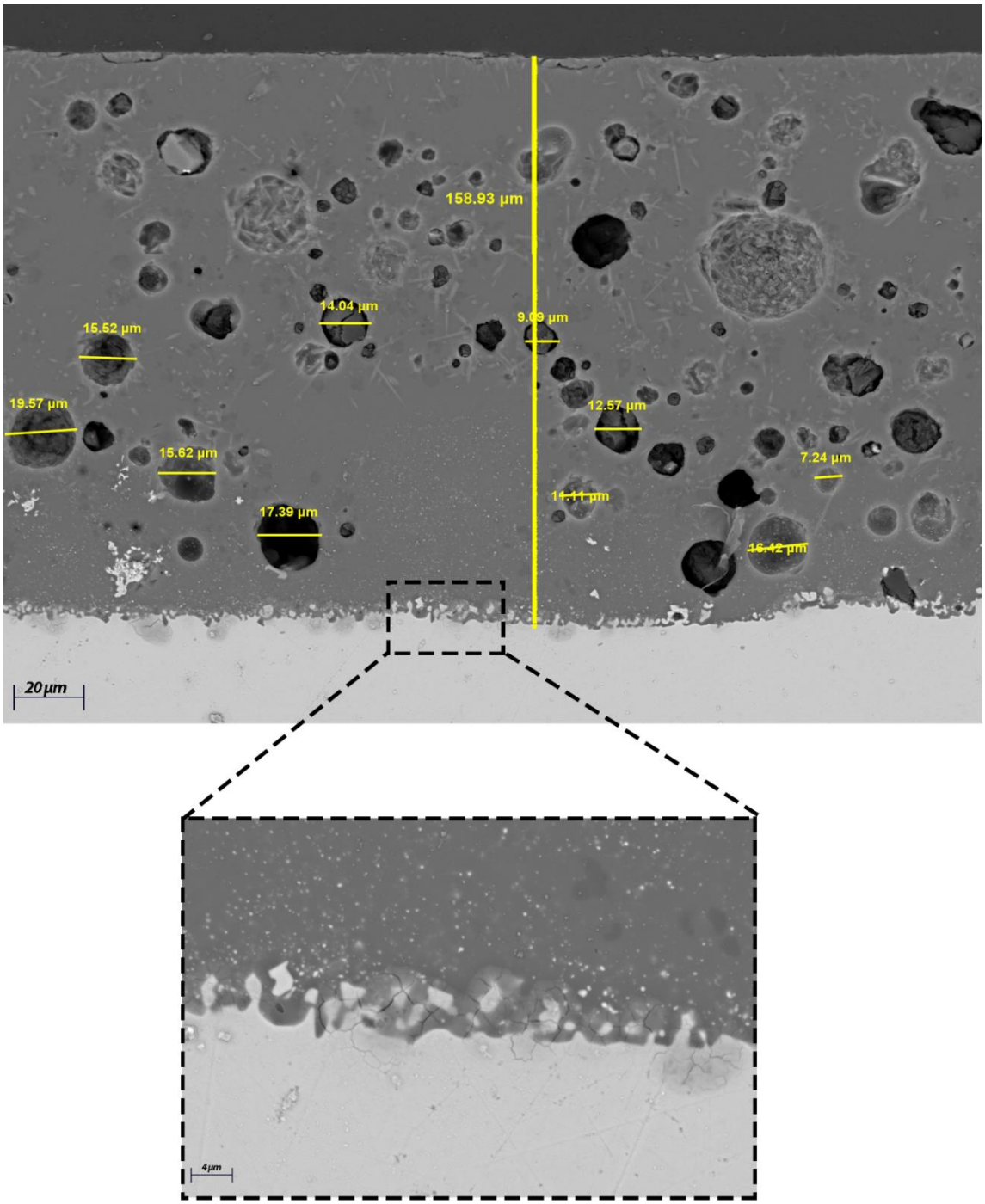


Figure 7.16 SEM imaging of cross-section between glass-ceramic coating and steel substrate of GCC-STD-Ni

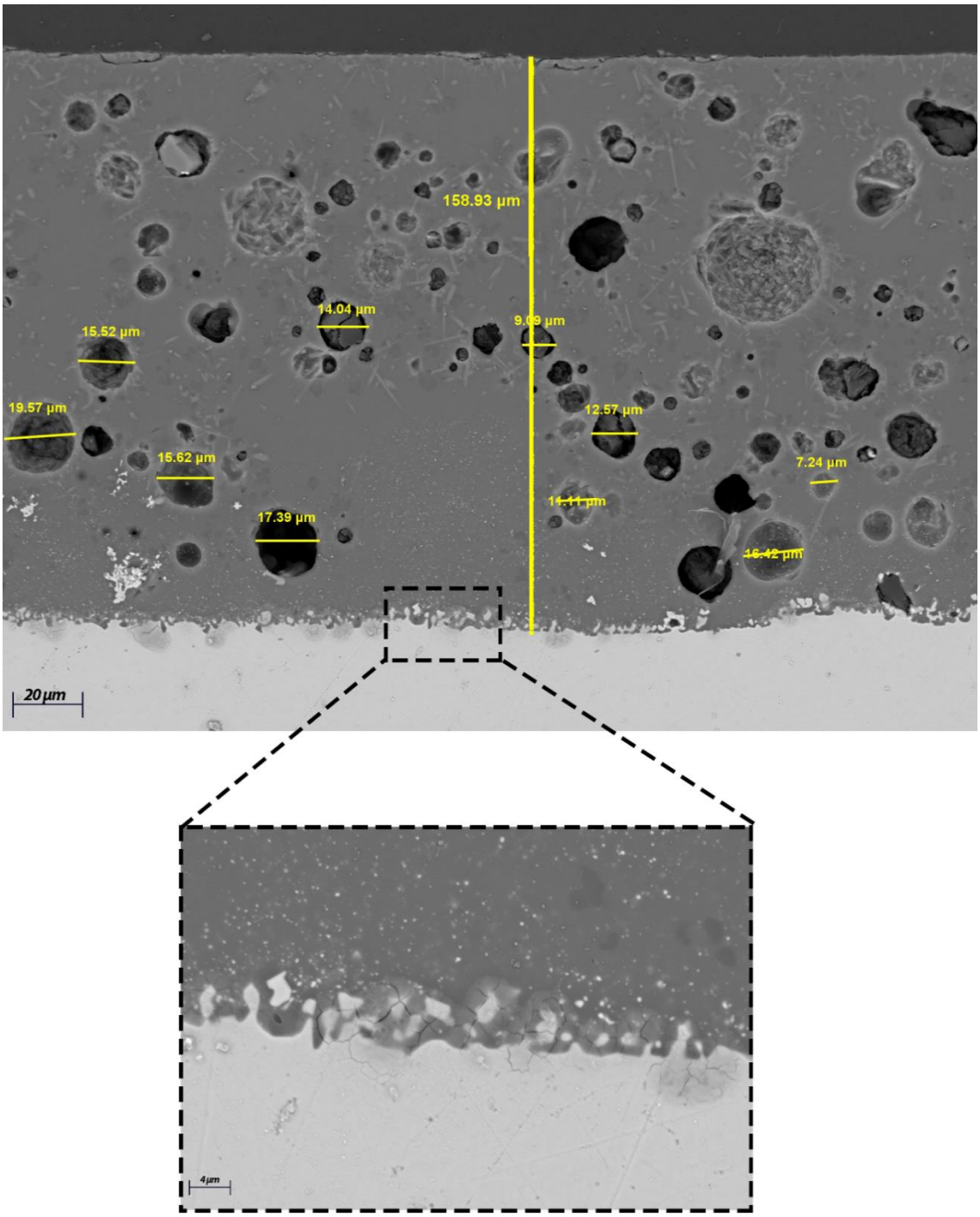


Figure 7.17 SEM imaging of cross-section between glass-ceramic coating and steel substrate of GCC-STD-Co

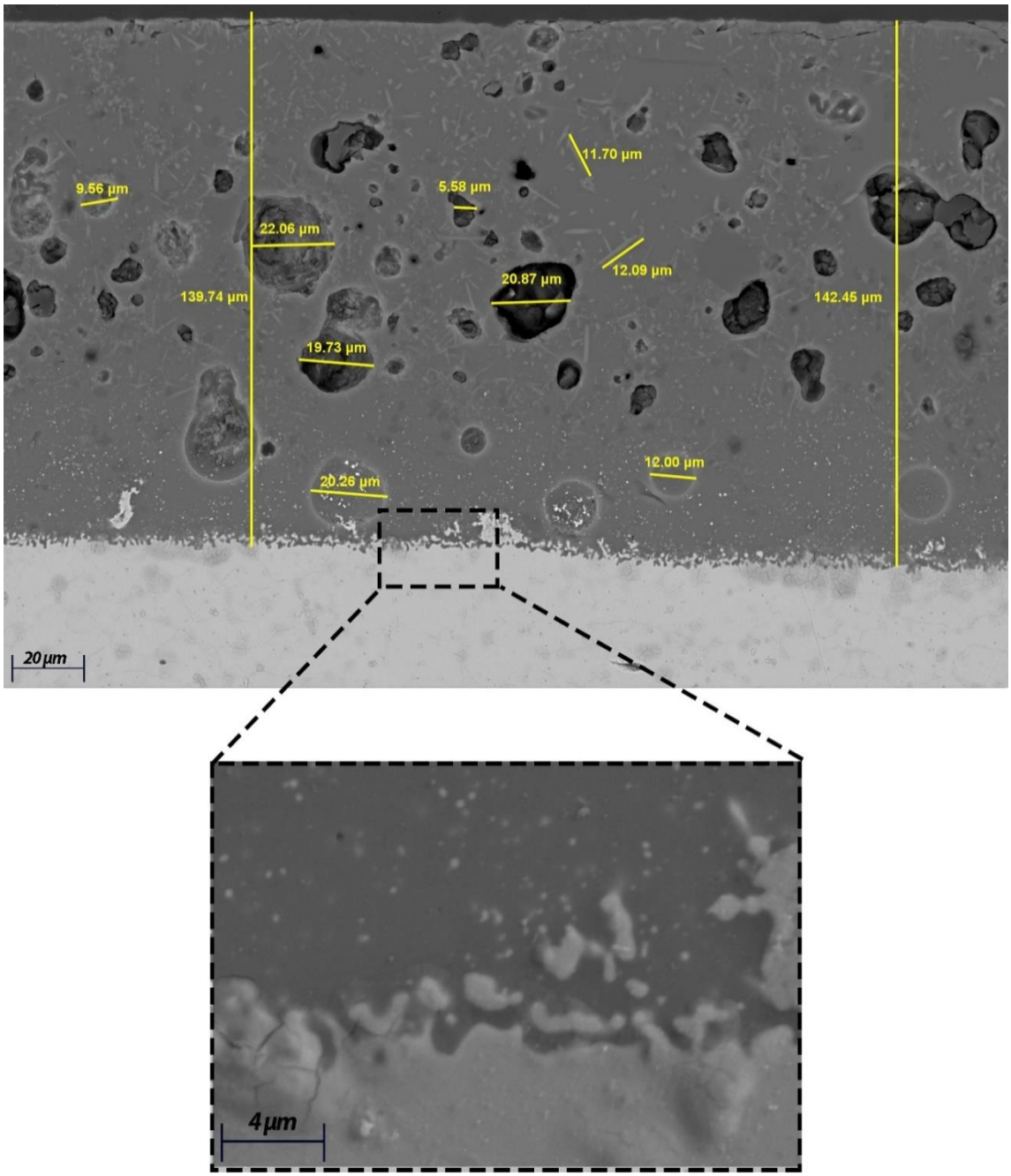


Figure 7.18 SEM imaging of cross-section between glass-ceramic coating and steel substrate of GCC-WD-Ni

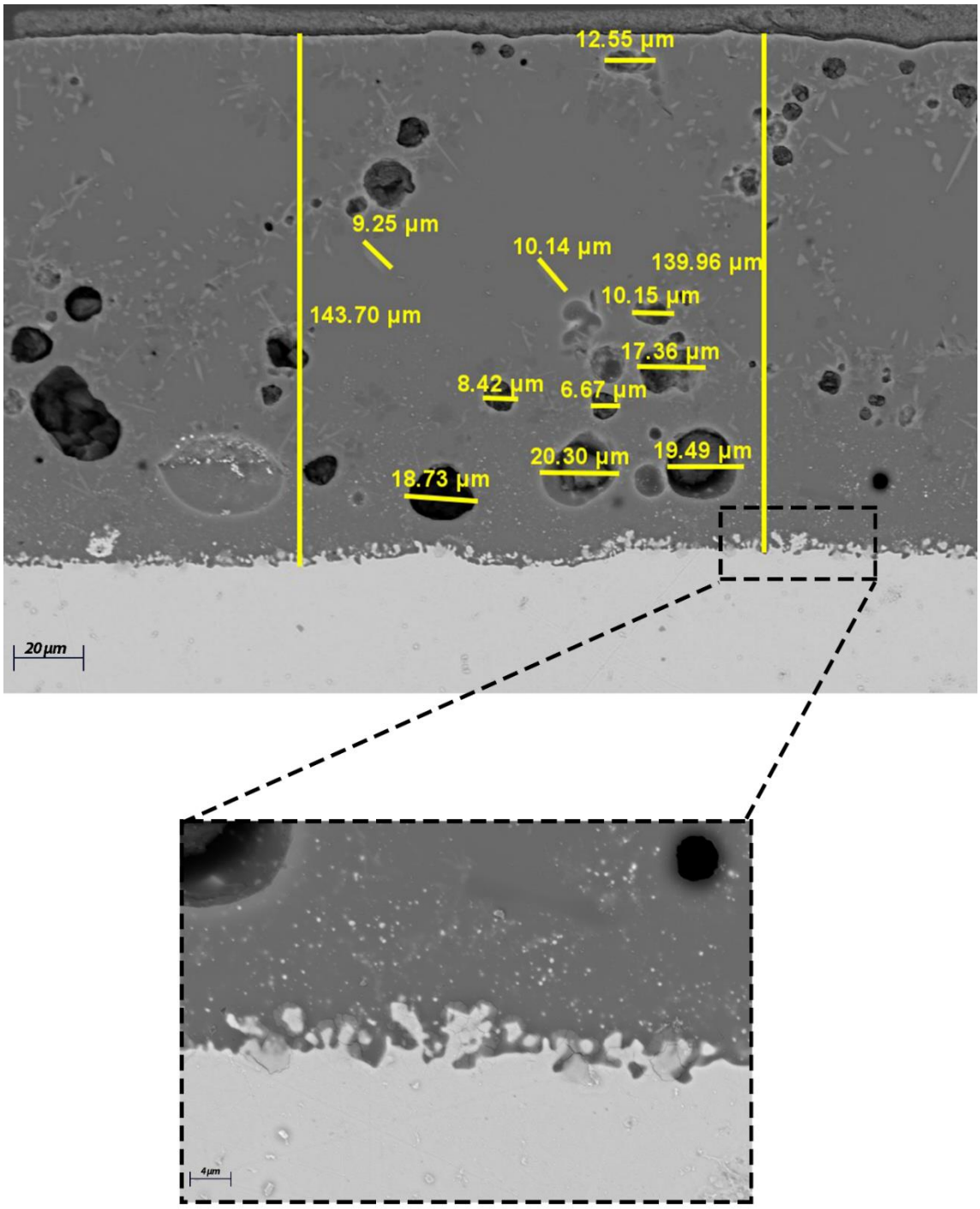


Figure 7.19 SEM imaging of cross-section between glass-ceramic coating and steel substrate of GCC-WD-Co

7.5.3 Color Measurement

The plates are colored thanks to the metal oxides they contain. No external colorant was used during the application. Nickel-based coatings show the color of the mixture of metal oxides; cobalt-based coatings, on the other hand, reflect the blue color specific to cobalt and appear to have a different undertone of blue due to the effect of other metal oxides. The plates that were coated and color values were measured are shown in Figure 7.20.

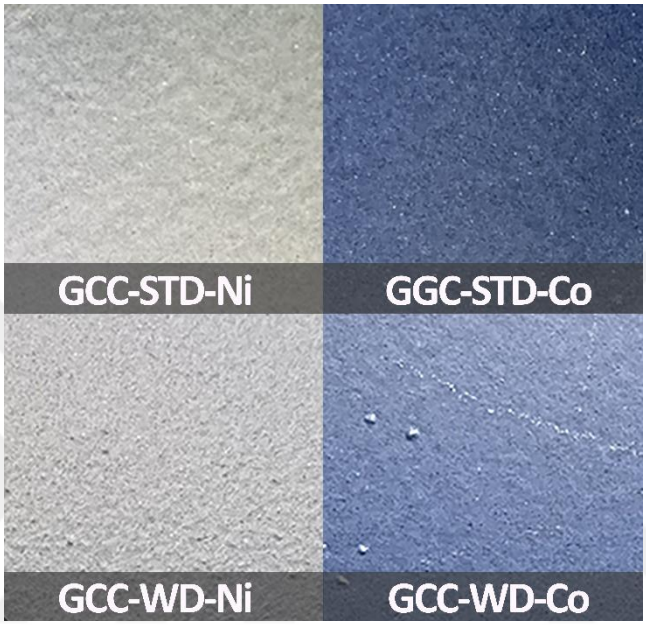


Figure 7.20 Glass ceramic coatings low magnification optical microscope images

Color measurement of enamel applied plates was carried out in the CIE L*a*b* color space. Table 7.10 gives the color measurement values of glass ceramic coatings. When GCC-STD-Ni and GCC-WD-Ni plates were compared with the SCI method, a difference of approximately 0.7 in the L* value was detected. The fact that the L* value of the GCC -STD-Ni plate is 0.7 higher indicates that the color is lighter (white). On the other hand, the a* value of GCC-STD-Ni plate is approximately 0.4 higher and the b* value is approximately 0.3 higher. A higher a* value indicates that the color is redish, and a higher b* value indicates that the color is more yellow. Since the surface properties of the coatings affect the color values, the SCE method was used to examine the color properties of the final product. Measurements similar to those taken with the SCI method were observed. When comparing the GCC-STD-Ni plate with the GCC-WD-Ni plate, a difference of approximately 0.8, 0.5 and 0.3 was detected in the L*, a* and b* values, respectively.

When GCC-STD-Co and GCC-WD-Co plates were compared with the SCI method, a difference of approximately 0.5 in the L* value was detected. A higher L* value of 0.5 of the GCC-STD-Co plate indicates that the color is lighter (white). On the other hand, the a* value of the GCC-STD-Co plate is approximately 0.3 more and the b* value is approximately 0.7 less. A higher a* value indicates that the color is redder, and a lower b* value indicates that the color is more blue. Since the surface properties of the coatings affect the color values, the SCE method was used to examine the color properties of the final product. Measurements similar to those taken with the SCI method were observed. When comparing the GCC-STD-Co plate with the GCC-WD-Co plate, a difference of approximately 0.8, 0.6 and 1.5 was detected in the L*, a* and b* values, respectively. Since the differences in color values are in the same direction and very close, no significant color change was observed due to surface properties.

Table 7.10 Color measurement of glass ceramic coatings

	SCI D65		
	L	**a**	**b**
GCC-STD-Ni	43,91±0,13	-3,17±0,04	0,21±0,09
GCC-WD-Ni	43,23±0,24	-3,58±0,17	-0,12±0,1
GCC-STD-Co	34,15±0,17	2,31±0,01	-13,26±0,26
GCC-WD-Co	32,61±0,01	1,99±0,08	-12,57±0,1
	SCE D65		
	L	**a**	**b**
GCC-STD-Ni	43,16±0,12	-3,28±0,04	0,13±0,1
GCC-WD-Ni	42,41±0,02	-3,74±0,2	-0,14±0,05
GCC-STD-Co	32,90±0,11	2,40±0,01	-13,90±0,25
GCC-WD-Co	30,86±0,51	1,78±0,03	-12,41±0,09

According to the color difference measurement ΔE calculations mentioned in Equation 6.1; according to SCI and SCE measurement methodologies, in nickel-based coatings; 0.85, 0.91 color changes were recorded, while 1.71, 0.47 color changes were recorded in cobalt-based coatings. Among the color change measurements, only 1 (1.71) was at a level that could be noticed through close observation; The other 3 results are too low to be detected by the human eye.

7.5.4 Gloss Measurement

The gloss of glass ceramic coatings was examined and shown in Table 7.11 respectively. The brightness values for GCC-STD-Ni, GCC-WD-Ni, GCC-STD-Co and GCC-WD-Co structures are 9.1, 8.4, 9.9 and 8.9, respectively. The difference in gloss between coatings containing industrial raw materials and those containing waste is around 1 GU. According to the literature, as the SiO_2 content increases, the brightness decreases [122]. The relatively low brightness value of GCC-WD-Ni supports this statement. Changing COPR did not result in any change in the aesthetic properties of the coatings.

Table 7.11 Gloss measurement of glass ceramic coatings

Sample Code	Gloss Value 60°
GCC-STD-Ni	9,1 ± 0,2
GCC-WD-Ni	8,4 ± 0,2
GCC-STD-Co	9,9 ± 0,25
GCC-WD-Co	8,9 ± 0,3

7.5.5 Acid Resistance Analysis

Glass-ceramic coatings, particularly in kitchenware applications, are consistently exposed to acid attacks. The presence and continuity of the $[SiO_4]$ structure within the glass-ceramic coatings play a crucial role in determining their acid resistance. SiO_2, being a key oxide, significantly influences acid resistance. Tetrahedrons composed of $[SiO_4]$ are employed to envelop the surroundings of $\{[AlO_4] - R^+\}$ and $\{[BO_4] - R^+]\}$ structures in order to shield them from the corrosive impact of acid. Essentially, an increase in SiO_2 content in the glass-ceramic coating formulation enhances acid resistance. Conversely,

the enlargement of the R_2O group in the structure, induced by ions like Li^+, Na^+, and K^+, disrupts the continuity of [SiO_4] tetrahedrons, resulting in decreased acid resistance[55].

To conduct the acid resistance test on the enamel coating, a solution is formulated using 10 g citric acid monohydrate and 100 mL distilled water, following the ISO 28706-2 standard. Subsequently, 4 mL of the prepared solution is applied to the enamel surface and allowed to stand for 15 minutes. During the test, the acid-exposed area is covered with a cap to prevent the evaporation of the solution[123]. To grade the cold citric acid test, a pencil line was drawn over the area where the acid test was conducted. The optimal acid resistance is represented by the test result's AA, whereas a failure is shown by the letter D. The test result of all samples is AA.

7.5.6 Coating Thickness

Following the coating application and the firing process, an analysis of the coating thickness of the enamel coating was conducted. This investigation aimed to assess the distribution of homogeneous coating thickness and any changes in coating thickness after the abrasion test. The DeFelsko Positest DFT Combo model coating thickness gauge was used for this analysis, in accordance with the ISO 2178:2016 standard[124]. According to the measurement results, the coating thickness was 150 ±10 μm for all samples.

7.5.7 Impact Resistance Analysis

The impact resistance, or adhesion ability, of enamels is evaluated by employing a 22 mm diameter cylinder apparatus with a weight of 1.5 kg. This apparatus is released from a height of 75 cm onto a metal surface coated with enamel, following the specifications outlined in the BS EN ISO 10209:2013 standard. The analysis is conducted to assess the impact of a 15 kJ energy on the enamel surface, adhering to the standard procedures[125].

The impact test results conducted in accordance with the BS EN ISO 10209:2013 standard is depicted in Figure 7.21. The impact test results for all samples were designated as 1. The outcomes of the impact test indicate that the coatings exhibit optimal adhesion. Furthermore, it was observed that the substitution of COPR into the structure does not lead to a significant alteration in impact strength.

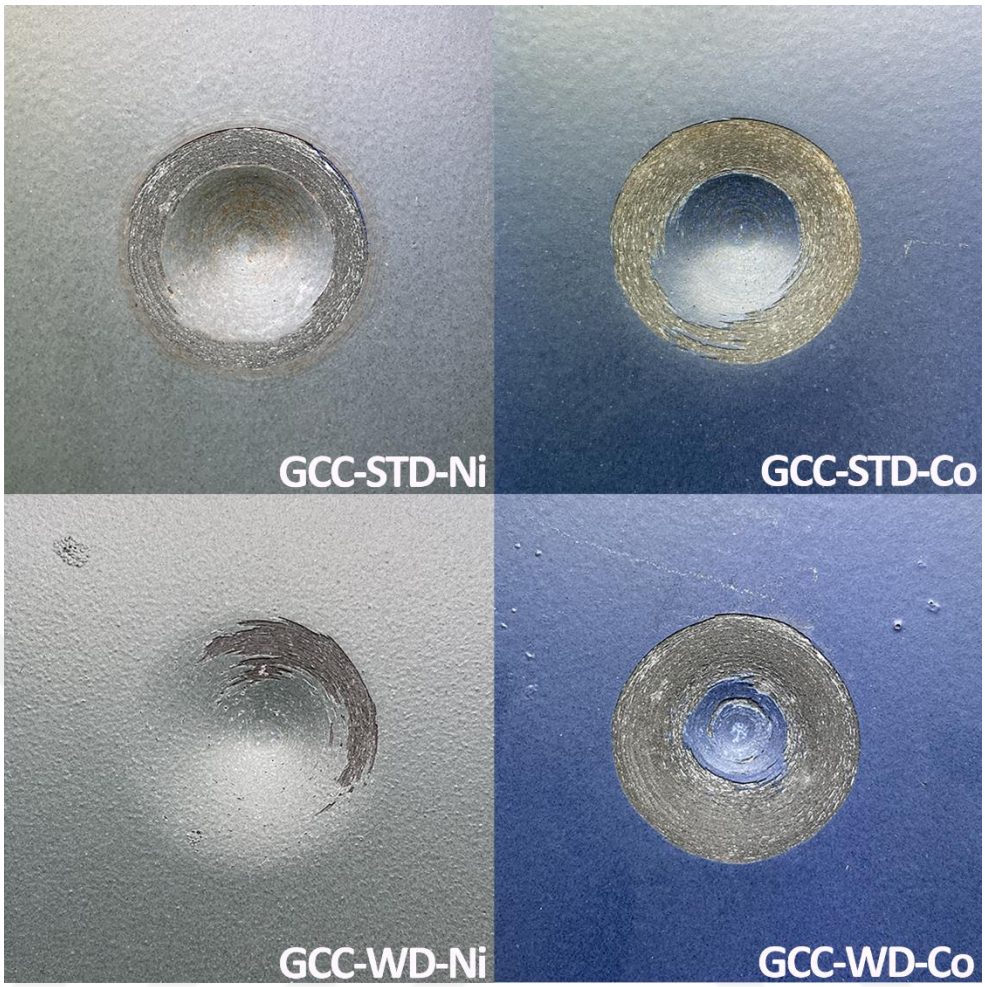


Figure 7.21 Impact test results of the glass ceramic coatings

8
CONCLUSION

This study investigates the potential use of chromite mine wastes as alternative raw materials in sodium borosilicate glass-ceramic coatings. It also explores the adhesion of agents (NiO and CoO) facilitating bonding to steel surfaces and assesses their compatibility with waste and coating properties.

XRF analysis shows the predominant components in supplied waste are 36.33 wt.% MgO and 32.85 wt.% SiO_2, while 15.56 wt.% minor components include Fe_2O_3, C, and Cr_2O_3.

In the TG-DTA analysis, a total mass loss of 15.56 wt.% is observed. In addition to the mass losses, there are three main reaction points: two exothermic reactions at 550°C-1135°C and one endothermic reaction at 819°C. Reaction points can be explained the separation of carbon from the structure observed in the XRF analysis at 550°C is associated with the crystal phase and polymorphic transformations of the lizardite phase observed in the XRD analysis at 819°C and 1135°C. According to the TG-DTA analysis critical points heat treatments were observed. Calcination performance was clearly observed in XRF analysis, and with the removal of carbon, the concentrations of magnesium, which is the major component, in the structure increased. The amount of carbon in the structure; it decreased from 6.46 wt.% to 2.49 wt.%. With this decrease, magnesium concentration increased from 42.72% wt.% to 45.62% wt.

XRD patterns shows all heat-treated samples contain amorphous and crystalline phases together. Upon examining the samples subjected to low-temperature heat treatment, the prevalent phases in the structure are chrysotile and lizardite. However, as the calcination temperature increases, these structures transform into forsterite and enstatite phases. In terms of minor phases reveals that the brucite and hillebrandite phases disapperad with rising temperature, while the magnesiochromite phase becomes visible.

According to the FT-IR analysis results of the samples; vibrations of Si, O, Al, Mg elements, whose elemental presence in the structure is confirmed by XRF analysis, are displayed. All FT-IR curves are similar to each other. In addition, the -OH structure is observed at 3686 cm^{-1} in samples belonging to low calcination temperatures. Peaks of between 900-1000 cm^{-1} represents the asymmetrical stretching vibration of Si-O-T (T =

Si, Al). The peak at 612 cm^{-1} represents Mg-O bond and bands at around 542 cm^{-1} and 426 cm^{-1} in all samples are attributed to Si-O and Al-O bonds, respectively.

The Raman analysis results confirm the FT-IR analysis results and indicate the presence of the O-H-O group. The peaks associated with this structure diminish at higher calcination temperatures, along with the bonds related to Si, Al, and Mg structures. Furthermore, the Raman analysis reveals characteristic peaks corresponding to the phases identified in the XRD analysis. The main peaks of the lizardite phase at 230 cm^{-1}, 390 cm^{-1}, 690 cm^{-1}, and 1100 cm^{-1} are observed in the immediate vicinity of the structure. As the calcination temperature increases, the XRD analysis demonstrates dehydroxylation reactions, leading to the replacement of lizardite crystals by the forsterite phase. Additionally, in the Raman analysis, the intensities of the main lizardite peaks decrease and are supplanted by peaks at 820 cm^{-1} and 860 cm^{-1}, indicative of the forsterite phase.

SSA and PV values increase as the calcination temperature increases. The reason for this can be explained by the loss of moisture and carbon in the structure over time, as revealed by XRF analysis. Differently, in the C-1150 sample, there was a sharp decrease in SSA and PV values. The reason for this can be explained by the transformation of the structure into a more dense form. Thermal microscopy analysis of waste; this explains the sudden decline. The waste showed sintering properties, losing 5% of its structural volume around 895°C.

When microstructure images of waste samples are examined carbon moving away from the structure, cracked areas form on the surface of the structure, and while the percentage of elemental carbon decreases.

PG-WD glass systems, produced using approximately 3.5 wt.% COPR, exhibit similar chemical compositions to PG-STD glass systems produced entirely from commercial raw materials. The XRD patterns of the precursor glass structures have a broad peak related for amorphous structure of a typical silicate glass.

The glass transition temperatures are quite close to each other: 515°C, 518°C, 513°C and 511°C for PG-STD-Ni, PG-WD-Ni, PG-STD-Co and PG-WD-Co, respectively. A broad exothermic peak in the range of 600-700°C was observed for all four PGs. Also HSM and dilatometer analysis were confirmed that similar thermal behaviours STD and WD PGs each other. All glass structures; have similar characteristic points and reaction tendencies.

The temperature differences that exist between them can be explained by chemical composition differences.

According to XPS analysis, the Cr element was fully in the Cr^{6+} state in the D-200 sample. The C-1150 and PG-WD-Ni samples showed a partial reduction of Cr^{6+} due to the combined effects of temperature and Mg. The PG-WD-Co sample, however, demonstrated a complete transformation to $Cr3^{+}$.

After crystallization steps; XRD analysis shows the all GCC samples have similar crystalline structure. Amorphous structure and five different crystalline phases are presence all samples.

These phases; Fluoro-tremolite with $Ca_2Mg_5(Si_4O_{11})_2F_2$ formulation (PDF#00-009-0330), quartz with SiO_2 formulation (PDF#00-022-1161) and cristobalite (PDF#82-0512), $Ca_2Fe_2O_5$ (PDF#01-086). Calcium iron oxide with the formulation and sodium calcium silicate crystals with the formulation $Na_4CaSi_3O_9$.

The coatings also consist of spherical and needle-shaped crystal and glass matrix. The regions in needle and spherical form are similar to the literature images of tremolite, calcium silicate and quartz phases. These results are confirmed by XRF and semi-quantitative EDS elemental analysis. It is observed that the crystals in the microstructures of COPR-derived coatings are more embedded in the glass structure. The reason for this is that the amount of crystals belonging to the GCC-STD-Ni coating is qualitatively higher. The reason for this may be that the first nucleation mobility, which was also revealed in TG-DTA analysis, started earlier than other coatings.

Since no additional colorant was used during the creation of the GCC structures, the color values of the coatings are unique to them. When all performance and aesthetic properties were compared between STD and WD glass ceramic coatings, it was observed that the use of waste had a negligible effect and did not directly affect the results.

Chromite mine wastes pose significant processing challenges due to their constituent components and the potential presence of Cr^{6+} ions. However, the substantial reduction of Cr^{6+} ions to Cr^{3+} ions during the formulation and vitrification processes, compatible with waste components, suggests that chromite ore ocessing residue (COPR) can be a viable source of SiO_2 and MgO. This transformation supports a sustainable approach to producing glass-ceramic coatings. Consequently, COPR has emerged as a promising alternative raw material to traditional industrial inputs.

This indicated that COPR could be a suitable raw material source for SiO_2 and MgO for a sustainable production approach in glass ceramic coating. COPR has become an alternative raw material to industrial raw materials.

REFERENCES

[1] G. H. Beall, “Dr. S. Donald (Don) Stookey (1915–2014): Pioneering researcher and adventurer,” *Front. Mater.*, vol. 3, no. August, pp. 1–8, 2016, doi: 10.3389/fmats.2016.00037.

[2] P. W. McMillan, “The crystallisation of glasses,” *J. Non. Cryst. Solids*, vol. 52, no. 1–3, pp. 67–76, 1982, doi: 10.1016/0022-3093(82)90281-2.

[3] J. Deubener *et al.*, “Updated definition of glass-ceramics,” *J. Non. Cryst. Solids*, vol. 501, no. February, pp. 3–10, 2018, doi: 10.1016/j.jnoncrysol.2018.01.033.

[4] I. S. Gutzow and J. W. P. Schmelzer, *Kinetics of Overall Crystallization: Kinetic Criteria for Glass-Formation BT - The Vitreous State: Thermodynamics, Structure, Rheology, and Crystallization*. 2013.

[5] L. F. de Lima, J. E. Zorzi, and R. C. D. Cruz, “Basaltic glass-ceramic: A short review,” *Bol. la Soc. Esp. Ceram. y Vidr.*, vol. 61, no. 1, pp. 2–12, 2022, doi: 10.1016/j.bsecv.2020.07.005.

[6] J. Deubener *et al.*, “Updated definition of glass-ceramics,” *J. Non. Cryst. Solids*, vol. 501, no. February, pp. 3–10, 2018, doi: 10.1016/j.jnoncrysol.2018.01.033.

[7] C. Ye *et al.*, “Preparation and properties of sintered glass-ceramics containing Au-Cu tailing waste,” *Mater. Des.*, vol. 86, pp. 782–787, 2015, doi: 10.1016/j.matdes.2015.07.173.

[8] Y. Liu *et al.*, “Cr(VI) recovery from chromite ore processing residual using an enhanced electrokinetic process by bipolar membranes,” *J. Memb. Sci.*, vol. 566, no. May, pp. 190–196, 2018, doi: 10.1016/j.memsci.2018.07.079.

[9] WolframHöland, “Glass-ceramic technology,” *Choice Rev. Online*, vol. 39, no. 10, pp. 39-5831-39–5831, Jun. 2002, doi: 10.5860/CHOICE.39-5831.

[10] C. Z. Liao, Y. Tang, P. H. Lee, C. Liu, K. Shih, and F. Li, “Detoxification and immobilization of chromite ore processing residue in spinel-based glass-ceramic,” *J. Hazard. Mater.*, vol. 321, pp. 449–455, 2017, doi: 10.1016/j.jhazmat.2016.09.035.

[11] Z. Yang *et al.*, “Effective removal of Cr(VI) from aqueous solution based on

APTES modified nanoporous silicon prepared from kerf loss silicon waste," *Environ. Sci. Pollut. Res.*, vol. 27, no. 10, pp. 10899–10909, 2020, doi: 10.1007/s11356-019-07427-6.

[12] P. Zhang, L. Zeng, S. Zhang, C. Li, and D. Li, "Solidification/stabilization of chromite ore processing residue via co-sintering with hazardous waste incineration residue," *Environ. Sci. Pollut. Res.*, vol. 30, no. 11, pp. 29392–29406, 2023, doi: 10.1007/s11356-022-24318-5.

[13] B. Li, C. Chen, Y. Zhang, L. Yuan, H. Deng, and W. Qian, "Preparation of glass-ceramics from chromite-containing tailings solidified with Red Mud," *Surfaces and Interfaces*, vol. 25, no. March, p. 101210, 2021, doi: 10.1016/j.surfin.2021.101210.

[14] L. Deng *et al.*, "Crystallization behavior and structure of CaO–MgO–Al2O3–SiO2 glass ceramics prepared from Cr-bearing slag," *Mater. Chem. Phys.*, vol. 261, no. November 2020, p. 124249, 2021, doi: 10.1016/j.matchemphys.2021.124249.

[15] Z. Bayer Öztürk and S. Dal, "Characterization of industrial ceramic glazes containing chromite processing waste: Experimental factorial design effects on color parameters," *Mater. Chem. Phys.*, vol. 282, no. August 2021, pp. 1–10, 2022, doi: 10.1016/j.matchemphys.2022.125928.

[16] H. Chen *et al.*, "Immobilisation of heavy metals in hazardous waste incineration residue using SiO2–Al2O3–Fe2O3–CaO glass-ceramic," *Ceram. Int.*, vol. 47, no. 6, pp. 8468–8477, 2021, doi: 10.1016/j.ceramint.2020.11.213.

[17] Ş. Kilinçarslan and Z. R. Kaya, "Usage of chromite wastes as aggregate in foam concrete production," *Arab. J. Geosci.*, vol. 11, no. 18, 2018, doi: 10.1007/s12517-018-3890-y.

[18] M. Chrysochoou and D. Dermatas, "An overview of the properties and treatment of chromite ore processing residue (COPR)," *Manag. Hazard. Residues Contain. Cr(VI)*, no. September 1998, pp. 265–294, 2011.

[19] G. Liao, J. Hu, Z. Chen, R. Zhang, G. Wang, and T. Kuang, "Preparation, properties, and applications of graphene-based hydrogels," *Front. Chem.*, vol. 6, no. SEP, pp. 1–5, 2018, doi: 10.3389/fchem.2018.00450.

[20] N. I. Min and T. A. Matveeva, "Glass Enamels For Steel And Cast-Iron Articles,"

Glas. Ceram., vol. 56, no. 047, pp. 358–363, 2000.

[21] A. Tunali, E. Ozel, and S. Turan, "Production and characterisation of granulated frit to achieve anorthite based glass-ceramic glaze," *J. Eur. Ceram. Soc.*, vol. 35, no. 3, pp. 1089–1095, 2015, doi: 10.1016/j.jeurceramsoc.2014.09.039.

[22] V.V. Vargin (Author) and K. Shaw, *Technology of Enamels*. .

[23] S. D. Stookey, "History of the Development of Pyroceram," *Res. Manage.*, vol. 1, no. 3, pp. 155–163, 1958, doi: 10.1080/00345334.1958.11755484.

[24] *Glasses and Glass-Ceramics*. 1989.

[25] James F. Shackelford, *Ceramic and Glass Materials*. Boston, MA: Springer US, 2008.

[26] V. Günay and Ş. Yılmaz, *Glass Ceramics: Science and Technology (Cam Seramikler: Bilim ve Teknolojisi)*. 2010.

[27] D. R. Uhlmann, "A Kinetic Treatment of Glass Transition," *J. Non. Cryst. Solids*, vol. 7, pp. 337–348, 1972.

[28] G. Beall, "Design and Properties of Glass-Ceramics," *Annu. Rev. Mater. Res.*, vol. 22, no. 1, pp. 91–119, 1992, doi: 10.1146/annurev.matsci.22.1.91.

[29] L. Fu, H. Engqvist, and W. Xia, "Glass – Ceramics in Dentistry : A Review," 2020.

[30] W. D. I and W. M. P, "Review Ceramic-matrix composites," *J. Mater. Sci.*, vol. 11, pp. 949–972, 1976.

[31] Q. Fu, G. H. Beall, and C. M. Smith, "Nature-inspired design of strong, tough glass-ceramics," *MRS Bull.*, vol. 42, no. 3, pp. 220–225, 2017, doi: 10.1557/mrs.2017.31.

[32] J. E. Shelby, *Intoduction to Glass Science and Technology*. 2005.

[33] "Industrial Porcelain Enameling Processes." https://www.ditmer.nl/EN/Enameling/Process/.

[34] Anonim, "Maden Tetkik ve Arama Genel Müdürlüğü-Heyelan Haritaları," 2023, [Online]. Available: https://www.mta.gov.tr/v3.0/hizmetler/heyelan-haritalari.

[35] E. Yılmaz, "Taban malzeme emaye arayüz ilişkilerinin emaye kalitesine etkisi," *Lincolin Arsyad*, vol. 3, no. 2, p. 139, 2014, [Online]. Available:

http://journal.stainkudus.ac.id/index.php/equilibrium/article/view/1268/1127.

[36] L. Kang, T. Liu, Z. Su, and Y. Kong, "Research on glass ceramics with negative coefficient of thermal expansion used as fiber Bragg grating substrate," *Mater. Act. Devices, Opt. Amplifiers*, vol. 5280, p. 638, 2004, doi: 10.1117/12.520427.

[37] H. Hahn *et al.*, "Thermal Expansion of Synthetic β-Spodumene and β-Spodumene-Silica," no. November, pp. 651–654, 1968.

[38] A. Herczog, "Application Of Glass-Ceramics For Electronic Components And Circuits," *IEEE Trans. Parts, Hybrids, Packag.*, vol. 9, no. 4, pp. 247–256, 1973, doi: 10.1109/TPHP.1973.1136735.

[39] A. Sakamoto and S. Yamamoto, "Glass-Ceramics: Engineering Principles and Applications," *Int. J. Appl. Glas. Sci.*, vol. 1, no. 3, pp. 237–247, 2010, doi: 10.1111/j.2041-1294.2010.00027.x.

[40] H. Wang, J. Liu, J. Zhai, and B. Shen, "Ultra High Energy-Storage Density in the Barium Potassium Niobate-Based Glass-Ceramics for Energy-Storage Applications," *J. Am. Ceram. Soc.*, vol. 99, no. 9, pp. 2909–2912, 2016, doi: 10.1111/jace.14446.

[41] L. Samiee, H. Sarpoolaky, and A. Mirhabibi, "Microstructure and adherence of cobalt containing and cobalt free enamels to low carbon steel," *Mater. Sci. Eng. A*, vol. 458, no. 1–2, pp. 88–95, 2007, doi: 10.1016/j.msea.2006.12.108.

[42] A. Majumdar and S. Jana, "Glass and glass-ceramic coatings, versatile materials for industrial and engineering applications," *Bull. Mater. Sci.*, vol. 24, no. 1, pp. 69–77, 2001, doi: 10.1007/BF02704843.

[43] W. D. Faust and O. Usa, *Porcelain (Vitreous) Enamels and Industrial Enamelling Processes*. 2012.

[44] E. D. R. Eppler, R. A., "Glazes and Glass Coatings," *Am. Ceram. Soc.*, 2000.

[45] F. W. . Andrews A. I., Pagliuca S., *Porcelain (vitreous) Enamels and Industrial Enamelling Processes: The Preparation, Application and Properties of Enamel*. International Enamel Institute, 2011.

[46] S. P. Rodtsevich, V. V. Tavgen', and T. S. Minkevich, "Effect of alkali metal oxides on the properties of titanium containing glass enamels," *Glas. Ceram.*, vol.

64, no. 7–8, pp. 244–246, Jul. 2007, doi: 10.1007/s10717-007-0061-0.

[47] Y. LI, J. WANG, and Q. ZHONG, “A Novel Method For Studying The Corrosion Resistance And Microstructure Of Enamel Coating Modified On High-Strength Steel In 3.5 Wt.% Nacl Solution,” *Surf. Rev. Lett.*, vol. 27, no. 02, p. 1950098, Feb. 2020, doi: 10.1142/S0218625X19500987.

[48] S. Agathopoulos, D. U. Tulyaganov, P. Valério, and J. M. F. Ferreira, “A new model formulation of the SiO2–Al2O3–B2O3–MgO–CaO–Na2O–F glass-ceramics,” *Biomaterials*, vol. 26, no. 15, pp. 2255–2264, May 2005, doi: 10.1016/j.biomaterials.2004.07.030.

[49] K. Benzesik, M. İ. Terzioğlu, F. Sahin, and O. Yucel, “Optimizing the Migration Behavior of Enamel Coatings Used as Food Contact Materials,” *19. Uluslararası Met. ve Malzeme Kongresi*, no. January 2019, 2018, [Online]. Available: https://www.researchgate.net/publication/329327438.

[50] A. P. Tomsia and J. A. Pask, “Chemical reactions and adherence at glass/metal interfaces: an analysis,” *Dent. Mater.*, vol. 2, no. 1, pp. 10–16, 1986, doi: 10.1016/S0109-5641(86)80063-X.

[51] B. Karasu, “Emayenin Dünü ve Bugünü (Enamel from Past to Present Time),” no. June, 2020.

[52] H. J. . ELLINGHAM, “Reducibility Of Oxides And Sulphides In Metallurgical Processes,” *Vacuum*, vol. 7–8, p. 216, Apr. 1959, doi: 10.1016/0042-207X(59)90795-X.

[53] W. Conshohocken, “Standard Test Method for Thermal Shock Resistance of Porcelain-Enameled Utensils,” 1998.

[54] G. H. Beall, “Design and Properties of Glass-Ceramics,” *Annu. Rev. Mater. Sci.*, vol. 22, no. 1, pp. 91–119, Aug. 1992, doi: 10.1146/annurev.ms.22.080192.000515.

[55] M. Shu, H. Yin, Q. Zhong, X. Shi, and H. Han, “Effect of glass powder on acid resistance of enamel coating,” *Surf. Rev. Lett.*, vol. 24, no. 3, pp. 1–9, 2017, doi: 10.1142/S0218625X17500366.

[56] F. S. Shieu, M. J. Deng, K. C. Lin, J. C. Wong, and J. Y. Wu, “Effect of surface pretreatments on the adherence of porcelain enamel to a type 316L stainless steel,”

J. Mater. Sci., vol. 34, no. 21, pp. 5265–5272, 1999, doi: 10.1023/A:1004728416960.

[57] M. Chen, W. Li, M. Shen, S. Zhu, and F. Wang, "Glass coatings on stainless steels for high-temperature oxidation protection: Mechanisms," *Corros. Sci.*, vol. 82, pp. 316–327, 2014, doi: 10.1016/j.corsci.2014.01.033.

[58] B. Wunder, R. Wirth, and M. Gottschalk, "Antigorite: Pressure and temperature dependence of polysomatism and water content," *Eur. J. Mineral.*, vol. 13, no. 3, pp. 485–495, 2001, doi: 10.1127/0935-1221/2001/0013-0485.

[59] T. Zhang, Y. Bao, and D. T. Gawne, "Process model of plasma enamelling," *J. Eur. Ceram. Soc.*, vol. 23, no. 7, pp. 1019–1026, 2003, doi: 10.1016/S0955-2219(02)00235-2.

[60] E. I. Kamitsos, J. A. Kapoutsis, H. Jain, and C. H. Hsieh, "Vibrational study of the role of trivalent ions in sodium trisilicate glass," *J. Non. Cryst. Solids*, vol. 171, no. 1, pp. 31–45, Jul. 1994, doi: 10.1016/0022-3093(94)90030-2.

[61] L. T. Alberta, *Environmental Forensics Contaminant Specific Guide*, vol. 01. 2014.

[62] Y. R. Murthy, S. K. Tripathy, and C. R. Kumar, "Chrome ore beneficiation challenges & opportunities - A review," *Miner. Eng.*, vol. 24, no. 5, pp. 375–380, 2011, doi: 10.1016/j.mineng.2010.12.001.

[63] J. F. W. Bowles, *Oxides*, 2nd ed., vol. 1. Elsevier Inc., 2020.

[64] S. K. Haldar, *Minerals and rocks*. 2020.

[65] N. Koleli and A. Demir, *Chromite*, no. 1. Elsevier Inc., 2016.

[66] U. S. G. Survey, J. F. Papp, and B. R. Lipin, "Chromium." doi: https://doi.org/10.3133/ofr01381.

[67] J. F. Papp, "Chromium - A National Mineral Commodity Perspective," 2007.

[68] R. Mohan, L. Deevakar, and V. Sivakumar, "Towards holistic technology solution to chromite ore processing residue (COPR) challenge; global issue: review and analysis," *Int. J. Environ. Sci. Technol.*, vol. 19, no. 1, pp. 665–676, 2022, doi: 10.1007/s13762-020-03097-x.

[69] J. Fruchter, "Peer Reviewed: In-Situ Treatment of Chromium-Contaminated

Groundwater," *Environ. Sci. Technol.*, vol. 36, no. 23, pp. 464A-472A, Dec. 2002, doi: 10.1021/es022466i.

[70] J. J. Coetzee, N. Bansal, and E. M. N. Chirwa, "Chromium in Environment, Its Toxic Effect from Chromite-Mining and Ferrochrome Industries, and Its Possible Bioremediation," *Expo. Heal.*, vol. 12, no. 1, pp. 51–62, Mar. 2020, doi: 10.1007/s12403-018-0284-z.

[71] J. López-Luna, M. C. González-Chávez, F. J. Esparza-García, and R. Rodríguez-Vázquez, "Toxicity assessment of soil amended with tannery sludge, trivalent chromium and hexavalent chromium, using wheat, oat and sorghum plants," *J. Hazard. Mater.*, vol. 163, no. 2–3, pp. 829–834, Apr. 2009, doi: 10.1016/j.jhazmat.2008.07.034.

[72] R. Saha, R. Nandi, and B. Saha, "Sources and toxicity of hexavalent chromium," *J. Coord. Chem.*, vol. 64, no. 10, pp. 1782–1806, May 2011, doi: 10.1080/00958972.2011.583646.

[73] K. Freese, R. Miller, T. Cutright, and J. Senko, "Review of Chromite Ore Processing Residue (COPR): Past Practices, Environmental Impact and Potential Remediation Methods," *Curr. Environ. Eng.*, vol. 1, no. 2, pp. 82–90, 2014, doi: 10.2174/2212717801021411171015 51.

[74] M. Wazne, S. C. Jagupilla, D. H. Moon, C. Christodoulatos, and A. Koutsospyros, "Leaching Mechanisms of Cr(VI) from Chromite Ore Processing Residue," *J. Environ. Qual.*, vol. 37, no. 6, pp. 2125–2134, 2008, doi: 10.2134/jeq2007.0443.

[75] R. Trittschack, B. Grobéty, and M. Koch-Müller, "In situ high-temperature Raman and FTIR spectroscopy of the phase transformation of lizardite," *Am. Mineral.*, vol. 97, no. 11–12, pp. 1965–1976, 2012, doi: 10.2138/am.2012.4162.

[76] Y. El Mendili *et al.*, "Combined XRF, XRD, SEM-EDS, and Raman Analyses on Serpentinized Harzburgite (Nickel Laterite Mine, New Caledonia): Implications for Exploration and Geometallurgy," *ACS Earth Sp. Chem.*, vol. 3, no. 10, pp. 2237–2249, 2019, doi: 10.1021/acsearthspacechem.9b00014.

[77] I. Rashid *et al.*, *Magnesium Silicate*, 1st ed., vol. 36. Elsevier Inc., 2011.

[78] M. A. Rivero Crespo, D. Pereira Gómez, M. V. Villa García, J. M. Gallardo Amores, and V. Sánchez Escribano, "Characterization of serpentines from

different regions by transmission electron microscopy, X-ray diffraction, BET specific surface area and vibrational and electronic spectroscopy," *Fibers*, vol. 47, pp. 1–11, 2019.

[79] D. S. O'Hanley and M. D. Dyar, "The composition of lizardite 1T and the formation of magnetite in serpentinites," *Am. Mineral.*, vol. 78, no. 3–4, pp. 391–404, 1993.

[80] C. Rinaudo, D. Gastaldi, and E. Belluso, "Characterızatıon Of Chrysotıle, Antıgorıte And Lızardıte By Ft-Raman Spectroscopy," *Can. Mineral.*, vol. 41, no. 4, pp. 883–890, Aug. 2003, doi: 10.2113/gscanmin.41.4.883.

[81] S. B. HOLMQUIST, "Conversion of Quartz to Tridymite," *J. Am. Ceram. Soc.*, vol. 44, no. 2, pp. 82–86, 1961, doi: 10.1111/j.1151-2916.1961.tb15355.x.

[82] T. Komabayashi, S. Omori, and S. Maruyama, "Petrogenetic grid in the system MgO-SiO 2 -H 2 O up to 30 GPa, 1600°C: Applications to hydrous peridotite subducting into the Earth's deep interior," *J. Geophys. Res. Solid Earth*, vol. 109, no. B3, Mar. 2004, doi: 10.1029/2003JB002651.

[83] N. L. BOWEN, "THE SYSTEM MgO—SiO2—H2O," *Geol. Soc. Am. Bull.*, vol. 81, no. January, pp. 41–60, 1970.

[84] S. M. Peacock and K. Wang, "On the Stability of Talc in Subduction Zones: A Possible Control on the Maximum Depth of Decoupling Between the Subducting Plate and Mantle Wedge," *Geophys. Res. Lett.*, vol. 48, no. 17, Sep. 2021, doi: 10.1029/2021GL094889.

[85] L. Yu, L. Fang, P. Zhang, S. Zhao, B. Jiao, and D. Li, "The utilization of alkali-activated lead–zinc smelting slag for chromite ore processing residue solidification/stabilization," *Int. J. Environ. Res. Public Health*, vol. 18, no. 19, 2021, doi: 10.3390/ijerph18199960.

[86] N. K. Nga, N. T. Thuy Chau, and P. H. Viet, "Preparation and characterization of a chitosan/MgO composite for the effective removal of reactive blue 19 dye from aqueous solution," *J. Sci. Adv. Mater. Devices*, vol. 5, no. 1, pp. 65–72, 2020, doi: 10.1016/j.jsamd.2020.01.009.

[87] A. Ansari, A. Ali, M. Asif, and Shamsuzzaman, "Microwave-assisted MgO NP catalyzed one-pot multicomponent synthesis of polysubstituted steroidal

pyridines," *New J. Chem.*, vol. 42, no. 1, pp. 184–197, 2018, doi: 10.1039/c7nj03742b.

[88] D. Durgalakshmi, R. Ajay Rakkesh, S. Kamil, S. Karthikeyan, and S. Balakumar, "Rapid Dilapidation of Alcohol Using Magnesium Oxide and Magnesium Aspartate based Nanostructures: A Raman Spectroscopic and Molecular Simulation Approach," *J. Inorg. Organomet. Polym. Mater.*, vol. 29, no. 4, pp. 1390–1399, 2019, doi: 10.1007/s10904-019-01105-3.

[89] X. Huang, R. L. Zhuang, F. Muhammad, L. Yu, Y. C. Shiau, and D. Li, "Solidification/stabilization of chromite ore processing residue using alkali-activated composite cementitious materials," *Chemosphere*, vol. 168, p. 300, 2017, doi: 10.1016/j.chemosphere.2016.10.067.

[90] M. Xia *et al.*, "Detoxification and immobilization of chromite ore processing residue using the alkali-activated cementitious materials mixed with ascorbic acid," *J. Environ. Manage.*, vol. 265, no. April 2019, p. 110350, 2020, doi: 10.1016/j.jenvman.2020.110350.

[91] D. A. Long, *The Raman Effect*. Wiley, 2002.

[92] B. Smith, *Infrared Spectral Interpretation*. CRC Press, 2018.

[93] P. Griffiths and J. Haseth, "Fourier Transform Infrared Spectrometry, Second Edition," 2006, doi: 10.1002/9780470106310.ch9.

[94] S. Schwartz *et al.*, "Pressure-temperature estimates of the lizardite/antigorite transition in high pressure serpentinites," *Lithos*, vol. 178, pp. 197–210, 2013, doi: 10.1016/j.lithos.2012.11.023.

[95] D. A. McKeown, M. I. Bell, and R. Caracas, "Theoretical determination of the Raman spectra of single-crystal forsterite (Mg2MSiO4)," *Am. Mineral.*, vol. 95, no. 7, pp. 980–986, 2010, doi: 10.2138/am.2010.3423.

[96] J.-M. Delaye, "Investigation of alumino-silicate glasses by coupling experiments and simulations: Part I - Structures." doi: https://doi.org/10.1016/j.jnoncrysol.2021.120936.

[97] K. Ishioka, K. G. Nakamura, and M. Kitajima, "Reduction in Raman intensity of Si(1 1 1) due to defect formation during ion irradiation," *Solid State Commun.*, vol. 96, no. 6, pp. 387–390, Nov. 1995, doi: 10.1016/0038-1098(95)00419-X.

[98] M. Li, Y. Liu, Y. Lin, X. Guo, R. Hong, and H. Shen, “Study on amorphous silicon thin film by aluminum-induced crystallization,” *Phys. Procedia*, vol. 18, pp. 77–80, 2011, doi: 10.1016/j.phpro.2011.06.061.

[99] T. S. Perova, R. A. Moore, K. Lyutovich, M. Oehme, and E. Kasper, “Strain, composition and crystalline perfection in thin SiGe layers studied by Raman spectroscopy,” *Thin Solid Films*, vol. 517, no. 1, pp. 265–268, 2008, doi: 10.1016/j.tsf.2008.08.060.

[100] O. R. K. Montedo, F. J. Floriano, J. de Oliveira Filho, E. Angoletto, and A. M. Bernardin, “Sintering behavior of LZSA glass-ceramics,” *Mater. Res.*, vol. 12, no. 2, pp. 197–200, 2009, doi: 10.1590/S1516-14392009000200014.

[101] C. Venturelli, “Heating Microscopy and its Applications,” *Micros. Today*, vol. 19, no. 1, pp. 20–25, 2011, doi: 10.1017/s1551929510001185.

[102] R. M. German, “Sintering Trajectories: Description on How Density, Surface Area, and Grain Size Change,” *Jom*, vol. 68, no. 3, pp. 878–884, 2016, doi: 10.1007/s11837-015-1795-8.

[103] K. Edalati, I. Fujita, X. Sauvage, M. Arita, and Z. Horita, “Microstructure and phase transformations of silica glass and vanadium oxide by severe plastic deformation via high-pressure torsion straining,” *J. Alloys Compd.*, vol. 779, pp. 394–398, 2019, doi: 10.1016/j.jallcom.2018.11.086.

[104] M. R. Irshidat, M. H. Al-Saleh, and S. Sanad, “Effect of Nanoclay on the Expansive Potential of Cement Mortar due to Alkali-Silica Reaction,” *ACI Mater. J.*, vol. 112, no. 6, pp. 801–808, Dec. 2015, doi: 10.14359/51687856.

[105] M. C. Biesinger, B. P. Payne, A. P. Grosvenor, L. W. M. Lau, A. R. Gerson, and R. S. C. Smart, “Resolving surface chemical states in XPS analysis of first row transition metals, oxides and hydroxides: Cr, Mn, Fe, Co and Ni,” *Appl. Surf. Sci.*, vol. 257, no. 7, pp. 2717–2730, 2011, doi: 10.1016/j.apsusc.2010.10.051.

[106] L. Mao *et al.*, “The role of temperature on Cr(VI) formation and reduction during heating of chromium-containing sludge in the presence of CaO,” *Chemosphere*, vol. 138, pp. 197–204, 2015, doi: 10.1016/j.chemosphere.2015.05.097.

[107] Y. Lan, L. Zhang, X. Li, W. Liu, X. Su, and Z. Lin, “Efficient immobilization and utilization of chromite ore processing residue via hydrothermally constructing

spinel phase Fe2+(Cr3+X, Fe3+2-x)O4 and its magnetic separation," *Sci. Total Environ.*, vol. 813, p. 152637, 2022, doi: 10.1016/j.scitotenv.2021.152637.

[108] R. Zhao *et al.*, "Synergistic immobilization of chromium in tannery sludge by ZnO and TiO2 and the oxidation mechanism of Cr(III) under alkaline in high temperature," *J. Hazard. Mater.*, vol. 424, no. PA, p. 127290, 2022, doi: 10.1016/j.jhazmat.2021.127290.

[109] R. Choudhary, S. Koppala, and S. Swamiappan, "Bioactivity studies of calcium magnesium silicate prepared from eggshell waste by sol-gel combustion synthesis," *J. Asian Ceram. Soc.*, vol. 3, no. 2, pp. 173–177, 2015, doi: 10.1016/j.jascer.2015.01.002.

[110] K. Hrabovská, J. Podjuklová, K. Barčová, L. Dobrovodská, and K. Pelikánová, "Vitreous enamel coating on steel substrates," *Solid State Phenom.*, vol. 147–149, pp. 856–860, 2009, doi: 10.4028/www.scientific.net/SSP.147-149.856.

[111] W. Xia and J. Chang, "Preparation and the phase transformation behavior of amorphous mesoporous calcium silicate," *Microporous Mesoporous Mater.*, vol. 108, no. 1–3, pp. 345–351, 2008, doi: 10.1016/j.micromeso.2007.04.013.

[112] S. M. Salman, S. N. Salama, H. Darwish, and E. A. Mahdy, "The role of MgO on the structural properties of CaO-Na2O(MgO)-P2O5-CaF2-SiO 2 derived glass ceramics," *Ceram. Int.*, vol. 36, no. 1, pp. 55–61, 2010, doi: 10.1016/j.ceramint.2009.06.021.

[113] S. Zhang, S. Tie, and F. Zhang, "Cristobalite formation from the thermal treatment of amorphous silica fume recovered from the metallurgical silicon industry," *Micro Nano Lett.*, vol. 13, no. 10, pp. 1465–1468, 2018, doi: 10.1049/mnl.2018.5167.

[114] H. Norsker and J. Danisch, *Glazes — for the Self-Reliant Potter*. Wiesbaden: Friedr. Vieweg & Sohn Verlagsgesellschaft mbH, 1993.

[115] M. Hunkel, H. Surm, and M. Steinbacher, "Dilatometry," *Handb. Therm. Anal. Calorim.*, vol. 6, pp. 103–129, 2018, doi: 10.1016/B978-0-444-64062-8.00019-X.

[116] M. G. Rasteiro, T. Gassman, R. Santos, and E. Antunes, "Crystalline phase characterization of glass-ceramic glazes," *Ceram. Int.*, vol. 33, no. 3, pp. 345–354, 2007, doi: 10.1016/j.ceramint.2005.10.002.

[117] G. Gavriliu, “Thermal expansion and characteristic points of -Na2O-SiO2 glass with added oxides,” *J. Eur. Ceram. Soc.*, vol. 22, no. 8, pp. 1375–1379, 2002, doi: 10.1016/S0955-2219(01)00448-4.

[118] M. D. Ediger, C. A. Angell, and S. R. Nagel, “Supercooled liquids and glasses,” *J. Phys. Chem.*, vol. 100, no. 31, pp. 13200–13212, 1996, doi: 10.1021/jp953538d.

[119] A. Campopiano, A. Olori, A. Cannizzaro, A. Iannò, and P. P. Capone, “Quantification of Tremolite in Friable Material Coming from Calabrian Ophiolitic Deposits by Infrared Spectroscopy,” *J. Spectrosc.*, vol. 2015, 2015, doi: 10.1155/2015/974902.

[120] K. Chen *et al.*, “Improved Oxidation and Hot Corrosion Resistance of 1Cr11Ni2W2MoV Stainless Steel at 650 °C by a Novel Glass-Ceramic Coating,” *Crystals*, vol. 11, no. 10, p. 1213, Oct. 2021, doi: 10.3390/cryst11101213.

[121] I. Santoso *et al.*, “Impact of recently discovered sodium calcium silicate solutions on the phase diagrams of relevance for glass-ceramics in the Na2O-CaO-SiO2 system,” *J. Eur. Ceram. Soc.*, vol. 42, no. 5, pp. 2449–2463, 2022, doi: 10.1016/j.jeurceramsoc.2022.01.010.

[122] B. Heid, “Emaillierungen für Edelstähle,” Technischen Universität Clausthal, 2007.

[123] “ISO, ‘Vitreous and porcelain enamels — Determination of resistance to chemical corrosion — Part 2: Determination of resistance to chemical corrosion by boiling acids, boiling neutral liquids, alkaline liquids and/or their vapours,’ International Organizat.”

[124] “ISO 2178:2016 - Non-magnetic coatings on magnetic substrates — Measurement of coating thickness — Magnetic method, International Organization for Standardization, Geneva, 2016.”

[125] “ISO, Cold rolled low carbon steel flat products for vitreous enameling. Technical delivery conditions, International Organization for Standardization, Geneva, 2013.”

PUBLICATIONS FROM THE THESIS

Conference Papers

1. K. Karaman, Y. B. Yılmaz, T. Cengiz, B. Çiçek, '' An Example of the Reuse of Waste as Raw Material: Use of Chromite Mining Waste in the Inorganic Coating Industry'' XI. Ceramic Congress with International Participation, SERKON22, November 2022, Afyon